Department of Information Engineering

Master's degree in ICT for Internet and Multimedia

Optoelectrical Fibertrodes based on Microfabrication for Neural Stimulation and Recordings

Candidate

Pietro Metuh – pietro.metuh@studenti.unipd.it

Supervisor

Prof. Luca Palmieri – luca.palmieri@dei.unipd.it

External supervisors

Prof. Christos Markos – chmar@dtu.dk

Dr. Marcello Meneghetti – mamen@dtu.dk

Academic Year 2022 – 2023

July 13th, 2023

DEI
Department of Information Engineering
Università degli Studi di Padova
Via Gradenigo 6/b
35131
Padova, Italy

Abstract

In this document, the thesis report for the Master's degree in ICT for Internet and Multimedia at the University of Padova (Unipd) and the Master of Science in Photonics Engineering at the Technical University of Denmark (DTU) is reported. The project corresponds to 30 ECTS for both universities, and it is the last activity for achieving the degrees under the TIME (Top International Managers in Engineering) double-degree program. This thesis reports on designing, fabricating, and characterizing fibertrode devices for neural stimulation in the central nervous system. These waveguide-shaped interfaces aim to optically stimulate selected spinal cord regions with optogenetics by introducing scattering points along the waveguide. Simultaneously, the interfaces electrically record the neural response via exposed metal electrodes, whose signal can be read by connectorizing them to a setup for electrophysiology.

Chapter 1 contains an overview of the topic of the project, with a brief description of the research problem to be solved, the contribution of this project, the methods, and the previous work on this matter. Chapter 2 provides an overview of the theoretical knowledge acquired and applied during the project, mainly dealing with polymer waveguide fabrication, optrode design, optogenetics, and electrophysiology. Chapter 3 briefly introduces finite-element modeling and the information on the simulations evaluated in COMSOL Multiphysics and the Wave Optics package to analyze the scattering properties for different geometrical parameters. Chapter 4 includes the most significant contribution of the thesis and illustrates the tested fabrication processes for the optrode interface, concluding with a protocol for the fabrication of the final device. In Chapter 5, the characterization methods of the optrode are illustrated. The employed techniques include the probing of optical scattering and electrochemical impedance spectroscopy. The final analysis consisted of an acute *in vivo* study in collaboration with the University of Copenhagen for electrophysiological recordings along the spinal cord of a rat. Finally, Chapter 6 summarizes the project's key findings and hints at possible future work possibilities to improve the interface further.

Sommario

Nel seguente documento è riportata la tesi per la laurea magistrale in ICT for Internet and Multimedia presso l'Università degli Studi di Padova (Unipd) e in Photonics Engineering presso la Technical University of Denmark (DTU). Il progetto corrisponde a 30 CFU per entrambe le università, ed è l'ultima attività per conseguire le due lauree con il programma di doppia laurea TIME (Top International Managers in Engineering). La seguente tesi riguarda la progettazione, fabbricazione e caratterizzazione di dispositivi *fibertrode* per stimulazione neurale nel sistema central nervoso. Queste interfacce a forma di guida d'onda mirano a stimulare specifiche regioni del midollo spinale tramite l'optogenetica, introducendo punti di scattering lungo la guida d'onda. Inoltre, le interfacce misurano i segnali elettrici neurali tramite elettrodi in metallo, la cui risposta può essere registrata tramite connettorizzazione ad un'interfaccia per l'elettrofisiologia.

Il Capitolo 1 contiene una panoramica dell'argomento del progetto, con una breve descrizione del problema di ricerca da risolvere, la contribuzione di questo progetto, i metodi sperimentali e clinici, e i precedenti studi al riguardo. Il Capitolo 2 offre una panoramica delle conoscenze teoriche acquisite e applicate durante il progetto, in particolare riguardo alla fabbricazione di guide d'onda in polimero, la progettazione di optrodi, l'optogenetica, e l'elettrofisiologia. Il Capitolo 3 introduce brevemente il metodo degli elementi finiti e le informazioni sulle simulazioni prodotte in COMSOL Multiphysics e il pacchetto Wave Optics per analizzare le proprietà di scattering per diversi parametri geometrici. Il Capitolo 4 contiene la contribuzione più significativa della tesi e illustra i processi di fabbricazione testati per l'interfaccia neurale, terminando con un protocollo per la fabbricazione del dispositivo finale. Nel Capitolo 5 sono illustrati i metodi di caratterizzazione per l'optrode. Le tecniche utilizzate includono il tracciamento dello scattering ottico e la spettroscopia d'impedenza elettrochimica. L'ultima analisi consiste in uno studio *in vivo* acuto in collaborazione con l'Università di Copenaghen per registrazioni elettrofisiologiche lungo il midollo spinale di un ratto. Infine, il Capitolo 6 riepiloga le principali scoperte del progetto e conclude con dei suggerimenti per possibili studi futuri volti a migliorare ulteriormente l'interfaccia.

Acknowledgements

The realization of this project was only possible thanks to the contribution of many people. I want to thank Luca Palmieri, Christos Markos, and Marcello Meneghetti, my supervisors, for their time and guidance during the project, as well as the words of encouragement in the most challenging times and the constructive feedback needed when carrying on a research project. In particular, I wish to thank Christos Markos for the ideas he provided during the brainstorming phases for the fabrication of the interface and his care in making the collaboration between us and the Neuronal Signalling Group from the University of Copenhagen possible. I thank Marcello Meneghetti, of whom I have required assistance in so many ways throughout the project, for his work in training me to use the optical setups and the thermal drawing tower, designing the adapter for the connectorization of the interface, implanting the device during an acute experiment, and for the general consultations in the modeling and data post-processing steps. I would also like to thank Maria Elena Valcher for enabling the recognition of this work at my home university and for being readily available whenever I needed their help.

A special thanks to Martin Nielsen, John Lauridsen, and Jan Normann Mortensen from the workshop at the National Space Institute (DTU Space), whom I have asked for help several times in preparing the polymer preforms. I would also like to acknowledge Jesper Hanberg and Rune Christiansen from DTU Nanolab for consulting and helping me with the fabrication steps of the project and for training me on the laser micromachining tool, which was fundamental for the realization of the device.

I am incredibly grateful to Amaia de Diego Ajenjo and Rune Berg from the Neuronal Signalling Group at the Department of Neuroscience of the University of Copenhagen, who performed the surgery for the acute experiment in the final testing phase of the project. Moreover, I would also like to thank the other Neural Devices and Gas Photonics group members who have helped me in the last five months, Parinaz Abdollahian and Kunyang Sui.

I wish to conclude by expressing my gratitude to my girlfriend Konstantina, my mum Maria Antonella, my dad Jude and my aunt Alice for the cherished support they have provided throughout my journey at the Technical University of Denmark, especially during this final project, when their encouragement has been more important than ever.

The project had many ups and downs, but we always found a workaround whenever I felt we had reached a dead-end. This experience has given me a great foundation of how academic research works. I am excited to finally share my learnings and milestones, which would not have happened without all these people.

Abbreviations

AOM acousto-optic modulator

CAD computer-aided design

ChR1 channelrhodopsin-1

ChR2 channelrhodopsin-2

COC cyclic olefin copolymers

CVD chemical vapor deposition

DCC DTU Computing Center

DI de-ionized

DNA deoxyribonucleic acid

EEG electroencephalogram

EIS electrochemical impedance spectroscopy

ewbe electromagnetic waves, beam envelopes

ewfd electromagnetic waves, frequency domain

FEM finite element method

FTTH fiber-to-the-home

HPC high performance computing

HP high-pass

LED light-emitting diode

LFP local field potential

LMT laser micromachining tool

NIR near infrared

NUV near ultraviolet

OSA optical spectrum analyzer

PBS phosphate-buffered saline

PCB printed circuit board

PC polycarbonate

PEC perfect electric conductor

PMC perfect magnetic conductor

PML perfectly matched layer

PMMA poly(methyl methacrylate)

POF polymer optical fiber

POW polymer optical waveguides

PSD power spectral density

RAM random access memory

RIE reactive-ion etching

SEM scanning electron microscope

SHG second harmonic generation

SNR signal-to-noise ratio

SPF scattering phase function

SPP surface plasmon polariton

TEM transverse-electromagnetic

TE transverse-electric

TFP thin-film polarizer

THG third harmonic generation

TIR total internal reflection

TM transverse-magnetic

List of Figures

List of Tables

Contents

Chapter 1

Introduction

1.1 Background

This project consists of the design, fabrication, and characterization of a fibertrode (a portmanteau of *fiber* op*trode*) for the stimulation and the recording of neural activity along the spinal cord, the part of the central nervous system that primarily transmits nerve signals from the motor cortex to the body [1]. Such devices are being investigated for optogenetics, a technique that uses optical signals and photosensitive proteins to control the activity of neurons, and electrophysiology, which is used to monitor such activity by recording electrical signals.

Neuromodulation by electrical stimulation has been used to treat chronic pain, movement disorders, and psychiatric illnesses. However, electrical stimulation lacks specificity in targeting the neurons, which impacts its effectiveness and safety [2]. In the last 20 years, optogenetics has gained popularity because of its ability to control neurons with light and photosensitive proteins instead of electrical currents. In particular, optogenetics was first investigated for the need to control one type of cell while leaving the others unaltered and thus target specific events in biological systems [3]. This technique has become important not only to analyze the causal relationship between cellular events and other parts of a complex biological organism but also to treat or investigate neurodegenerative diseases such as Parkinson's [4] and Alzheimer's [5]. Behavioral experiments have gained a lot of attention in the last twenty years, primarily for their applications in memory, learning, and neural stimulation, and optogenetics is one of the main techniques developed to stimulate the central nervous system [6]. This technique has opened research toward the understanding and treatment of neurological diseases [7]. Other applications of optogenetics also involve other neural systems for the treatment of, for example, bladder dysfunction to improve urination [8].

Some optogenetic systems implement additional functions, such as electrochemical sensing [9] and drug delivery [10], for improved analysis of the neural circuits. This project focuses on combining the optical interface with electrical recording. The combination of optogenetics with electrophysiology enables the recording of the stimuli with a single interface by collecting the electrical signals conveyed by the stimulated neurons. Monitoring cellular activity when stimulating cells allows testing whether the stimulation is working as expected. While the activity in the central nervous system can be monitored in various ways, such as optical functional imaging or magnetic resonance imaging [11], electrophysiology can be readily integrated on the same probe used for optogenetics and is

characterized by high spatial and temporal resolutions.

1.2 Prior work

Optogenetics first emerged in the 1970s, when biologists discovered that some proteins, the so-called opsins, behaved as ion gates when exposed to visible light at specific wavelengths [3]. There are different classes of opsins, and although bacteriorhodopsins were described as light-sensitive ion channels back in 1971, greater advances came with the description of channelrhodopsins in 2002 and with the emergence of optogenetics by demonstrating single-component control tools in 2005, which revealed how to target one type of cells and leave the others unaltered. In 2007, the first fiber-optic tool enabled optogenetic control deep in the brain of freely moving animals [12, 13]. In the same year, hybrids of optical fibers and electrodes (optrodes) first appeared [14].

From an engineering point of view, one of the main problems that must be solved to ease the implementation of optogenetics is a means to illuminate a limited tissue region. Recently, two main approaches have been investigated. One deals with implanted micro-LEDs, whose main advantage is restricting the illumination volume and reducing the implantable system dimensions [15]. Micro-LEDs have been primarily tested in brain implants [16, 17], although distributed optogenetics along the spinal cord has been demonstrated [18]. Micro-LEDs, however, are more complex to assemble than monolithically integrated solutions and are still relatively bulky compared to electrical probes. Moreover, since LEDs are in close contact with the tissue, heat generation can cause undesired increases in temperature in the tissue [2].

The second approach is based on optical stimulation with optical fibers or probes. Most techniques rely on silica or inert polymer optical fibers. However, the former is not biocompatible and is relatively brittle. Polymer optical fibers, conversely, are more flexible and biocompatible but are characterized by higher attenuation and need to be surgically removed after the implant [19]. The main advantage of optical fibers and optical waveguides is the lack of tissue heating during irradiation, easier integration with electrodes to add electrophysiology capability, and a lower expected cost of the device [20]. Novel fibers have been used to demonstrate the use of biodegradable material to eliminate the risk associated with removing the fibers [19, 21]. Nevertheless, the tethering approach alters behavioral tasks and natural movement and might cause tissue damage, especially when brain stimulation is combined with pharmacological functions [7]. While probes have the advantage of compatibility with monolithic fabrication, significantly reducing the bulk of an interface compared to optical fibers, an optical fiber or a ferrule is usually still required to couple light into the waveguide [22].

Optogenetic implants are sometimes paired with electrodes to add electrophysiology capability, namely the electrical recording of the neuronal activity [11]. Devices combining optical stimulation and electrical recording are referred to as optrodes. One of the main problems with optrodes is the photoelectric noise caused by the recording sites and the illumination regions being too close to each other [20]. The electromagnetic field might generate a surface current density on the metal, creating artificial electrical signals. Different electrodes and post-processing techniques have been shown to mitigate the artifacts introduced by this noise effectively [11].

Combined optogenetics/electrophysiology techniques have been demonstrated as a powerful tool for distinguishing the causal roles of neural regions. Some works have shown promising multimodal probes for multipoint brain stimulation and recording [16, 17, 23–25]. However, to the author's knowledge, multimodal optrodes have not been demonstrated in the spinal cord, which is rich with excitable cells for therapeutic modulation, including motor neurons, sensory neurons, and interneurons [26]. Modulating activity in these targets has been traditionally accomplished by electrical stimulation, which has been used to treat chronic conditions such as spinal cord injury or epilepsy. Electrical stimulation, however, fails in many patients for reasons not yet well understood, induces muscle fatigue when stimulating paralyzed muscles, and cannot prevent muscle contractions in patients with spasticity [26]. Conversely, optogenetics can be implemented with cell type specificity without involuntarily contracting the patient's muscles and can, in principle, stimulate tissue from a longer distance.

The main challenge for implants in the spinal cord lies in the penetration of the probe. Optical fibertrodes are often extended deep into brain tissue, with minimal reported changes in animal behavior due to the tissue damage caused by the implant. However, such penetration appears unfeasible for the spinal cord, as the penetration will likely require the severing of white matter tracts, where local damage can have global consequences for the animal [26]. Therefore, it is even more critical to replace the stiffness of silica optical fibers, metals, and other stiff probe materials is particularly incompatible with spinal cord implants, with softer polymers, whose Young's modulus is closer to the typical values in the spinal cord (40-60 kPa) [27]. Consequently, the implant must be flexible and have a structure that can accommodate the shape of the spinal cord, even with the displacement that might be introduced by motion.

1.3 Research problem, goals, and methods statement

In this project, a novel flexible optrode design for multi-site stimulation and recording was developed for applications in the spinal cord. The main problem that this interface aims to solve is the simultaneous multi-site optical stimulation and electrical recording of different neuronal sites along the spinal cord. Although multi-site optogenetic stimulation or multi-site electrophysiology have already been separately demonstrated by many [28], this work aims to implement both multi-site optical stimulation and electrical physiology on a flexible, tissue-compatible substrate, that can accommodate the spinal cord thanks to its rectangular cross-section. The optrode design features micro-holes on the surface of the flexible probe, whose purpose is to control the light illumination volume and expose the electrodes buried in the waveguide.

The ultimate purpose of this thesis project was thus to demonstrate this scalable fibertrode for multi-site optical stimulation and electrophysiology with a relatively simple geometry and fabrication process. The project featured a combination of modeling and analysis, microfabrication, characterization, and experimental methods in neuroscience. The most significant contribution and focus, however, lies in the microfabrication of the neural interface to demonstrate the feasibility of a device that is both versatile (i.e., can perform optogenetics and physiology) and compatible with spinal cord tissue (i.e., made with biocompatible materials and with a flexible substrate). To the

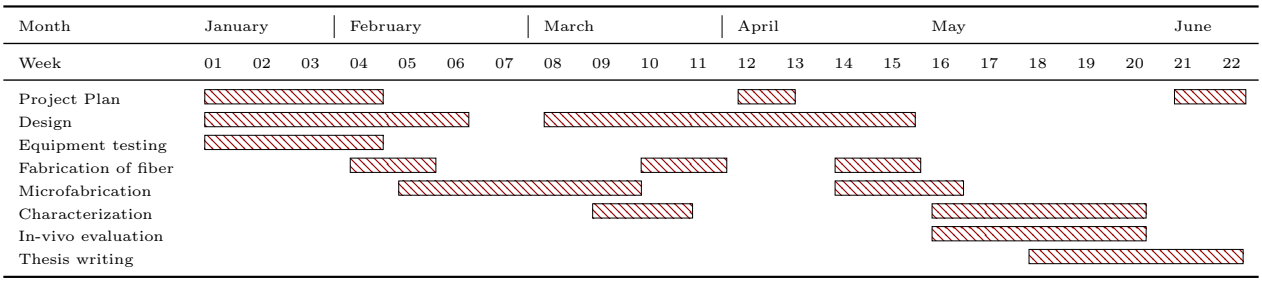

Table 1.1: Revisited Gantt chart with the project timeline, including the main expected milestones and activities.

author's knowledge, a flexible polymer interface for implants along the spinal cord for multi-site neural stimulation and recording in rodents has not been realized yet.

After some initial simulations of the polymer waveguide via COMSOL Multiphysics, a microstructured polymer optical waveguide was fabricated by thermal drawing, holes for scattering enhancement and electrode exposure were micromachined, and microwire electrodes were integrated into it. After connectorization, the device was then characterized electrically (with electrochemical impedance spectroscopy) and optically (with optical spectroscopy and time-resolved scattering measurements), and its performance was evaluated under an *in vivo* study for electrophysiological recordings. As shown in the Gantt chart of Table 1.1, the project advancement was not linear, as the newly encountered problems often required a redesign or different fabrication approach for a solution. The simulation activities were often carried out simultaneously with the fabrication tasks, as many steps require machines, materials, or other tools to be ready before advancing. Many designs and materials were tested, but only one gave consistent results that could be replicated and thoroughly tested. The optoelectrical characterization was also terminated when post-processing and analyzing the data from the *in vivo* trial. As one can see by comparing Table 1.1 with the initial project plan, the fabrication techniques and the overall timeline have changed considerably as new workarounds and methods were discovered. The project plan itself was updated twice, once halfway through the project and finally at the end of it, during the writing of this document. Detailed comments on the initially proposed milestones are given in the final chapter.

Chapter 2

Theoretical background

The following chapter describes the main theoretical concepts behind the developed optoelectronic interface, its fabrication, and the clinical techniques it aims to implement. Section 2.1 begins with a brief recap of basic optics concepts to describe the number of modes in a rectangular polymer waveguide, used in the future sections and in the next chapter when dealing with the choice of the model to use in simulations. Section 2.2 continues with an overview of the fabrication techniques for polymer waveguides, with a particular focus on preform production and thermal drawing, the two methods used in the experimental part of the project. Section 2.3 covers the basics of light transmission in biological tissue and, more specifically, in the main components of the central nervous system, white and gray matter. The chapter continues with an overview of the two clinical methods that this project's interface attempts to implement. The device targets optogenetics (Section 2.4), namely the stimulation or characterization of neural stimuli via light impulses, and electrophysiology (Section 2.5), that is, the recording of the neural response via electrodes. Nevertheless, the main objective of the project and the author's background are focused on the engineering part; hence, the medical part is not further developed. Finally, the design requirements for the optrode interface are illustrated in Section 2.6, where the main challenges for optical stimulation and electrical recording are presented.

2.1 Optical waveguides

Optical waveguides are used to confine and guide light in the optical spectrum, which usually refers to the visible spectrum (between about 380 nm and 750 nm), but might also include near ultraviolet (NUV) and near infrared (NIR) in some cases. The simplest optical waveguide is made of a medium with a refractive index n_1 embedded in a medium with a lower index $n_2 < n_1$. In ray optics, the working principle of optical waveguides can be proven via Snell's law, namely

$$n_1 \sin\theta_1 = n_2 \sin\theta_2, \tag{2.1}$$

where θ_1, θ_2 are the incident and refractive angles, respectively. When light rays inside the first medium propagate with an incidence angle higher than the critical angle θ_c, namely the angle such that $\sin\theta_2 = 1$, or

$$\theta_c = \arcsin\left(\frac{n_2}{n_1}\right), \tag{2.2}$$

the so-called total internal reflection (TIR) condition is satisfied, and light will reflect completely. Over a straight waveguide, this corresponds to propagation.

While the ray-optics model for light propagation is very useful for describing light-matter interaction with macroscopic objects, it also has several shortcomings, which increase as the size of the features becomes comparable to the size of the wavelength. A much more accurate yet complex model is given by electromagnetic optics, which is described by Maxwell's equations. While Maxwell's equations generally feature complex-valued tensors (the electric permittivity ϵ and the magnetic permeability μ), as an optical medium is generally dispersive, absorptive, anisotropic, and nonlinear, the equations can often be dramatically simplified for relatively weak fields in transparent media (i.e., media with low light dispersion and absorption within the desired portion of the spectrum), such that the parameters of the equation become scalar and real-valued. In this case, each vector component u of the three-dimensional electric and magnetic fields $\mathbf{e}$ and $\mathbf{h}$ satisfies the wave equation

$$\nabla^2 u - \frac{1}{c^2}\frac{\partial^2 u}{\partial t^2} = 0, \tag{2.3}$$

where $c = \frac{1}{\sqrt{\epsilon\mu}} = c_0/n$ is the speed of light in the medium.

Electromagnetic optics can describe the interactions with small scatterers, absorption in media, polarization effects, and many more phenomena that ray optics does not predict [29]. Mathematically speaking, geometrical optics is the limit of wave optics as the wavelength λ approaches 0. In general, the TIR of ray optics at a given angle corresponds to the propagation of a mode, namely a solution to Maxwell's equations that propagates indefinitely inside a waveguide, assuming that absorption can be neglected. Contrary to ray optics, the number of modes in a waveguide is discrete, but it becomes virtually continuous as the size of the waveguide increases. Modes are often described as a superposition of transverse modes, which can be divided into transverse-electric (TE) and transverse-magnetic (TM) modes, depending on whether the electric or magnetic field component is orthogonal to the direction of propagation. In transverse-electromagnetic (TEM) modes, both the electric and the magnetic field components along the direction of propagation are zero, which is not compatible with the boundary conditions in a geometry of a waveguide with finite width and length.

Let us now assume that the electromagnetic wave is monochromatic, namely that the fields are time-dependent as

$$u(\mathbf{r}, t) = \mathrm{Re}\left[u(\mathbf{r})e^{i\omega t}\right], \tag{2.4}$$

where ω is the angular frequency of the monochromatic wave. In this case, the wave equation can be written as a Helmholtz equation as

$$\nabla^2 u + k^2 u = 0, \tag{2.5}$$

which is now an eigenproblem with eigenvalue $\omega^2 n^2/c_0^2 = k^2$. This equation will be shown in Section 3.1, where the equations solved in the numerical modeling are presented. When a waveguide is small compared to the wavelength (depending on the geometry of the waveguide, but in general when the cross-section dimensions are comparable to λ), only a few modes can propagate. For instance, in optical fibers and rectangular waveguides, there are two fundamental modes that can be excited at any wavelength. [29]. As the size of the waveguide cross-section increases, more propagating solutions are generated for the wave equation in (2.3). Each of them can be identified by an effective refractive

index $n_{\text{eff}} \equiv n\beta/k_0$, where β is the propagation constant (the component of the wavevector along the propagation direction) and $k_0 = \omega/c$ is the wavenumber in free space.

In general, there is no simple solution to Maxwell's equations and the boundary conditions for a waveguide. However, analytical solutions can be found for waveguides with simple geometries. The simplest is the slab waveguide, often referred to as a one-dimensional waveguide or planar waveguide. It consists of an infinitely-extending slab of dielectric material with index n_1, surrounded by a medium of lower index $n_2 < n_1$.

In real-world conditions, confinement is often sought in two directions (as the wave propagates along the third). The most popular geometry for a 2D optical waveguide is the optical fiber, whose cross section in the simplest design features a circular core of index n_1 and a larger, circular cladding of slightly lower refractive index $n_2 < n_1$. Optical fibers are fabricated with low-loss materials (dependent on the application), and their design enabled unprecedented improvements in the transmission of optical signals, which was exploited first in telecommunications, and later in fields such as sensing and biomedicine.

As later sections explain, this project considers another optical waveguide, the so-called rectangular waveguide. As the name suggests, the cross-section of such a waveguide is rectangular, with a being the broad side and b being the narrower. The transversal component of the wavevector k_t must satisfy the critical-angle condition, that is [29]

$$k_t^2 \equiv k_x^2 + k_y^2 \leq n_1^2 k_0^2 \sin^2 \theta_c. \tag{2.6}$$

Within this region, the wavevector components must also satisfy a self-consistency condition so that the phase shift by an integer multiple of 2π for every transverse roundtrip. Two further conditions are thus given:

$$2k_x a = 2\pi m_x + 2\phi_r \tag{2.7}$$

$$2k_y b = 2\pi m_y + 2\phi_r, \tag{2.8}$$

where ϕ_r is the phase shift introduced by the reflection, which depends on the angle of incidence, and m_x, m_y are integers representing the mode number. It can be proved that these solutions can be represented as points within the ellipse given by (2.6) [29], as represented in Figure 2.1a. To obtain the number of modes, the intersection of the solutions of (2.7) and the ellipse area must be obtained.

When the waveguide is large, the number of modes (accounting for both TE and TM modes) can be approximated as [30]

$$M \approx \frac{\pi}{4}\frac{b}{a}\left(\frac{2a}{\lambda}\right)^2 \text{NA}^2, \tag{2.9}$$

where λ is the wavelength in vacuum and $\text{NA} \equiv \sqrt{n_1^2 - n_2^2}$ is the numerical aperture. An example showing the scaling of the number of modes for a rectangular waveguide with equal sides is shown in Figure 2.1b.

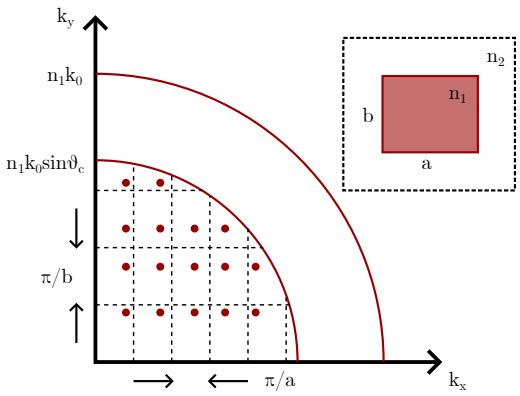

(a) Estimating the number of modes of a rectangular waveguide of sides a and b and refractive index n_1 in an environment of index n_2.

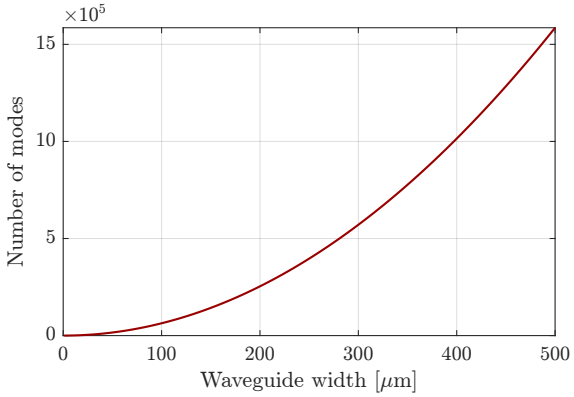

(b) Approximate number of modes in a rectangular waveguide made of a polymer ($n_1 = 1.58$) in water ($n_2 = 1.33$) against the side length $a = b$. The wavelength is $\lambda = 650\,\text{nm}$.

Figure 2.1: Number of modes in rectangular waveguides.

2.2 Polymer waveguide fabrication

While silica optical fibers virtually constitute the entire portion of waveguides for long-distance optical communications, mainly thanks to their low attenuation and dispersion in the third optical window (i.e., around 1550 nm), polymer optical waveguides (POW)s, and polymer optical fiber (POF)s find many applications in short-distance communications (e.g., the final link in fiber-to-the-home (FTTH)), thanks to the less stringent channel capacity requirements and the inexpensive production [31]. As a matter of fact, silica-based preforms are usually fabricated through a tedious chemical vapor deposition process, and the fibers are then thermally drawn at very high temperatures (1000 °C). Compared to silica, POWs have a glass transition temperature T_g (the temperature at which an amorphous material gradually transitions from a brittle state into a more viscous state) of 100-200 °C (in silica, $T_g = 1120\,°\text{C}$) [32]. However, it is worth stressing that the viscosity in silica is considerably less sensitive to temperature than typical polymers. While viscosity between 1000 and 2400 °C drops at a rate of about 0.93 orders of magnitude per 100 °C in silica, it drops at a much faster rate of 4.2 orders of magnitude per 100 °C in poly(methyl methacrylate) (PMMA) above the T_g [33, 34].

In addition to the production costs, polymer waveguides can have other intrinsic advantages over silica in other applications. For example, the sensing properties of distributed polymer waveguides are usually superior to silica, thanks to the higher temperature and strain coefficients, which translates into higher temperature and strain sensitivity. Moreover, the strain limit for polymers is generally greater than 3%, while the limit for silica is less than 1%. In biosensors, polymer waveguides also have the advantage of being flexible and nontoxic, which increases biocompatibility with the soft tissue in animals and humans.

In the following subsections, the most common approaches to POW thermal drawing, based on producing one preform (or more, in the case of microstructured fibers) and the subsequent thermal drawing of the waveguide, are presented. It is worth noting, however, that other preformless techniques have also been developed. These techniques can be divided into two categories:

- On-substrate monolithic microfabrication employs semiconductor-compatible fabrication methods, such as UV photolithography, reactive-ion etching (RIE) etching, photobleaching, ashing, injection molding, inkjet printing, and more [31, 35].

- Continuous extrusion, coextrusion, or melt spinning can also be used to fabricate waveguides and fibers with different profiles with continuous techniques, namely by running every step simultaneously [32, 36].

2.2.1 Preform production

The preform is an intermediate product with the same topology as the preform but with a much larger diameter and a contained length. In a subsequent drawing step, the preform becomes a thinner, longer waveguide [37].

Several techniques can be adopted to fabricate preforms for POWs. When producing microstructured POFs, for example, a common fabrication scheme relies on a two-step process, where the preform is first fabricated with the desired hole arrangement and stretched into a cane, reducing its diameter by a factor 10 or similar [38]. The canes are then assembled and used to form a secondary preform, from which the fiber is drawn. The main distinction between manufacturing techniques lies in the desired properties of the refractive index profile of the waveguide. Graded-index POFs, for instance, feature a progressive radial change in concentration of the material composition and are obtained with methods such as interfacial-gel polymerization, chemical vapor deposition, centrifugation, diffusion, and photochemical polymerization [37].

On the other hand, structured preforms can be made of a single material or multiple materials. Several techniques, briefly described below, have been used to fabricate structured preforms:

- Drilling. Mechanical or ultrasonic drilling has been used to produce tubes for step-index fibers or holes in POWs [32, 39]. Further machining and/or polishing may be required depending on the application.

- Stacking. Stacking consists of assembling rods, tubes, or plates from single or multiple materials into a preform. It may be applied recursively to obtain the required microstructure dimensions and features, but it raises challenges for reproducibility [32].

- Casting. Polymer casting is typically employed to produce preforms for waveguides, or rods and tubes for step-index preforms, by melting the material in a closed, evacuated container of the desired shape [32, 40].

- Extrusion. Extrusion can produce very complex microstructures, and it involves only a single processing step, where heated soft glasses are compressed and pushed through a die with the desired cross-section.

- Thin-film rolling. This process involves rolling a thin polymer film around a rod and thermally consolidating it under a vacuum above T_g to fuse the materials [32].

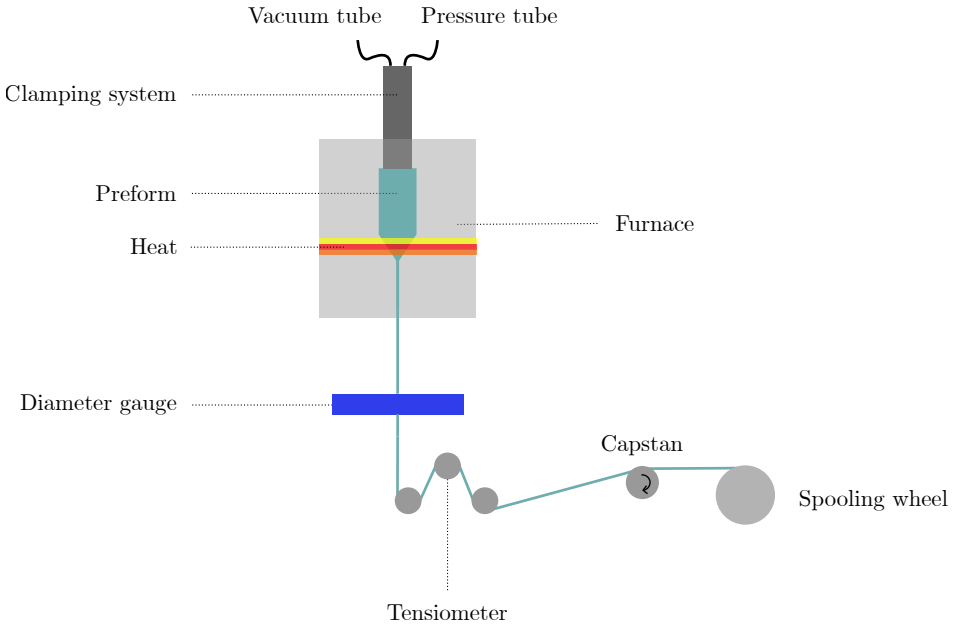

Figure 2.2: Schematic representation of a thermal drawing tower.

- Solvent deposition. This technique consists of slowly evaporating a solvent inside a rotating polymer tube (similarly to modified chemical vapor deposition (CVD) techniques for glass optical fiber production) for a controlled multilayer deposition process [41].

2.2.2 Thermal drawing

Once the preform is completed, it can be drawn to cane and/or fiber at a temperature sufficiently higher than the glass transition temperature T_g. Thermal drawing of POWs is carried on in drawing towers, similarly to silica fibers. Compared to silica, however, a drawing tower for polymers is considerably smaller and simpler, thereby improving the production cost and fabrication time. The main reason for this difference is in the drawing temperature. Recall that the glass transition temperature is about ten times higher in silica than the common polymers used in preforms. This requires a much higher tower and active cooling to ensure the temperature gradient is at the desired rate.

Figure 2.2 shows a schematic illustration of a drawing tower. Each component is briefly described below:

- The clamping system holds the preform, often using screw threads in the preform, and it controls its vertical position via a feed unit, usually interfaced via software, to adjust the feeder speed v_f. The clamping system can also be connected to a pressure or vacuum tube, whose purpose is explained below.

- The furnace contains the preform and features a hole at the top for the clamping rod and one at the bottom for the dropping polymer waveguide. A simple furnace has a single plane at maximum temperature, but more advanced designs might require multiple heaters and temperature sensors to better control the drawing process.

- The diameter monitor consists of a laser measuring the diameter of the dropping waveguide. Consequently, it is usually optimized to read waveguides with circular cross-sections, although some monitors can probe the diameter along different axes and provide a better estimate even for different geometries.

- The tensiometer gauges the tension on the waveguide, which is mainly governed by the temperature in the furnace, the feeder speed, and the capstan speed. Tension values for waveguides usually range between 0 and 100 g, depending on the diameter, while for canes, whose typical diameter is 6 mm, they can be as high as 2 kg [38].

- The capstan pulls the waveguide, maintaining a constant tension and draw rate.

- The tower usually ends with a spooling wheel, used to take up the waveguide and collect it in an orderly manner.

Silica optical fiber drawing towers include additional components, such as a cooling section, a polymer coater, a UV lamp or a second furnace for curing the polymer, and a second diameter gauge.

There are up to five main parameters to account for when drawing a waveguide:

- Temperature defines the viscosity of the material and, thus, how easily it flows and can be pulled. Higher setpoint temperatures reduce the risk of breaking the waveguide but are also more likely to distort the features of a microstructured waveguide.

- Gas pressure (optional) is applied when drawing microstructured waveguides and optical fibers to avoid the partial or total collapse of the holes previously produced in the preform.

- Vacuum (optional), on the other hand, is used when the preform is made by more than one phase. It collapses any undesired interface, avoiding air gaps trapped inside the final waveguide.

- The feeder speed v_f and the capstan speed v_p define the reduction factor of the waveguide, namely the ratio between a cross-sectional feature of the preform and the same feature on the waveguide. The length of these features changes with the known proportion from the mass conservation law [42]

$$\frac{v_f}{d_f^2} = \frac{v_p}{d_p^2}, \tag{2.10}$$

  where d_p is one of the section sides of the preform, and d_f is the corresponding side of the fiber.

2.2.3 Materials

The most commonly used polymer for POWs is PMMA (sometimes better known as acrylic, or as the trademark name Plexiglas), a low-cost, widely available polymer that is considered transparent between 350 and 850 nm [38, 43]. PMMA-POWs have a typical absorption coefficient of 0.15 dB/m minimum at 650 nm. Polycarbonate (PC) has similar optical properties to PMMA, except for slightly higher absorption in the visible, less water absorption, and a higher glass transition temperature. Moreover, thanks to their higher refractive index, PC and PMMA are also often used, respectively, in the core and the cladding of POFs. Other polymers, such as the cyclic olefin copolymers (COC)

Property	PMMA	PC	Topas	Cytop
n (589 nm, 25 °C)	1.49	1.58	1.53	1.34
Transmission [%]	92	90	91	95
T_g [°C]	115	145	134	108
Moisture absorption [%]	0.3	0.12	0.01	<0.01
Tensile strength [MPa]	75	63	63	41-49
Att. theor. limit [dB/km]	106 (650 nm)	–	0.3 (1300 nm)	–
Relative cost	Low	Low-mid	Mid-high	High

Table 2.1: Main properties of the polymers used in optical waveguides. Data from [37, 44].

Topas or Zeonex, are typically more expensive but have desired properties in some applications, such as sensing, where for example, the high water absorption of PMMA or PC might disrupt the accuracy of the device. In the infrared range, the absorption of POWs is dominated by molecular vibration losses. For applications in the NIR range, perfluorinated polymers (such as Cytop) are often used to decrease the absorption from fundamental vibrations and overtones from C-H bonds arising above 700 nm [37]. By replacing hydrogen atoms with a heavier element like fluorine, the vibration peaks are redshifted, thereby decreasing the absorptance of the polymer. Perfluorinated polymer fibers have a considerably lower theoretical attenuation limit of 0.3 dB/km, comparable to the attenuation of silica glass. A summary of some of the main optical, thermal, and mechanical properties of polymers is given in Table 2.1.

2.3 Light delivery in tissue

Light attenuation in tissue can be estimated by the Beer-Lambert law [11]

$$I(z) = I_0 e^{-\mu z}, \tag{2.11}$$

where I_0 is the initial light intensity and μ is the attenuation coefficient, which is a sum of the absorption coefficient μ_a and scattering coefficient μ_s in biological tissue [45]. A third parameter $p(\hat{\mathbf{s}}, \hat{\mathbf{s}}')$, the so-called scattering phase function (SPF), describes the fraction of light incident on a scatterer from a direction $\hat{\mathbf{s}}$ that gets scattered along another direction $\hat{\mathbf{s}}'$. To account for this anisotropy, one often defines an anisotropic factor, also known as the average cosine of scatter, which measures the portion of scattered light retained in the forward direction upon a scattering event and varies from -1 (light is completely backscattered) to 1 (light is completely forward scattered) [45]. Accounting for both absorption and scattering being highly dependent on the wavelength of the electromagnetic radiation and for the anisotropy of scattering in tissue (i.e., the fact that light will scatter with preferential angles), a full expression of the extinction coefficient can be given as

$$\mu_t(\lambda) = \mu_a(\lambda) + (1 - g)\mu_s(\lambda). \tag{2.12}$$

When delivering light in the central nervous system, two types of tissues are especially relevant: white and gray matter. The former contains few cell bodies and mainly comprises fiber nerves, while

Parameter	Tissue	Value
g	White matter	0.80
g	Gray matter	0.88
μ_s	White matter	$420\,\mathrm{cm}^{-1}$
μ_s	Gray matter	$110\,\mathrm{cm}^{-1}$
μ_a	White matter	$1 - 2\,\mathrm{cm}^{-1}$
μ_a	Gray matter	$0.17 - 20\,\mathrm{cm}^{-1}$

Table 2.2: Extinction values for gray and white matter. The values correspond to a wavelength of 500 nm. Adapter from [45].

the latter contains more cells and fewer nerves. A summary of the extinction parameters for these two tissues is given in Table 2.2. The reported values of the anisotropic factor (0.8 and 0.88) indicate a relatively low tendency of brain tissue to scatter light at optical frequencies.

The coupling of light from the source or the waveguide to the tissue depends on the optrode design and the desired profile. Some probes exploit the transmitted light at the end of a fiber to illuminate the biological tissue. Another method uses tapered optical fibers, illuminating large tissue volumes by emitting radiation over a long segment [46]. This design exploits the radial dependence on the number of propagating modes inside a fiber. Similarly to the TIR condition in (2.6), the transverse component of the wavevector allows propagation for

$$k_t(a) \leq k_{t,\,\mathrm{max}} = k_0 \mathrm{NA}, \tag{2.13}$$

where k_0 is the vacuum wavenumber, and NA is the numerical aperture of the fiber. An approximation of the number of modes for optical fibers is given in [47]

$$M \approx \frac{1}{2}\left(\frac{\pi}{\lambda} a(z)\right)^2 \mathrm{NA}, \tag{2.14}$$

so that as a decreases, so does the number of guided modes [48]. Incidentally, it is worth noting the proportionality of the number of modes with λ^{-2} in both optical fibers and rectangular waveguides, but the difference in proportionality with the numerical aperture, as seen in (2.9).

In optogenetics, the required optical intensity to activate the neural response can vary. Still, a common target value is about $1\,\mathrm{mW/mm}^2$ when using channelrhodopsin-2 (ChR2) [49], which is considered among the most efficient opsins in terms of minimal optical intensity required to generate an action potential (described in further detail in Section 2.5.1). While this value can be obtained by arbitrarily increasing the input power, one must also account for the cell damage threshold, which sets an upper value on the intensity that can be safely used inside tissues. It is common to use the end of a silica optical fiber for stimulation. By using an input optical intensity of $100\,\mathrm{mWmm}^{-2}$, which has been identified as a damage threshold for continued stimulation [50], the maximum distance from the tip with sufficient optical intensity is reached at about 2 mm. Depending on the cleaving of the fiber, the optical distribution can be modified. While advanced mappings of the light distribution have been generated for various applications, using the Beer-Lambert equation is still used extensively for its ability to provide a quick, reliable estimate of the optical intensity.

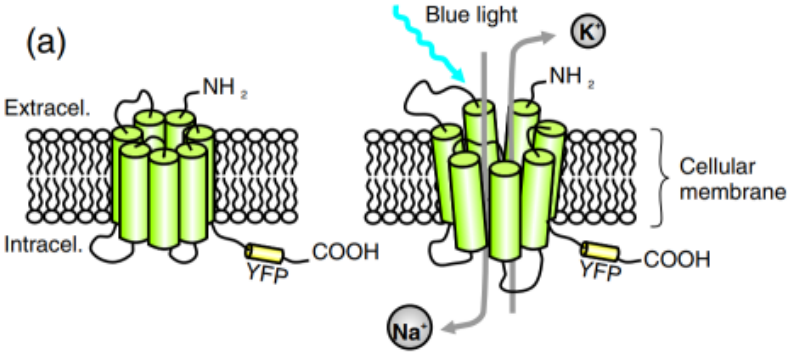

Figure 2.3: Schematic representation of a transmembrane channelrhodopsin protein in its closed (left) and opened (right) configurations upon blue light illumination. Reproduced from [11].

2.4 Optogenetics

As briefly reported in the introduction, optogenetics modulates the response of opsins, namely proteins that behave as ion gates upon light excitation. Figure 2.3 shows a schematic representation of the ion gate mechanism. The growth of the field of optogenetics was mainly triggered by the development of single-component optogenetics by using channelrhodopsin-1 (ChR1) [51] and ChR2 [52], two microbial light-gated cation (positively-charged ion) channels found in the green alga *Chlamydomonas reinhardtii*. ChR2 was shown to open rapidly upon absorption of a photon, with the peak absorption in the blue region (470 nm), but nowadays, there are light-sensitive proteins covering the full visible spectrum [11]. Other rhodopsins achieve the opposite; namely, they inhibit ion transport upon light absorption [23]. While optogenetics has focused on the activation mechanism for a long time, the sensing aspect is equally important, especially to achieve multimodal mapping of the brain function [11].

The generated photocurrents depend not only on the selected opsin but also on other parameters, such as the targeted cell type and the optical intensity. Although ChR2 has been the preferred tool for targeted light activation, research has investigated other rhodopsins with increased light sensitivity to avoid the likelihood of cell damage under the photon flux required for ChR2 activation ($10^{18} - 10^{19}$ photons s^{-1} cm^{-2} at 480 nm) [53–55].

Optogenetics tools also include photosensitive proteins that exhibit fluorescence under selected environments [11]. Two common examples are voltage-sensitive fluorescent proteins (VSFPs), which change their fluorescence output as a function of the potential through the cellular membrane [56] and calcium-ion (Ca^{2+}) sensors for visualizing intracellular signaling activity [57].

There are three main approaches to expressing the photosensitive opsins in selected tissue regions of the spinal cord [26]. First, transgenesis consists of breeding rodents to specifically express opsins from birth. However, many genetic lines are not fully characterized in the spinal cord, and further studies are needed to allow for finer control of the spinal cord and the peripheral nervous system. Second, cellular transplantation may be effective to achieve greater specificity of expression because cells can be sorted before the transplant. Finally, viral vectors can infect specific cells and introduce genes to restrict the deoxyribonucleic acid (DNA) delivery to defined neurons [26]. However, this

delivery is often performed in a separate surgery from the implant, followed by a patient observation period of several days [25, 50, 58]. Viral vector-mediated gene delivery is the most common for optogenetics, thanks to its cell-type specificity, long-term expression, and safety profile.

2.5 Electrophysiology

Monitoring cellular activity when stimulating cells is important to test whether the stimulation works as expected. The activity in the central nervous system can be monitored in various ways, such as optical functional imaging or magnetic resonance imaging [11]. One of the most popular methods, however, is electrophysiology. Broadly speaking, electrophysiology is the science and technique of studying the electrical phenomena that play a role in living creatures, such as the membrane potential of living cells [59]. The signals characterizing these organisms may be slow changing (typically due to a change in the concentration of a chemical substance) or short, transient peaks called action potentials or spikes, which are caused by the switching of ion gates in the membrane of neurons or other electrically active cells. In extracellular recordings with wide-tip electrodes, the recorded signal contains more than one spike train, and its amplitude is given by a collective contribution of multiple neural sources, the so-called multi-unit activities. On the other hand, a suitably small electrode can typically record the activity of a single fiber nerve.

Electrophysiology offers high temporal and spatial resolution by using electrodes, often sampling at more than 20 kHz and probing activity at the cellular level, and extracellular recording is noninvasive to cells and does not require photochemicals [11]. Electrodes are, however, sensitive to photoelectric artifacts, cross-talk between channels, and signal degradation, and they can cause tissue damage when implanted. Electrical recordings have the benefit of a fine spatial resolution (less than 10 µm), sub-microsecond temporal resolution, and good sensitivity (greater than 10 µV). On the other hand, the selectivity of the recording is limited and requires pharmacology to determine the contributors to the potential [60].

2.5.1 Action potentials

The action potential is a transient (less than 1 ms) increase of the membrane potential, which moves from the initiation point to the terminals of the axons (the fiber nerves that project the electric signal from the neuron along the body) [61]. The action potential is caused by changes in the permeability of the axon membrane to sodium and potassium ions, thanks to proteins called ion channels. While action potentials occur in several types of cells (such as muscle cells), the focus will be given to neurons, where action potentials are also known as nerve impulses or spikes.

All animals need to convert neural signals into trains of action potentials to send them through nerve fibers [59]. Most spike trains are irregular; therefore, a series of action potentials is considered a stochastic point process [59]. Figure 2.4 [62] shows the typical shape of an action potential. Any cell is, in general, electrically polarized; that is, it maintains a potential across the plasma membrane, known as resting potential. When a synaptic input perturbs the cell, the so-called depolarization phase occurs. When depolarization is strong enough to overcome the threshold potential, an action potential is triggered, abruptly increasing the membrane potential. After reaching the peak, the

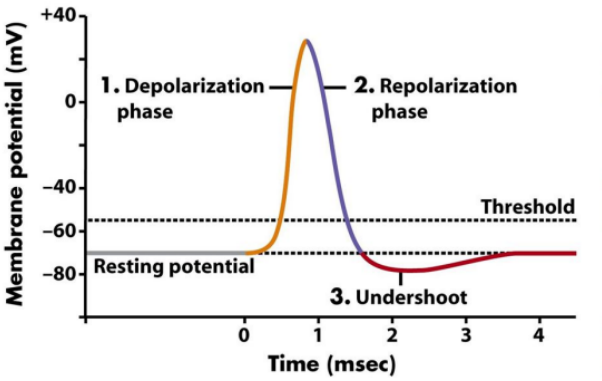

Figure 2.4: Typical action potential shape and phases. Reproduced from [62].

potential abruptly decreases, usually to a lower voltage than the resting potential, before it returns to the initial value. The duration of an action potential is of few milliseconds. While the shape, amplitude, and frequency of action potential highly depend on the type of neuron, all action potentials in a given cell have approximately the same features.

Individual action potentials are picked up with the so-called single-unit recordings, also called single-neuron recordings. These recordings measure the electric response of a single neuron using a microelectrode, which records the change in voltage as a function of time. The microelectrodes must have a fine tip (about 1 µm) and be impedance matching [63]. Intra-cellular single-unit recordings occur within the neuron and measure the voltage change across the membrane during action potentials, providing information about the resting potential, the postsynaptic potentials, and the spikes through the axon. Extracellular recordings, on the other hand, occur when the microelectrode is close to the cell surface and only provide spike information, which is typically recorded within a distance of 140 µm [64]. Single-unit action potentials cover distinct frequency bands from a local field potential (LFP) (typically < 100 Hz for LFPs and >250 Hz for single-unit action potentials) [64], hence they can be separated by analog or digital filtering. When the tip of the microelectrode is larger than 1 µm, the electrode might record the activity generated by several neurons, as their spiking activity partially or completely overlaps. This type of recording is referred to as multi-unit recording, and it is characterized by lower-frequency signals compared to single-unit action potentials [64]. As the microelectrodes become even wider, the action potentials become more and more difficult to record, while the low-frequency local field potentials start to appear.

2.5.2 Local field potentials

A LFP is a type of extracellular signal that reflects a dynamic flow of information across neural networks [65]. It is a composite signal that receives contributions from multiple neural sources, and it is generated in nervous and other tissues by the synchronized electrical activity of cells in the tissue. High-frequency electron oscillations are typically attenuated more than low-frequency with distance; hence, the LFP is the strongest at frequencies lower than 300 Hz [63]. While the term local might hint at a strong sensitivity to spatial features inside the tissue, LFPs are, in fact, nonlocal, as the rate of decay of the field potential is given both by the spatial extension and by the internal

distribution of ion charges within the source. Although the properties of electrodes might have some impact on the recorded signal, the electrodes sense any field potentials at their proximity, and it is usually the local geometry of the source and the electrical properties of the medium that govern the LFP decay rate [66]. Since the signal results from the superposition of multiple sources, it is generally possible that the highest amplitude is found at a distance from a source. Because of its greater stability compared to single-unit action potentials, it is often used for long-term experiments and clinical applications [63, 65].

Neural oscillations, also known as brain waves, are rhythmic patterns of neural activity that arise from local field potentials in the central nervous system, which are usually analyzed with an electroencephalogram (EEG), an inexpensive technique used to monitor the state of the brain without the need of an implant [67]. Nevertheless, brain waves can also be recorded with microelectrodes. The most common analysis approach for low-frequency neural oscillations is a power spectral analysis, which usually divides the spectrum into five bands:

1. Delta waves (0-4 Hz). They include the lowest frequency component and are usually sent during sleep, in infancy, or in serious organic brain diseases. Animals have a more widespread activity within this range.

2. Theta waves (4-7 Hz). They mainly occur in the parietal and temporal regions of children's brains. In adults, it is associated with emotional stress or certain stages of sleep.

3. Alpha waves (8-13 Hz). Alpha waves are typically recorded during consciousness for an awake but relaxed person with closed eyes.

4. Beta waves (13-30 Hz). Beta waves are usually further classified into Beta I (13-20 Hz) and Beta II (20-30 Hz). The former appears together with alpha waves, while Beta II appears only during intense mental activity and tension.

5. Gamma waves (30-150 Hz). The spectral power density of this band is generally low, and it is often filtered out of the signal to remove noise. However, it may indicate cognitive function and arousal in clinical applications.

2.5.3 Electrodes

Electrodes have been the main component in stimulating or recording neural activities. Their working principle varies depending on the technique, and two main classes of electrical recording can be distinguished: noninvasive electrodes and implantable electrodes [63]. Noninvasive electrodes are also referred to as EEG electrodes, as they are employed by this technique. EEG electrodes are further divided into wet, dry, and non-contact electrodes, depending on whether the medium surrounding the electrode is a conductive, adhesive gel, the electrode is placed in direct contact or slightly penetrates the scalp without any sticky matter, or with a small spacing between the electrodes and the skin. Non-contact electrodes dramatically reduce the preparation time, but the small signal amplitude is highly susceptible to motion artifacts. By varying electrode types and bandwidth, it is possible to record single units, multi-units, local field potentials, and more [11].

Implantable electrodes are surgically implanted on the surface or penetrated into the tissue to measure electrical activity at a higher resolution, enabling recording down to the individual cell. Non-penetrating electrodes are implanted on the surface and thus typically flat-shaped, and they are used for less invasive approaches in techniques such as epicranial EEG, and epidural or epicortal electrocorticography (ECoG) [63, 68]. These electrodes are often fabricated on rigid substrates, although recent advances have proved their potential when using biocompatible, soft substrates [68, 69]. However, the spatial resolution for these electrodes is too low for single- or multi-unit recordings.

On the other hand, penetrating electrodes are needle-shaped and are used to measure action potentials or local field potentials. These electrodes are typically divided into glass micropipettes, filled with an ionic solution to make them conductive on the tip, or metal microwires, insulated except for the tip in contact with the tissue. Metal microwires have critical advantages over glass micropipettes for measuring action potentials because they have a lower impedance at high frequencies, a high signal-to-noise ratio, and mechanical properties more compatible with brain implantation. On the other hand, the main disadvantage of microwires is the possible inflammatory reaction in the tissue, making some of them (such as silver, copper, and iron) toxic [70]. Some metals, such as tungsten, have good biocompatibility and mechanical properties, and the first in-vivo multi-neural recording with tungsten wires dates back to 1967, as the stiffness was large enough for them to be guided inside rabbit brain tissue without a supporting rod [71]. The drawback of a stiffer electrode is inflammation and risk of neural damage due to the large mismatch between Young's modulus (namely the ratio between the applied stress and the axial strain, quantifying the stiffness of a solid material) of metals (tens or hundreds of GPa) and of the brain tissue (about 3 kPa) [63]. To counteract this, metal surrounded by a flexible polymer with a sharp tip is commonly used to implant thin, flexible multi-electrode arrays in the brain.

Electrodes are typically tested via electrochemical impedance spectroscopy (EIS), a spectroscopy technique consisting of the measurement of the complex impedance of an electrode in an electrolyte solution. This parameter is a good indicator of how high the signal-to-noise ratio (SNR) in tissue can be. If the impedance is too high, there will be a high thermal noise in the measurement due to the generated Joule heating, and the high impedance will limit the flow of current. On the other hand, when the impedance is very low, the resulting small voltage signals can easily be overwhelmed by noise, which reduces the SNR and decreases the measurement precision. Further information about EIS can be read in Section 5.2, where the experimental setup used in the project is presented.

2.6 Optrode design

There are two fundamental elements needed to build a functional optrode: a way to convey light into the regions to be stimulated (for example, by the optical waveguide or the optical fiber) and a way to convey the electric signals from the neurons to the outside of the implant, to be able to record it (for example, by the metal microelectrodes). The challenge in building the optrode primarily consists in incorporating these two elements in a compact geometry that is robust yet flexible and biocompatible.

Original optrode designs combined commercial optical fibers with extracellular electrodes [14], obtaining a simple, low-cost design that can be integrated into any electrophysiological recording

setup. Alternative designs feature a glass pipette electrode (see Section 2.5) to record the electrical response and guide light simultaneously; the attenuation is considerably higher than an optical waveguide but can be compensated using a higher input power. Other methods include tapered optical fibers, whose illumination volume can be enhanced by tuning the radial profile of the fiber, as further explained in the previous section.

Advanced geometrical and material designs might include multiple recording sites or light stimulation sites using multiple electrodes or scattering points, respectively [16]. Typically, these optrodes are fabricated by embedding the electrodes directly in the waveguide structure through techniques such as plasma etching and physical vapor deposition. Other fiber designs might integrate the electrodes during the preform phase and draw them with materials of compatible thermal properties. Some designs even include drug delivery channels in a multifunctional fiber, thus enabling the electrical, optical, and chemical interrogation of a neural circuit with a narrow and flexible polymer probe [72]. However, the compatibility of the electrode and the waveguide material is critical. With polymers such as PMMA and PC, whose drawing temperature is typically around 200 °C, metal alloys containing tin or indium have been used for their melting point close to this temperature range. Alternatively, metals with much higher melting points can be considered for convergence thermal drawing, where microwires at the final size are fed independently from a preform with holes. Tungsten microelectrodes, for example, are often used for their relative stiffness, their biocompatibility, and their ability to form stable ion interfaces with the surrounding tissue, which improves the electrophysiological signal-to-noise ratio in clinical studies [73]. Moreover, the impedance of tungsten microwires is generally in the desired range to obtain a good SNR.

It is worth mentioning that the properties of the illumination source are also important when designing a system for light stimulation. Most importantly, one must consider factors such as the emission wavelength, optical intensity, and modulation properties of the source [11]. Moreover, it is necessary to account for the so-called photoelectric artifacts, which arise when a metal is exposed to light whose energy is above the so-called binding energy, thereby freeing electrons that can generate measurable currents. These artifacts are particularly relevant when stimulation and recording sites overlap, as the optical intensity will be particularly high. Stacked metal layers could also be a source of photoelectric artifacts [20]. In a metallic-confined waveguide, propagating and evanescent modes generate a surface current density on the metallic cladding, potentially generating spurious electrical signals. To mitigate the photoelectric artifacts, one can typically decrease the light intensity or consider using non-metal electrodes, such as glass micropipettes, which are free from photoelectric artifacts [11]. Finally, the optrode design will also depend on the type of targeted optogenetic study. The mobility is unimportant for an acute experiment where the species is restrained or anesthetized, and the optrode can be tethered for optical power delivery and signal recording. However, in chronic experiments where the patient moves freely, it becomes important to consider lighter-weight cables, rotary joints, and even wireless options, such as magnetic induction-powered micro-LEDs.

Chapter 3

Numerical simulations and modeling

This chapter presents the results of the numerical simulations carried out to model the optical properties of the designed waveguides for the neural interface. The simulations were carried on with Comsol Multiphysics® 5.6, with the Ray Optics and the Wave Optics modules. Two model types were primarily used: 2D and 3D models. The main advantage of the 2D model is the drastically reduced simulation time. By assuming that a waveguide is either infinitely wide or long, however, several features of the device cannot be simulated. The 3D model, on the other hand, is much more precise and reliable in predicting the behavior of a device such as the fibertrode, but the required computational power increases by several orders of magnitude.

Given the geometry of the device (whose cross-section extends over hundreds of wavelengths), the wave optics simulations required a vast number of mesh elements and were generally run with high performance computing (HPC), a technology that uses clusters of powerful processors in parallel to solve complex problems at high speed. The DTU HPC cluster is an IBM LSF cluster, and it is provided by the DTU Computing Center (DCC). DTU students and employees can run simulations by connecting to the LSF cluster via ThinLinc, from which jobs can be sent to the cluster through console commands over a Linux interface.

Section 3.1 defines the terms and concepts mentioned throughout the chapter with Comsol Multiphysics. Then, Sections 3.2 and 3.3 present the main results with the 2D and 3D models, respectively. The chapter ends with a description of the steps to build one of the models in Comsol Multiphysics.

3.1 Comsol Multiphysics

Comsol Multiphysics is a software package based on the finite element method (FEM), a method for solving differential equations by dividing an extensive system into so-called finite elements by discretizing the space into a mesh. Simple equations that model the finite elements are combined into more complex equations that govern the whole system, and the solutions are found by minimizing an error function [74]. In this section, a brief introduction to the terms used in the chapter will be given. The section is subdivided into themes, from the modeling geometry to the mathematical solvers needed to simulate an interface.

3.1.1 The geometry

Building a model begins with the geometry itself, which can be either built from scratch using the primitives integrated into the software (such as rectangles, circles, polygons for 2D geometries or blocks, spheres, and cylinders for 3D geometries) or by importing computer-aided design (CAD) files. Adding primitives to the modeling space defines domains and boundaries. Domains have the exact dimensions as the model; hence, they are surfaces in 2D and volumes in 3D models. Conversely, boundaries are defined between adjacent domains; hence, they are lines or curves in 2D models and surfaces in 3D models. Each domain requires a defined material and mesh, while boundaries are primarily used to define the external boundaries or the ports in the model.

3.1.2 Materials

Each domain in the model must be assigned a material. In the electromagnetic waves package, the most critical parameter of a material is naturally the refractive index, which defines the dispersion and absorption properties of light. Comsol has an extensive library of optical materials, which includes all the materials considered in the project: PMMA, PC, copper, tungsten, indium, tin, air, and water. All materials have information about the real refractive index n' at optical frequencies, but only some also come with the imaginary part n'' of the refractive index. For example, in the default library, water and metals have both n' and n'', but organic polymers such as PC and PMMA only have n'. This means that the solution of the wave equation will not account for intrinsic absorption losses inside these materials. While such absorption is negligible for short propagation distances, to improve the accuracy of a model, it is possible to manually import the data of complex refractive indices, which can usually be found in articles or databases such as [75].

3.1.3 Meshing

Meshing is dividing the 2D or 3D modeling space into finite cells. It is possibly the most challenging part when building a simulation model, to the point that some have argued that rather than science, it is an art [76]. Not only is it what defines the quality and reliability of a simulation, but also it defines its computational viability, which, despite the HPC, can be easily compromised by a fine mesh.

Generally, for a high-quality simulation, the frequency-domain wave optics physics requires several mesh elements that are approximately $\lambda/3$ to $\lambda/4$ in size, where λ is the simulation wavelength. However, due to the size of the device, this corresponds to meshing a geometry of hundreds of micrometers per dimension, which can easily mean billions of elements in a 3D model. Not only does this require remarkable computational power, but it also needs an inaccessible amount of random access memory (RAM) while computing, even when using an HPC. Consequently, it is necessary to either decrease the simulation volume or increase the size of the mesh elements. From the simulations run throughout the project, it seems that the former is a more reliable approach, as a coarse mesh can lead to visibly-unphysical results.

Several types of meshes can be used in Comsol Multiphysics. One must first distinguish between structured and unstructured grids to understand their usage. The formers are highly space efficient,

thanks to the regular connectivity, and thus have the advantage of better convergence and higher resolution. Conversely, unstructured grids allow for any possible element compatible with the dimensions of the solver, which usually makes them more inefficient yet versatile. Below, a brief explanation of those used in the project is given.

- **Triangular meshes.** Free triangles are unstructured meshing elements used in 2D domains or 3D boundaries. They can achieve much higher accuracy than rectangles of equal side length and are the simplest to set up. They are typically configured by setting the maximum element size in free space; in materials with different refractive indices or in the proximity of smaller geometrical features, the element size will resize automatically. However, free triangles are also the most computationally-demanding elements.

- **Tetrahedral meshes.** A tetrahedral mesh is a 3D generalization of a triangular mesh. Tetrahedra achieve the highest precision in a three-dimensional model, but they significantly increase the computational complexity and size of the model.

- **Mapped meshes.** Mapped meshes are structured; hence they can be much coarser and obtain a comparable accuracy to unstructured elements, thus reducing the size of a model and the computational complexity. They are particularly beneficial for the electromagnetic waves, beam envelopes (ewbe) physics, given that the slowly-varying envelope ensures the mesh will be fine enough to resolve the physics of the electromagnetic wave. Mapped meshes require a source and destination edge between which the meshing elements are mapped, and they are typically configured by specifying the number of longitudinal and transverse elements for a given domain.

- **Swept meshes.** Similarly to a tetrahedron for a triangular mesh, a swept mesh is the generalization of mapped meshes for a 3D geometry. Swept meshes require one or more source and destination faces between which the meshing elements are swept.

By default, triangular or tetrahedral meshing elements are created with a size of $\lambda/5$ in free space and become proportionally smaller in domains with higher refractive index. Structured elements such as mapped and swept meshing elements, on the other hand, come with a default number of 10 longitudinal and transverse meshing elements. Depending on the geometry, it is often worth trying to change these parameters, even by selecting specific finite element sizes for each domain, to optimize the performance and the quality of the simulation.

3.1.4 Boundary conditions

Boundary conditions are a set of additional constraints to the solution of the partial differential equations in the model. Boundary conditions are typically defined on the outer boundaries of the simulation geometries. Examples of common boundary conditions are the perfect electric conductor (PEC) and the perfect magnetic conductor (PMC). The former assumes the boundary is a perfect conductor with zero resistance and sets to zero the parallel component of the electric field and the orthogonal component of the magnetic field with respect to the interface. Conversely, the latter zeroes the orthogonal component of the electric field and the parallel component of the

magnetic field. PECs and PMCs should be selected according to the polarization of the input field to impose the desired value of the field at the boundaries in metals or other highly-reflective materials.

Another important type of boundary condition is the so-called perfectly matched layer (PML), which belongs to the artificial domains. PMLs are useful when the physical domains of interest extend indefinitely, where PEC or PMC boundary conditions are insufficient. A PML mimics open, non-reflective infinite domains, and as such, it is usually used at the edges of a model. They are critical when instead of a core/cladding fiber, one deals with a single-material waveguide with scattering elements, from which a large part of the light escapes the confined modes. PMLs are typically defined in layer domains, namely domains created by introducing a layer of a given thickness around another precedently-defined domain.

3.1.5 Solvers and studies

Several solvers were used for the simulations in this project. For the ray optics simulations, the *geometrical optics* (gop) physics was used. The ray optics module includes the geometrical optics interfaces, which trace a large number of rays through the modeling domain by solving a set of six ordinary differential equations for the position $\mathbf{q}$ and wave vector $\mathbf{k}$, which were derived from the short-wavelength limit of a plane-wave solution of Maxwell's equation [77]. The material discontinuities introduce additional conditions following the laws of geometrical optics (reflection, refraction, and diffraction). The domains through which the rays travel must be meshed, the mesh can be very coarse, except for the proximity of curve surfaces. Hence, the advantage of the ray optics module lies in the computational efficiency, which enables the finding of solutions for models considerably larger than the ones of the wave optics package.

For the wave optics module, the electromagnetic waves, frequency domain (ewfd) and the ewbe physics are available in both 2D and 3D models. The frequency domain solver computes the full-wave form of the Helmholtz equation

$$\nabla \times (\nabla \times \mathbf{E}) - k_0^2 n^2 \mathbf{E} = 0 \tag{3.1}$$

$$\mathbf{E}(x, y, z) = \tilde{\mathbf{E}}(x, y) e^{-i\beta z} \tag{3.2}$$

via the FEM, which is used to approximate the partial differential equations by discretizing the model. While (3.1) accounts for non-homogeneous fields, in this case, both permittivity and permeability are constant in the volume of any given material, hence they simplify to the result shown in (2.5). The frequency-domain solver does not implement any approximation for the field and resolves both the envelope and the field oscillations given by the phase. On the other hand, the beam envelopes solver solves the Helmholtz equation by assuming the field envelope $\tilde{\mathbf{E}}$ varies slowly. This allows factoring out the phase $e^{-i\beta z}$ from the Helmholtz equation and resolving the slow envelope only. Because of this process, the required computational power can decrease considerably, enabling the solution for larger models.

Each model contains several study presets, depending on the geometry and the physics. In this project, the used preset studies were the following:

- Mode analysis. This step is only available in 2D and 2D axisymmetric cross-sections of waveguides, where it is used to find the cross-sectional distribution of allowed propagating

modes. It is used to analyze the propagation modes in optical waveguides, determining the characteristic modes that can propagate through the structure. One can specify the range of modes to be analyzed and add additional constraints, such as the desired number of modes or a specific propagation direction.

- Boundary mode analysis. Whether it is active or not, each port requires a boundary mode analysis step in the study, which specifies the port number, the mode number, and the effective index of the mode to be sought. It is used in both 2D and 3D models whenever ports are defined.

- Frequency domain. After obtaining the eigenmodes with the previous study steps, the frequency domain study can also be performed to obtain the field distribution for a given mode, calculate the transmission and reflection coefficients, and extract other results. It is used in both 2D and 3D models.

- Ray tracing. The ray tracing steps are a particular case of the time-dependent study step; hence, it works in the time domain and calculates the propagation of individual rays across the geometrical model, accounting for the refraction and dispersion properties of the specific materials. The study step thus requires specifying the time steps, either in terms of absolute time intervals or path lengths. Stop conditions can also terminate the simulation whenever no active rays remain, or their intensity is negligible. A ray detector can also track rays that reach specific points or regions of interest in the system.

3.2 2D models

This section presents the main results from the simulated 2D models. Overall, the geometry of the interface could be modeled without reducing its size by running the simulations on HPC. However, the information that could be extracted was limited, as the optrode interface naturally extends over three dimensions, and 2D models are inevitably less accurate. They have nevertheless been used to support the development of neural interfaces, even in notable works [78]. 2D models are run under two different configurations. Cross-sectional models are used with the mode analysis study step to obtain information about the eigenmodes of the waveguides as a function of the geometrical parameters. However, they provide information only about some scattering properties of the waveguide. Conversely, the axial models are used with the boundary mode analysis and frequency domain study steps by defining ports in the model and calculating transmittance, reflectance, and absorptance from such ports. They are helpful in observing the scattering properties of the geometry, but they cannot resolve the different thicknesses and shapes of the three-dimensional elements.

3.2.1 Cross-sectional view

The initial modeling was done on a cross-sectional view of the waveguide, which can be helpful in the analysis of the mode profile distribution. The initial examples were simple circular fiber cross sections to get acquainted with the software. The initial software simulations featured a PC core and a PMMA cladding.

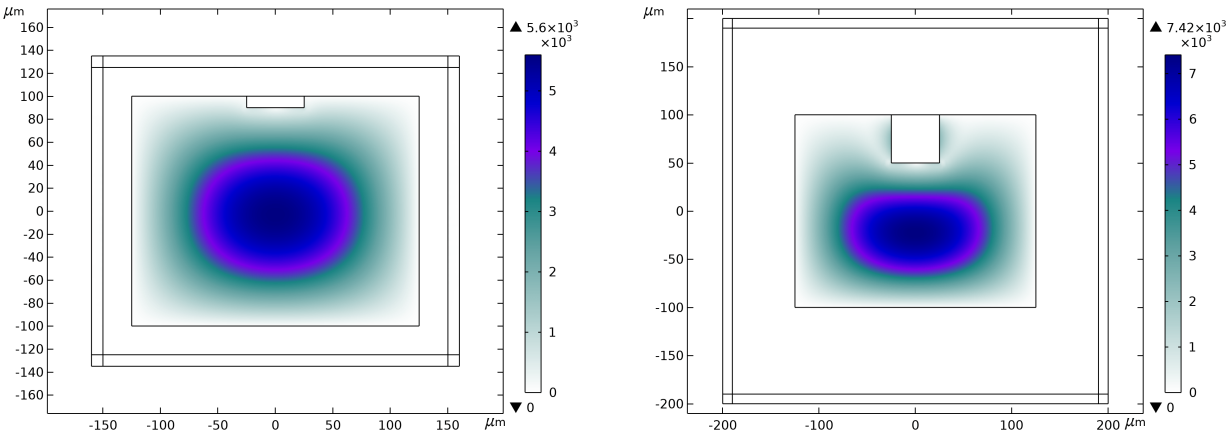

(a) $h = 10\,\mu\text{m}$. (b) $h = 50\,\mu\text{m}$.

Figure 3.1: Distribution of the electric field norm for the fundamental mode, for different height values of the electrode. The domains are PMMA (waveguide), tungsten (rectangular electrode), and water (outer domain).

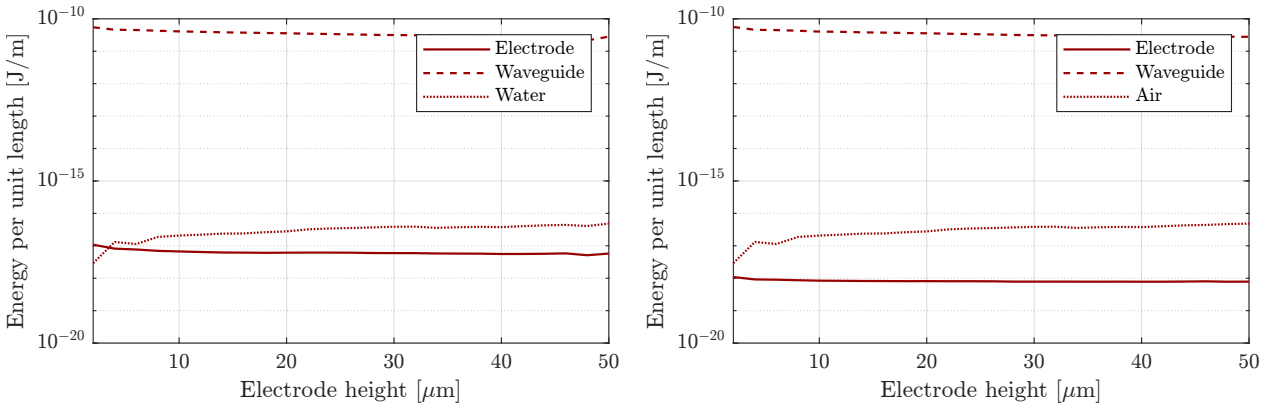

(a) Time-averaged energy density, water (integration). (b) Time-averaged energy density, air (integration).

Figure 3.2: Variation of the energy density as a function of the electrode size for the fundamental mode.

The model of Figure 3.1 features three domains: a rectangular waveguide made of PMMA, an electrode made of copper, and the environment is air. The air domain has a PML, which becomes important when removing the cladding domain; otherwise, the reflections lead to numerous artifacts. By comparing the electric field norm with different electrode heights h, such as these cases where $h = 10\,\mu\text{m}$ and $h = 50\,\mu\text{m}$, one can notice how the fundamental mode is deformed with increasing electrode height, and how the field concentrates towards the bottom and on the edges of the electrode itself. As will be shown later in 3D simulations, higher-order modes are affected even more by the presence of electrodes in the waveguide, and they cause the most scattering.

Figure 3.2 illustrates the energy density per unit length (the energy density is integrated over the two dimensions of the 2D model, thereby producing units of J/m) in the waveguide, electrode, and surrounding domains. First, Figure 3.2a first plots the energy against electrode height when the surrounding medium is water. From the gradual increase in the energy in the water domain, it appears that the rectangular electrode does introduce some extra scattering losses, which make

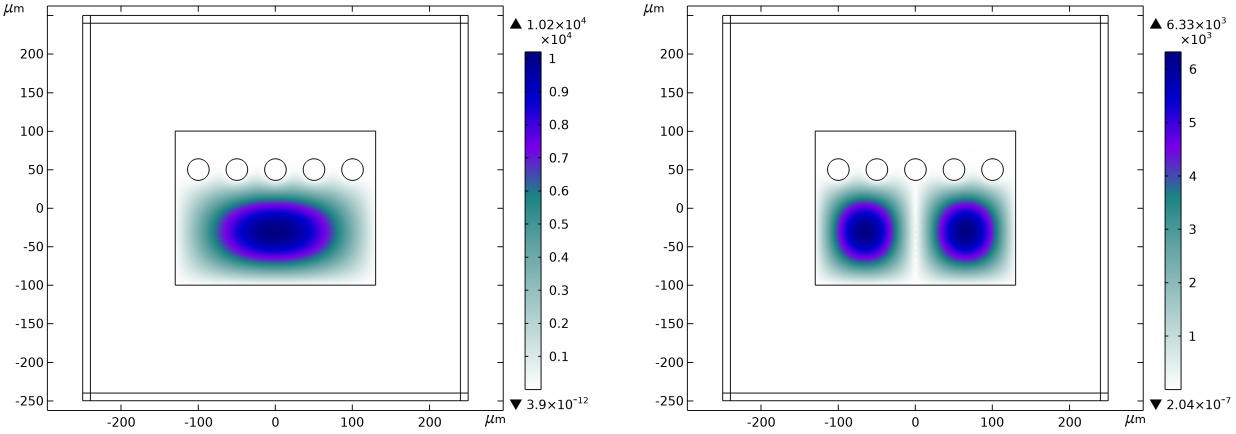

(a) Fundamental mode.

(b) First higher-order mode.

Figure 3.3: Distribution of the electric field norm for two modes in the PC-In waveguide. The domains are made of PC (waveguide), indium (five electrodes), and water (outer rectangle).

some light couple into radiative modes. Figure 3.2b then shows the same plot when the surrounding medium is air. While the trend closely matches the one for water, the energy density is decreased in the electrode in favor of a slight increase in the air domain. The difference, however, does not seem to be significant. It is worth remarking that while the difference between the two cases is negligible, it is expected to increase for higher-order modes, whose interactions with the electrode and surrounding domains are stronger.

After the first fabrication results with a PMMA waveguide and having modified the design of the waveguide, a new geometry for this simulation was proposed, as reported in Figure 3.3. Here, the two lowest-order modes are compared in the same geometry, characterized by a $250 \times 200\,\mu m$ PC waveguide and five indium electrodes in a water environment. The row of metal electrodes concentrates most of the field on the bottom of the waveguide for both modes; the mode features must become comparable to the size of the upper part of the waveguide for light to concentrate on this area. Incidentally, the legend shows how even between the fundamental mode and the first higher-order mode, there is a difference in the field intensity, which is slightly higher in the first case.

3.2.2 Axial view

The 2D axial simulations of the waveguide show the propagation direction and one of the two cross-section dimensions (in this case, the height). While some preliminary estimates of the scattering intensity were done with this model, it was mainly used to compare the results of the different solvers, ewbe and ewfd, as well as to gain familiarity with the meshing techniques. While the mode analysis of the cross-sectional view can calculate the eigenmodes even with very large geometries, the propagation of the electromagnetic field is much more computationally intensive and requires a higher degree of mesh optimization. The model itself shown in Figure 3.4 shows a $65 \times 20\,\mu m$ model size, which is considerably smaller than those shown in the cross-sectional simulations above. Nevertheless, these simulations had to be run in the HPC due to the stringent mesh requirements.

Due to the topology of the geometry, which contains a nonuniform domain (the hole), a structured

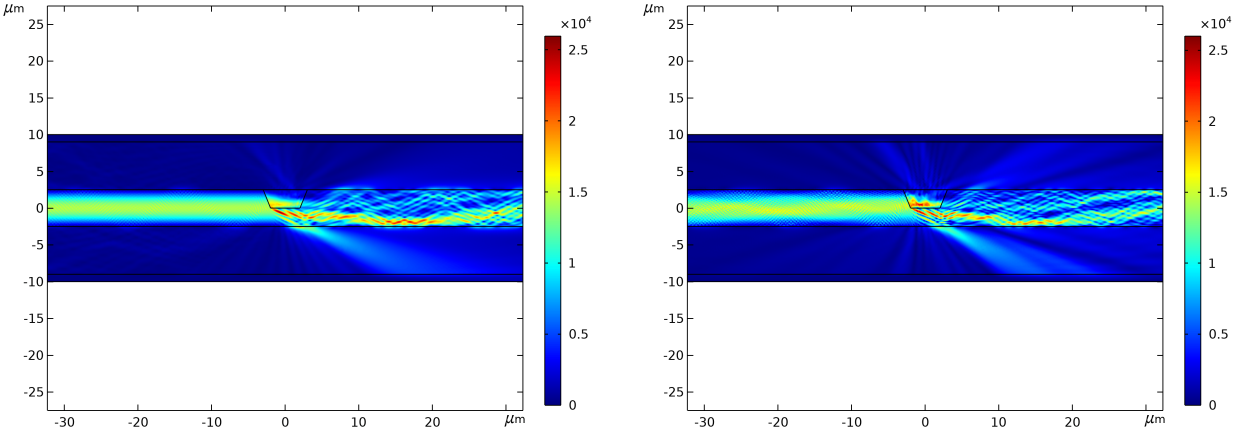

(a) Electromagnetic waves, beam envelopes (ewbe). (b) Electromagnetic waves, frequency domain (ewfd).

Figure 3.4: Scattered electric field when using the ewbe and the ewfd physics. The 4 µm-tall waveguide is made of PMMA and the environment of water.

grid could not be used to mesh the model entirely. The use of free tetrahedra significantly increases the finite element number, thus leading to the requirement of a larger dedicated memory. To somewhat reduce the memory requirements, the mesh was partitioned to have multiple regions: a swept mesh on the first and last thirds of the waveguide length, as well as in the PML, and free tetrahedra for the central portion containing the hole. By comparing the two different cases of Figure 3.4, it is possible to note some features better defined with the ewfd physics, such as the diffracted beams in the water domain. However, the main features are preserved in the more efficient ewbe, although the computational time and memory decreased only slightly. The following section provides a quantitative analysis of the scattering profile with a 3D geometrical model, thus obtaining more accurate results.

3.3 3D models

In principle, modeling in 3D opens up many more possibilities for improving the quality and accuracy of the model. However, with the wave optics package, the computational power, RAM, and storage space needed, even a portion of this device is far from the available resources, even accounting for the HPC. The 3D simulations are divided into geometrical and wave optics simulations; the latter are further divided into field distribution, scattering, and polarization analysis models. In all the following simulations, x is the propagation direction, y is the horizontal direction of the waveguide cross-section, and z is the vertical direction.

3.3.1 Ray tracing

A preliminary evaluation of the waveguide in three dimensions was carried out with the geometrical optics package. Figures 3.5a and 3.5b show the geometry built for the model: the waveguide is made of PC, the environment is water, and the five electrodes are metallic. Ten rays were released over 50 uniform cones on the input boundary over an angle of $\pi/6$ rad to ensure that the TIR condition upon reflection is met. Four ray detectors were placed on the external boundaries (top, bottom, side, and output boundaries), and the physics-controlled mesh was set to extra-fine. The *wall* feature of

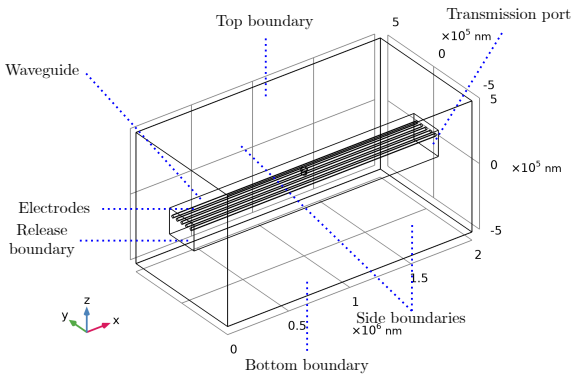

(a) 3D overview of the geometrical model for the ray optics package, with five electrodes.

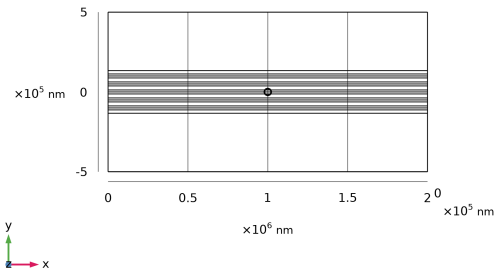

(b) Projection of the model over the xy plane, showing the hole position.

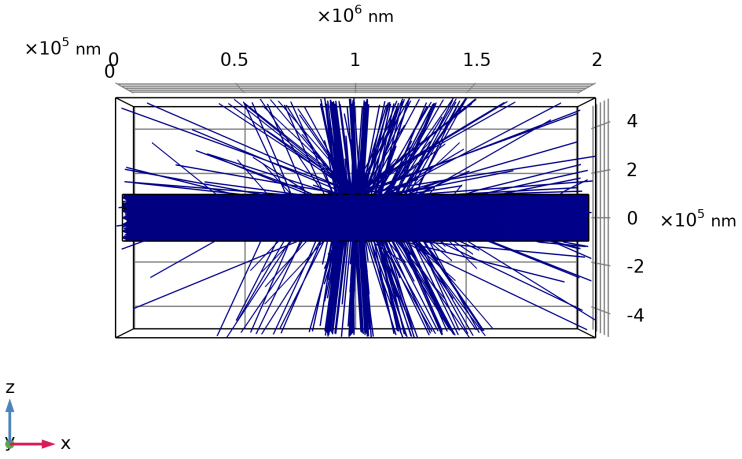

(c) Ray tracing simulation, showing the rays on the xz plane in the middle of the waveguide. The model overestimates the scattered intensity by the hole proximity.

Figure 3.5: Geometrical optics simulations in COMSOL Multiphysics.

the package (which freezes rays that impinge on selected boundaries) was used on all the external boundaries, and the specified wavelength for the ray dispersion was set to 650 nm.

The only study step needed is the so-called *ray tracing* step, which calculates the distribution of the released rays over a selected time interval – in this case, 1 ns. The rays can then be analyzed in terms of statistics or spatial distribution. Figure 3.5c shows an example obtained from tracing the rays of the model illustrated above, with the blue rays projected on a xz plane at the center of the waveguide. The central scattering due to the hole can be immediately noticed for the significant amount of secondary rays released upon scattering, which impinge on the upper, lower, and side boundaries.

From the ray detectors, the total number of rays impinging on the upper, lower, and side boundaries were 119, 108, and 226, respectively. In comparison, the number of transmitted rays is 420, which, if one were to take the number of rays as a measure of the optical intensity, would roughly correspond

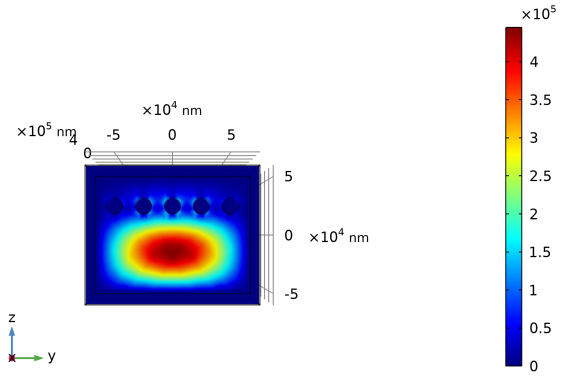

(a) Cross section of the fundamental mode, matching the results of the 2D model in Figure 3.3a.

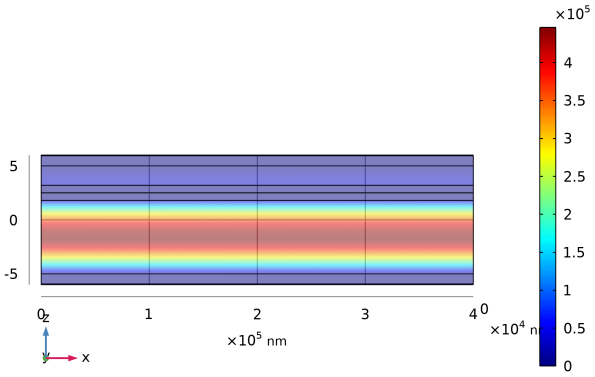

(b) Field propagation along the waveguide, as seen on the xz plane in the middle of the waveguide.

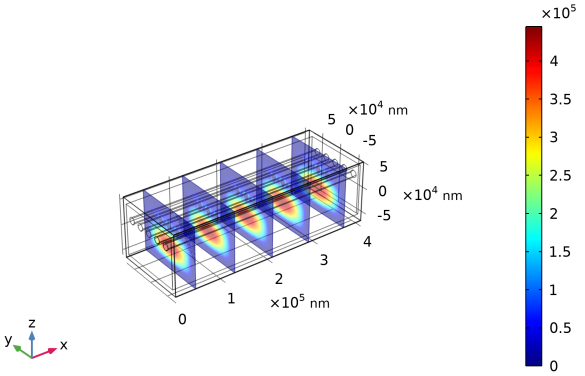

(c) Sliced cross-sections along the waveguide, showing the unperturbed profile of the mode.

Figure 3.6: Electric field distribution of the fundamental mode in a PC waveguide with five In electrodes in a 3D geometry. The cross-section ($125 \times 100\,\mu m$) is halved with respect to the modeled device due to computational constraints.

to a scattering of 51.9%. This estimate is far too high, as shown in the wave optics simulation and the experimental characterization. Hence the geometrical optics model was rapidly replaced by the more accurate (yet computationally intensive) wave optics package.

3.3.2 Field mode distribution modeling

The first tested geometry was a five-channel waveguide without holes, enabling efficient computation with a structured grid. In Figure 3.6, the model consists of a PC waveguide with a cross-section of $125 \times 100\,\mu m$ and five electrodes made of indium. By using a swept mesh in either ewbe or ewfd, it is possible to efficiently compute the mode profile and distribution for the fundamental mode (or any other mode of interest). As one can observe, the electric field is mainly concentrated on the larger part of the waveguide cross-section, and the five electrodes almost act as mirrors, given the weakness of the field on the region above them. The results thus match those found in Figure 3.3a when calculating the fundamental mode field distribution in the 2D geometry. Naturally, the distribution

is uniform along the propagation direction x, as no perturbations (e.g., holes) were introduced.

3.3.3 Scattering modeling

When using boundary mode analysis and defining ports in a model, COMSOL Multiphysics calculates the total transmittance, reflectance, and absorptance by default. For the two ports defined in the model (where Port 1 is the input port and Port 2 is the output port at the opposite end of the waveguide), the parameters give immediate information on the amount of reflected and transmitted light, which is of primary interest for this work. Similarly, the scattering caused by the hole was simulated by calculating the time-average power outflow on a surface boundary at the top and the bottom of the waveguide (the function *ewfd.nPoav* in COMSOL Multiphysics) and comparing it to the input power (which is by default set to 1 W).

Due to the change in the domain topology when introducing a hole domain, the mesh had to be created with free tetrahedra instead of swept meshes to reduce the computational power. However, this greatly decreased the model's maximum size, which had to be shrunk to the micrometer level. Figures 3.7a and 3.7b illustrate the $2 \times 2 \times 2\,\mu\text{m}$ model geometry and mesh, respectively. Each geometrical feature in the model was set to be proportional to the width of the waveguide w_c, including the hole size, the radius of the electrodes, the height, and the length of the core. Figure 3.7 shows a comparison of the electric field distribution between a model where $w_c = 1\,\mu\text{m}$ and $w_c = 2\,\mu\text{m}$. Due to the subwavelength features of the first model, it is clear that the modes have very different properties. In the first case, the concentration of the field around the metal electrodes (Figure 3.7c) and the exponential decay of the power along the axis (Figure 3.7d) suggest that a non-propagating mode above the surface plasmon polariton (SPP) frequency is excited. Let us recall that the plasma frequency of a metal can be modeled by the Drude-Lorentz model as

$$\omega_p = \sqrt{\frac{Ne^2}{\epsilon_0 m_0}}, \tag{3.3}$$

where N is the electron density, e is the electronic charge, ϵ_0 is the vacuum permittivity and m_0 is the electron mass. At the interface between a dielectric (the polymer waveguide) and a metal (the tungsten wires), the wavevector component along the interface is imaginary when $\omega_{\text{sp}} < \omega < \omega_p$, where

$$\omega_{\text{sp}} \equiv \frac{\omega_p}{\sqrt{1+\epsilon_d}}, \tag{3.4}$$

ϵ_d being the permittivity of the dielectric. In the case of tungsten ($\omega_p = 3.19 \times 10^{15}$ rad/s), the SPP resonance frequency with an interface of tungsten and PC ($n \approx 1.58$) gives $\omega_{\text{sp}} = 2.13 \times 10^{15}$ rad/s. Hence, visible light at 633 nm, corresponding to an angular frequency of 2.90×10^{15} rad/s, is within the range of no propagating modes. However, as the features increase in size compared to the wavelength, this evanescent mode is not excited, and the fundamental mode distribution is found again. This is mostly attributed to the decrease in the mode confinement by the proximity of the waveguide interface when the size of the waveguide is increased, which decreases the coupling efficiency of the observed mode. Additionally, when the waveguide size becomes large compared to the wavelength, the wavevector constraints for the excitation of this mode are usually no longer satisfied.

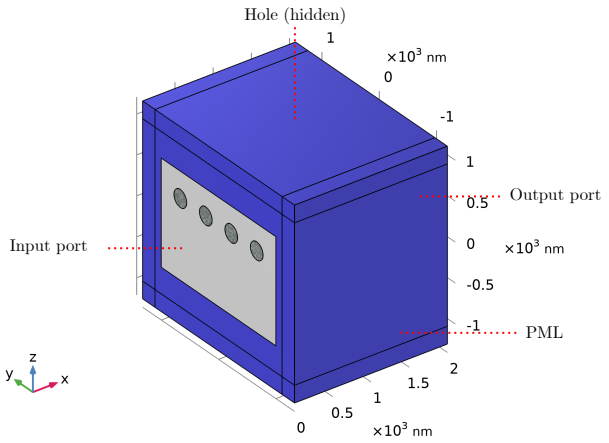

(a) 3D view of the model, with PC (grey), water (blue), and tungsten (black).

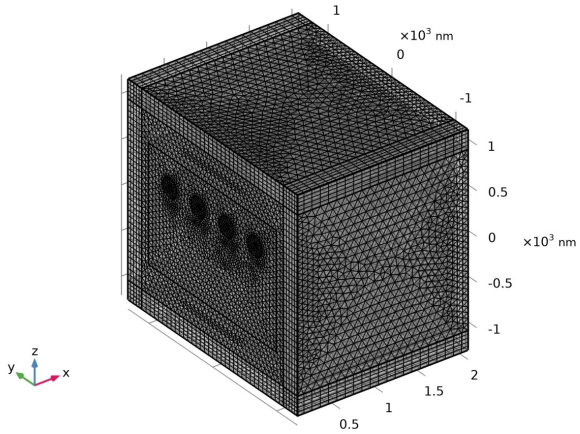

(b) Meshing of the model.

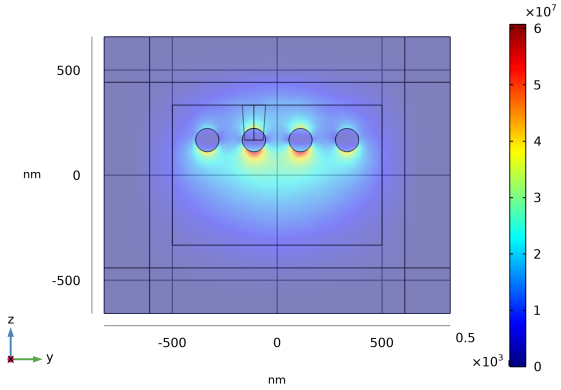

(c) Cross section distribution, $w_c = 1\,\mu\text{m}$.

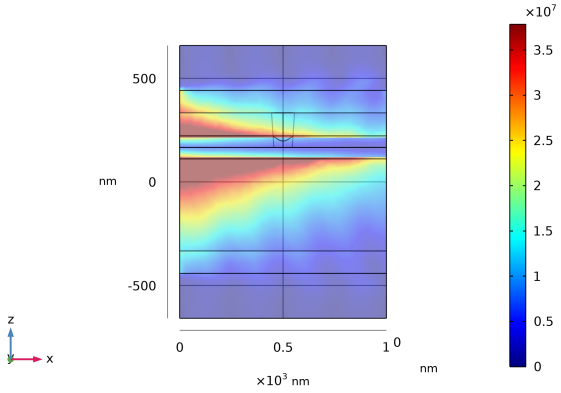

(d) Axial distribution, $w_c = 1\,\mu\text{m}$.

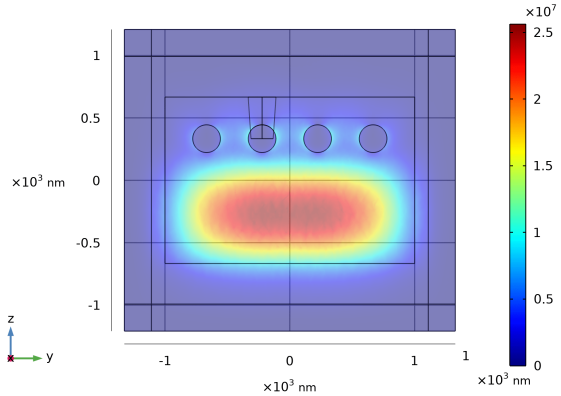

(e) Cross section distribution, $w_c = 2\,\mu\text{m}$.

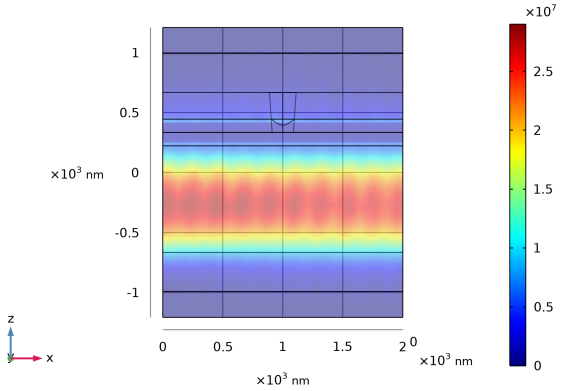

(f) Axial distribution, $w_c = 2\,\mu\text{m}$.

Figure 3.7: Comparison of the electric field distribution of the fundamental mode in a PC waveguide with four W electrodes in a 3D geometry and a machined hole, with the *ewfd* model.

A series of seven simulations with increasing model size (core width ranging from 1 µm to 4 µm) was run to compare the effect of the model size on the scattering effects of the fundamental mode. The results have been collected under Figure 3.8. From the field distribution, the propagating mode appeared at 1.5 µm; hence, all the larger models had the same distribution. This explains the difference in transmittance and absorptance between $w_c = 1\,\mu\text{m}$ and the larger simulations

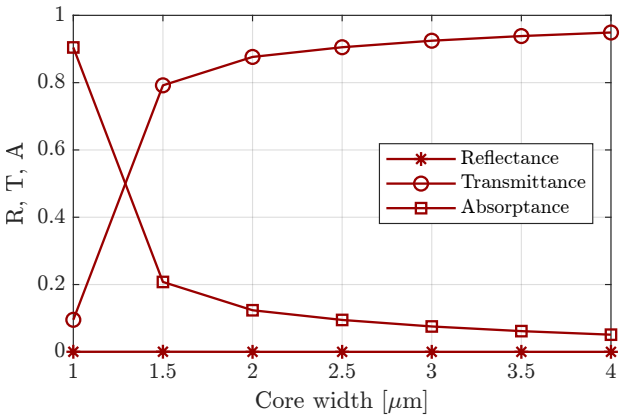

(a) Reflectance, transmittance, and absorptance.

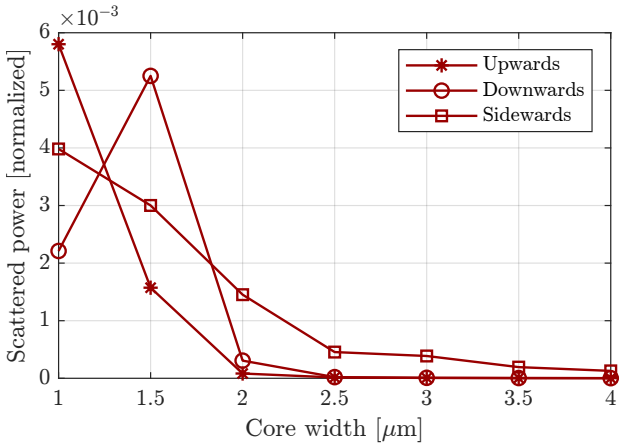

(b) Scattered power flow.

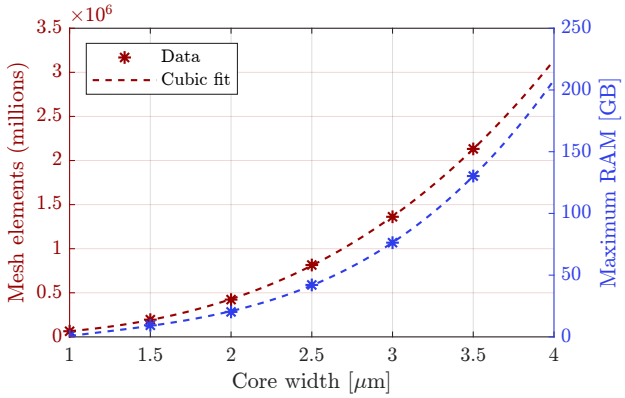

(c) Data of the computational parameters (dots), fitted by a cubic polynomial curve (dashed lines).

Figure 3.8: Numerical results of the fundamental mode for different sizes of a PC-W waveguide in *ewfd*.

(Figure 3.8a). Nevertheless, the absorptance generally decreases with the model's size, as less field is concentrated near the tungsten wires or the hole.

Figure 3.8b illustrates the optical scattering as a function of the model size, which, as previously explained, was calculated by integrating the power flow by the water domain surfaces before the PML. The power was divided into upward (corresponding to the surface above the hole), downward (below the waveguide), and sideward scattering. It is worth observing that the scattering in the horizontal direction dominates for the larger geometries and is followed by downward scattering. While the scattering direction of interest is upward (the stimulation region should match the region in contact with the electrodes, namely the one in the proximity of the hole), the device can still be used, as the waveguide can sustain high optical power without significant tissue heating.

Incidentally, although the scattered power is minimal, one must recall that higher-order modes (which make up the vast majority of power in a bulk waveguide such as this one) have a much different electric field distribution, which will also extend close to the electrodes, and particularly on the upper part of the waveguide. Thus, those modes will be scattered more significantly by the hole. Moreover, the ideal smooth surfaces of the waveguide, the interface with the tungsten, and the hole are highly different from the rough surfaces of an actual device, and the lack of impurities in the PC

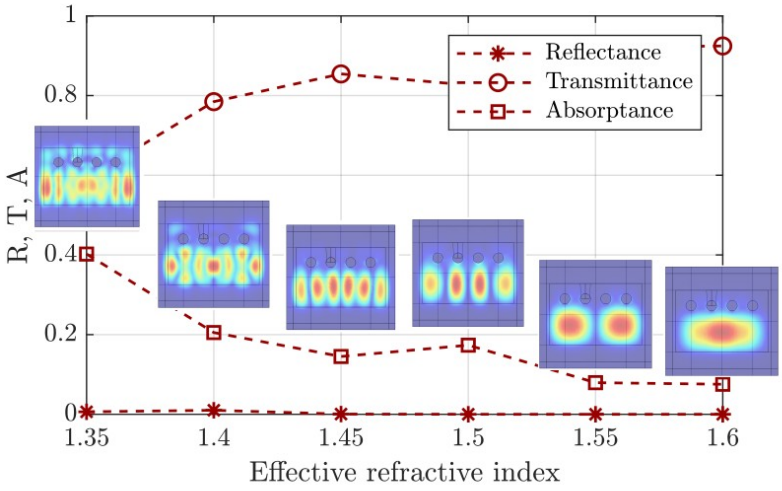

(a) Reflectance, transmittance, and absorptance.

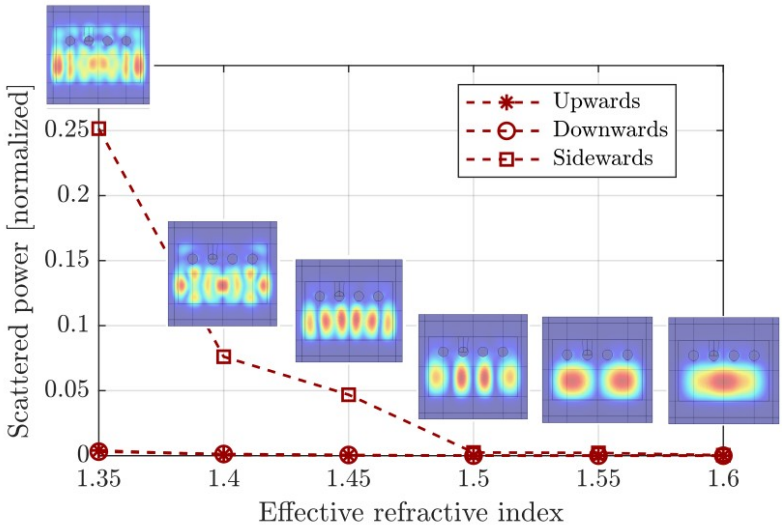

(b) Scattered power flow.

Figure 3.9: Comparison of the transmission and scattering for different modes of a PC-W waveguide with a core width of 3 µm in *ewfd*. The inset shows the mode field distribution at a given effective refractive index.

neglects the random intrinsic scattering points distributed along the fiber itself.

Figure 3.8c illustrates the computational challenges behind these simulations, namely why the simulations had to be stopped at a much smaller feature size than the actual device. Since the three dimensions of the model scale with the core width, the mesh elements, as well as the maximum RAM used by the model and the elapsed simulation time, are all expected to increase proportionally to w_c^3, namely the cubic power of the width. The cubic fit (dashed lines) confirms the hypothesis and shows why the maximum core width had to be stopped at 4 µm. Any increase of more than 500 nm above this value would have required more than 300 GB of allocated random access memory.

Higher-order modes generally feature much stronger scattering as they concentrate around the

holes and the electrodes. To show this, the effective refractive index of the mode was changed. This parameter is specified in each step of the boundary mode analysis and is usually set to the refractive index of the core when looking for the fundamental mode in an optical fiber or a waveguide. By default, the solver looks for the mode closest to the desired effective refractive index in absolute value. Hence, higher-order modes can be found by setting the effective index n_{eff} to a smaller value. For the modes to be confined in the waveguide and not radiative, the index must meet the following condition:

$$n_{\text{cl}} \leq n_{\text{eff}} \leq n_{\text{co}}, \tag{3.5}$$

where n_{cl} and n_{co} are the indices of the cladding and the core, respectively. For the simulations, n_{eff} was thus set at intervals of 0.05 from 1.35, the refractive index of water being 1.332 at a wavelength of $\lambda = 600\,\text{nm}$. The results of the computations for $w_c = 3\,\mu\text{m}$ are given in Figure 3.9, where the insets in the pictures show the respective field distribution of the calculated mode. From the value with the highest index (i.e., the fundamental mode), the field distribution is changing and becoming more complex. In particular, the mode at $n_{\text{eff}} = 1.35$ has a large component close to the hole, and as such, the scattering value is much larger than the other modes.

To further examine the scattering profile of each mode, the electric field was recorded in proximity to the waveguide (80 nm outside the waveguide boundaries), normalized to the maximum, and reported on a polar plot, as shown in Figure 3.10. The main scattering direction for the fundamental mode is toward the bottom of the waveguide, but as the order of the modes increases, so does the scattering intensity on the sides. In all cases, the scattering on the desired side (i.e., the top) is smaller than the other directions, as Figure 3.9b had anticipated. Nevertheless, the case for $n = 1.35$, the highest-order mode recorded in the simulation, has a considerable increase in the scattered field in the proximity of the hole, as the field distribution also shows. In this case, the scattering toward the top is stronger than the bottom. Due to the higher field concentration on the top part of the waveguide, the top-scattered field is expected to be even stronger for the modes propagating in the full-sized waveguide, where the higher-order modes are prominent.

A large number of higher-order modes compensates for their lower power compared to the fundamental mode; hence their effect is considerable in real-world propagation. Moreover, it is worth recalling that the actual device is orders of magnitude larger than the simulated one ($w_c = 3\,\mu\text{m}$), hence the number of higher-order propagating modes, as well as the optical scattering intensity, will be considerably larger.

3.3.4 Polarization

The last numerical modeling activity dealt with the effect of light polarization in the model. Polarization was horizontal (along the y axis) by default for all the simulations above. However, the effect of exciting vertically-polarized modes in small rectangular waveguides such as the one modeled here is worth investigating. Similarly to the steps above to find higher-order modes, the orthogonally polarized mode was obtained by changing the number of modes requested by the solver to 2 modes. This way, the second-order mode (with the second-closest effective refractive index) is found.

First, a mode distribution change was observed when exciting the z-polarized fundamental mode.

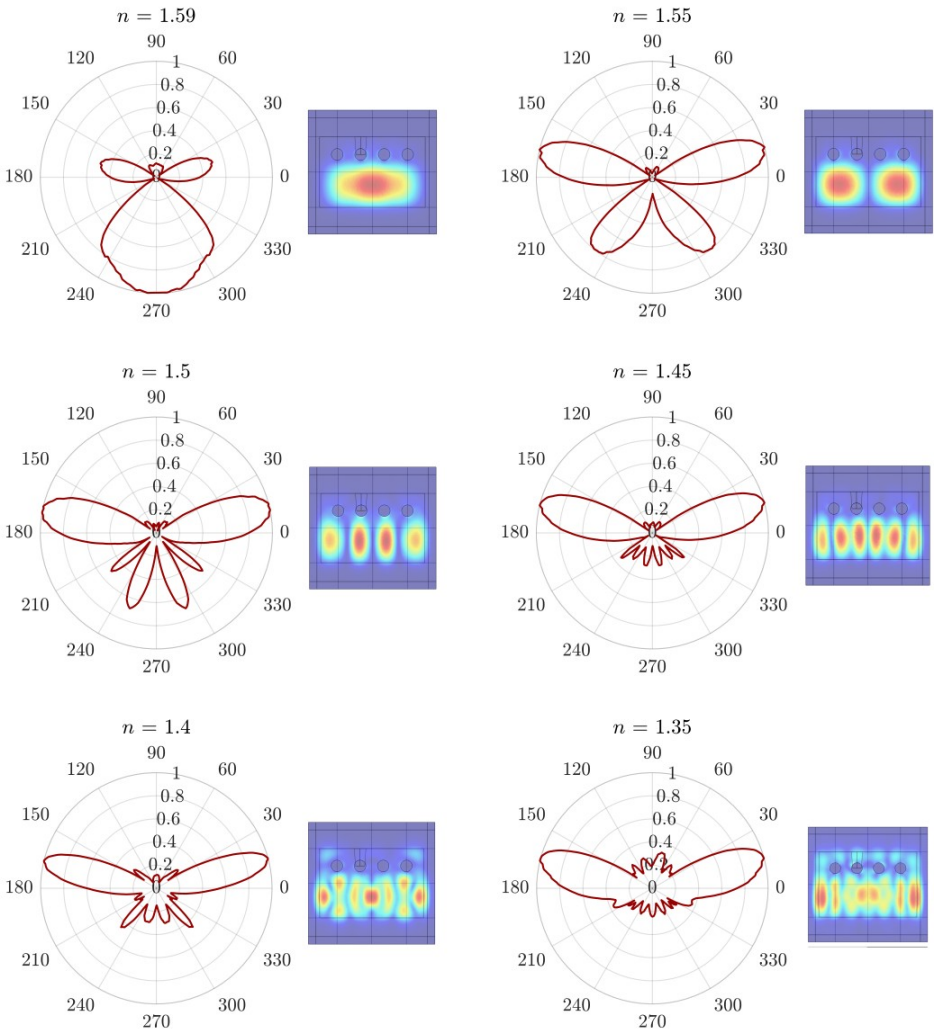

Figure 3.10: Polar plots of the normalized electric field outside the waveguide, on the yz plane intersecting the hole in half, shown with the respective excited modes on the side. The preferential directions of the scattered field change considerably with the effective refractive index.

Figures 3.11a and 3.11b show the cross-section at the end of the waveguide and axial field distribution for a core width of $w_c = 2\,\mu\text{m}$, together with arrows showing the polarization direction. Some differences can be observed by comparing it with the orthogonally polarized mode of Figure 3.7e and 3.7f. First, a more significant portion of the light is confined on the surface of the metal electrodes for a similar mode distribution. Second, the field intensity attenuates faster along the waveguide than in the horizontally-polarized mode. These changes are to be expected, as in such small, asymmetric waveguides, orthogonal modes are asymmetric, too. However, these differences are expected to disappear as the waveguide increases in size.

Similarly to Figure 3.8, the effect of polarization was thus evaluated as a function of the simulation size. The results for transmittance and absorptance are shown in Figure 3.11c. Due to the higher

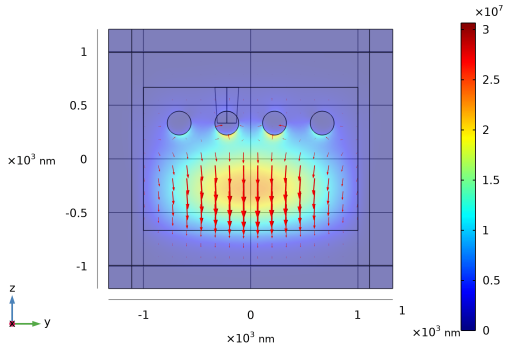

(a) Distribution and polarization at the end of the waveguide for $w_c = 2\,\mu\text{m}$ and the z-polarized fundamental mode.

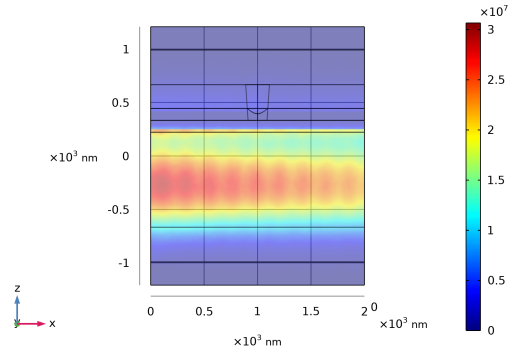

(b) Distribution along the propagation axis of the waveguide for $w_c = 2\,\mu\text{m}$ and the z-polarized fundamental mode.

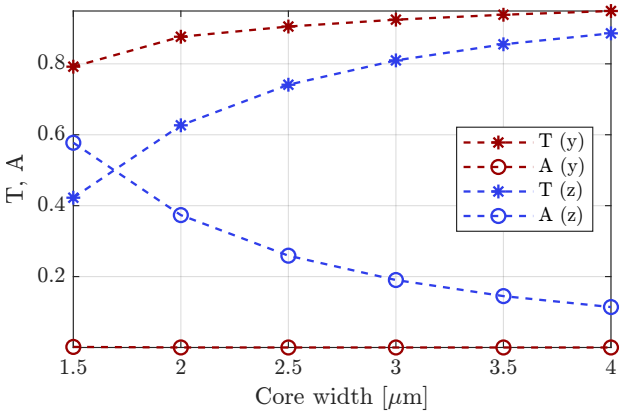

(c) Comparison of the transmittance and absorptance for different input polarizations with variable core width w_c.

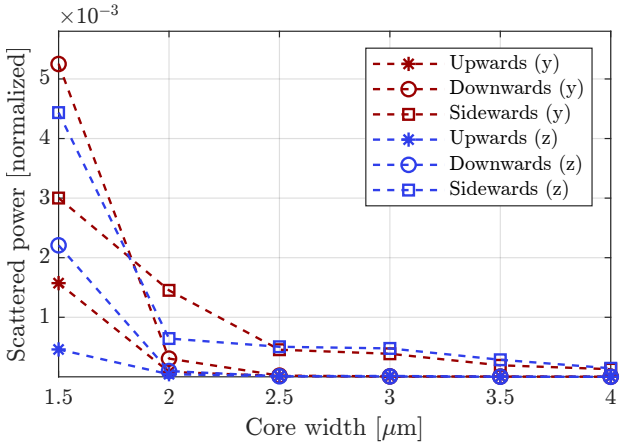

(d) Comparison of the upward and downward scattered power flow for different input polarizations with variable core width w_c.

Figure 3.11: Analysis of the polarization effects on the modeling in *ewfd*.

field concentration by the metallic surface, the absorptance is higher for the vertically-polarized mode. The difference between the two is initially high, with a ratio between the y-polarized mode and the z-polarized mode of 1.9 in terms of transmittance. However, as the core size increases, the difference between the two modes narrows, and the ratio is already 1.07 when the core width is 4 µm. The ratio is thus predicted to approach 1 for very large waveguides, and for the actual device, no significant difference is expected between the two polarizations.

Figure 3.11d shows that the scattered power is greater for the previously-analyzed horizontal polarization for both upward and downward scattering. Conversely, sideward scattering is stronger for the vertically-polarized mode. This result is arguably explained by the different interactions as a function of the polarization direction, which enhances the scattering because of the larger wavevector component parallel to the scattering direction.

Name	Symbol	Value	Name	Symbol	Value
Core width	w_c	3 µm	Electrode position (y)	y_e	-4 µm
Core height	h_c	$w_c * 2/3$	Hole upper width	W_h	$4r_e$
Core length	l_c	3 µm	Hole lower width	w_h	$0.8r_e$
Environment width	w_e	$w_c + 3t_{\text{PML}}$	Hole height	h_h	$r_e/6$
Environment height	w_h	$h_c * 1.1 + t_{\text{PML}}$	Wavelength	λ_0	650 nm
Electrode radius	r_e	$w_c/18$	Frequency	f_0	$c_{\text{const}}/\lambda_0$
Electrode position (x)	x_e	5 µm	Input power	P_N	1 W
Effective ref. index	n_{eff}	1.35:1.6	Thickness of the PML	t_{PML}	$\lambda_0/3$

Table 3.1: Parameters defined in the global definitions for the numerical model.

3.4 Protocol

A protocol describing the main steps to develop the simulation model is given below to conclude this chapter. Given the large number of simulation files and geometries tested in the project, the protocol will only cover one (specifically, the 3D model for comparing the different modes). Nevertheless, the other models follow naturally in most cases, and their generation does not vary significantly from the following procedure.

1. Model setup.
   (a) Select the model wizard and choose a 3D model.
   (b) Select the Electromagnetic Waves, Frequency Domain physics.
   (c) In the study setup, add a Boundary Mode Analysis step.
2. Global definitions.
   (a) Define all the geometrical and optical parameters, as reported in Table 3.1.
3. Geometry
   (a) Create a work plane (*wp1*) and insert it in the yz-plane.
   (b) In *wp1*, define a rectangle with the core dimensions and one with the environment dimensions. Define also a circle *c1* with the electrode dimensions and position.
   (c) Create an array pointing to *c1*, set the array type to linear, the displacement to $w_c * 9/2$, and the size to 4, to create the four electrodes.
   (d) Create an extrusion pointing to *wp1* and set the distance to l_c.
   (e) Create a cone with the dimensions of the hole (w_h, W_h, h_h), and set its coordinates to $(l_c/2, -w_c/9, h_c/2 - h_h)$.
   (f) Define another work plane (*wp2*) in the yz-plane, and set the x-coordinate to $l_c/2$. Inside, define a rectangle with dimensions $w_c + 80$ nm and $h_c + 80$ nm.

4. Perfectly-matched layer

   (a) In the rectangle for the environment, define a layer on all four sides with thickness t_{PML}.

   (b) In the *artificial domains*, create a *perfectly matched layer*, set its type to cartesian, and assign it to the domains 1-6.

5. Materials

   (a) Select the water model (real and imaginary part) from Hale and Querry 1973 in the material library. Assign it to domains 1-6, 12-15, and 20.

   (b) Select the tungsten model (real and imaginary part) from Ordal et al. 1988 in the material library. Assign it to domains 8-11, 16, 18-19, and 21-23.

   (c) Select the PC model (real part) from Sultanova et al. 2009 in the material library. Manually add the information about the imaginary part from the model that can be exported from [75], and assign the material to domains 7 and 17.

6. Physics

   (a) Make sure that PEC boundaries are assigned to all outer boundaries of the geometry.

   (b) Define a port (*port1*), set its type to numeric, turn on the excitation at the port, and set the input power to P_N. Assign the port to boundaries 14, 21, 25, 30, 35 and 40.

   (c) Define a port (*port2*), set its type to numeric, turn off the excitation at the port, and assign the port to boundaries 107 and 109-113.

7. Mesh

   (a) Create a mesh and set the sequence type to *user-defined*.

   (b) Set the default mesh size to *general physics* calibration, with *finer* elements.

   (c) Create a free-tetrahedra sub-mesh and set the calibration to *physics-controlled* and the element size to coarser. Set the minimum vacuum wavelength to λ_0.

   (d) Create a swept sub-mesh and assign it to all the PML domains. Set the number of both vertical and horizontal elements to 10.

8. Study

   (a) Assign the *boundary mode analysis 1* to *port1* and frequency f_0. Set the desired number of modes to 1 for a horizontally-polarized mode, and set the mode to search around n_{eff}.

   (b) Create another *boundary mode analysis* step and repeat the previous step for *port2*.

   (c) Select the *frequency domain* step and set the frequency to f_0.

   (d) Create a default solver configuration and compute the solution.

9. Results

   (a) Under desired values, create a global evaluation group. Insert the expressions *ewfd.Rtotal*, *ewfd.Ttotal* and *ewfd.Atotal* to compute the reflectance, transmittance, and absorptance.

(b) Create three surface integration groups, and assign them to boundaries 19, 16, and 15+50, respectively. Insert the expression *ewfd.nPoav* under all three groups to compute the scattering power for the up, bottom, and side boundaries.

(c) Create a 3D plot group. Create two slice plots, each with the expression *ewfd.normE*, to display the electric field magnitude along selected planes. Set the planes to yz and xz and the number of slices to the desired value.

(d) Create a 1D plot group. Create a line graph with the expression *ewfd.normE*. Assign it to lines 90-92 and 148 and plot the result against the arc length.

(e) Export the plot data to a table and save the results to a file. To display the scattering on a polar plot, prepare a script to convert the arc length for each of the four lines into the correct angle.

Chapter 4

Fabrication

This chapter contains the main work of the project, illustrating all the fabrication steps carried on to produce the optoelectrical interface. Five preforms with different designs and material properties were used throughout the project. Each section in the chapter illustrates the fabrication process for a different preform and is divided into four subsections with the following structure:

1. Preform design. This step includes the CAD design and the features of the preform.
2. Waveguide drawing. This subsection contains information about the thermal drawing process for the preform, including time-resolved graphs of the parameters and resulting waveguide cross-sections.
3. Micromachining. In this step, the process for the fabrication of holes to create optical scattering points and to expose the metal electrodes is described.
4. Connectorization. This step includes information on the electrical integration, connector adapters, and device encapsulation.

To conclude the chapter, the final section gives a brief overview of the five preforms and reports a thorough protocol for the fabrication of the final design.

4.1 The PMMA waveguide

Preform design

The starting point for the drawing of the waveguides was a standard PMMA cylindrical preform of 25 mm in diameter. The preform was first annealed at 50 °C for three days in a vacuum dryer (Goldbrunn 450) and subsequently machined into a prism with a rectangular cross-section of dimensions $90 \times 17 \times 13.5$ mm and an adapter for the clamping system of the drawing tower on one end.

Waveguide drawing

The waveguide was drawn in the Neurolab of DTU Electro, using a drawing tower for POWs and POFs. The drawing tower featured a furnace with a single temperature setpoint, a laser measuring

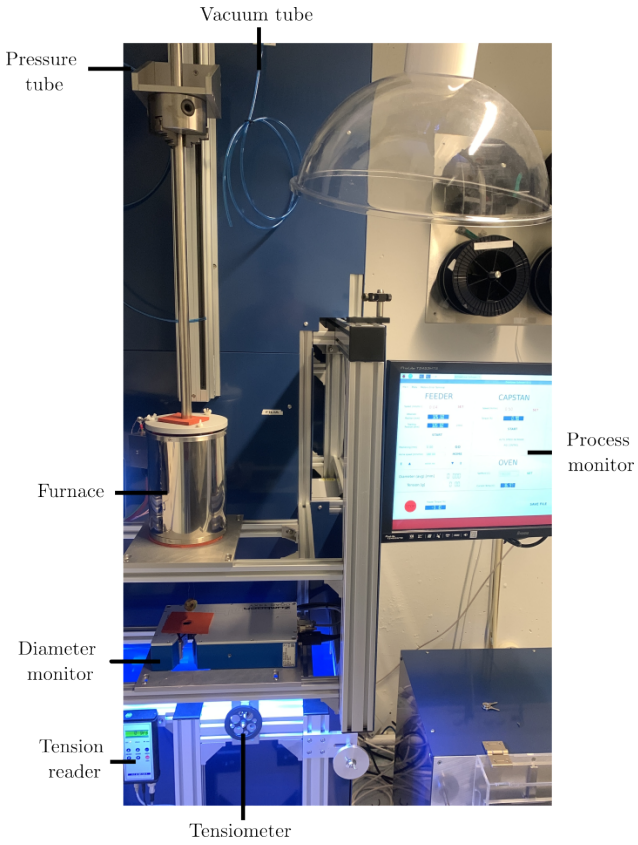

Figure 4.1: Picture of the drawing tower used in the project.

head to detect the fiber cross-section diameter, a tensiometer, and a capstan. Figure 4.1 shows a photograph of the drawing tower.

A hole was first drilled near one of the short sides to suspend a weight with an iron thread. This is done to both increase the stress on the preform while drawing, thereby easing the drawing of the fiber at lower temperatures, and to have a visual aid to assess when the preform begins to drop under heat. The initial cross-section target was $250 \times 200\,\mu m$, corresponding to a reduction of 68 times from the preform cross-section, as per the mass-conservation law of Equation (2.10). Moreover, since the waveguide is made of a single material and has no microstructure, the pressure parameter, which would otherwise be crucial to ensure the fiber is drawn correctly, is unimportant.

Initially, the preform was clamped to the tower, and the furnace was heated to 120 °C (60 °C below the target draw temperature) and left stabilizing for about one hour to homogeneously heat the preform, as PMMA has low thermal conductivity. Subsequently, the temperature was increased by 5-10 °C until the preform slowly began to drop. The final temperature was set at 205 °C. A plot of the setpoint temperature and the readout from the internal sensor is shown in Figure 4.2a. The readout shows a little temperature overshoot; hence the increase of the temperature in short steps, especially at higher temperatures.

At that point, the iron weight and the first section of PMMA with decreasing cross-section were removed. Once the fiber became small enough, it was spun around a tension meter made of three rollers, pulled by the capstan, and spooled. The feed and the pull speed were adjusted throughout the drawing, ranging between $v_f = 0.2 - 0.6\,mm/min$ and $v_p = 0.24 - 2.3\,m/min$, respectively, to

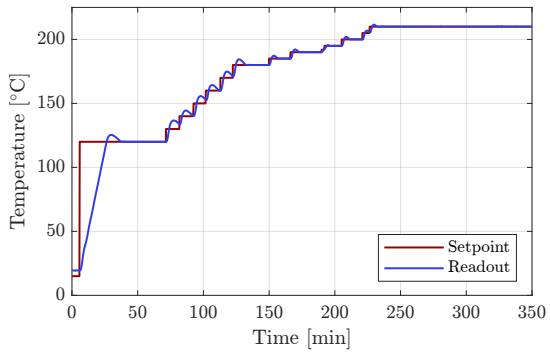

(a) Setpoint and real-time readout temperature in the tower furnace. The readout temperature features some degree of overshoot.

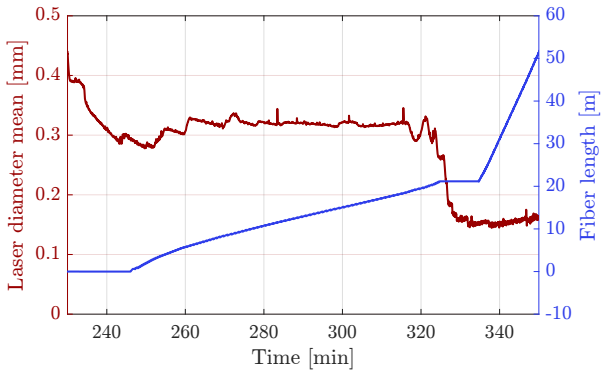

(b) Fiber diameter measured by the laser sensor, and total drawn fiber length. The diameter length is overestimated by about a factor of 1.2.

Figure 4.2: Data collected during the fiber drawing.

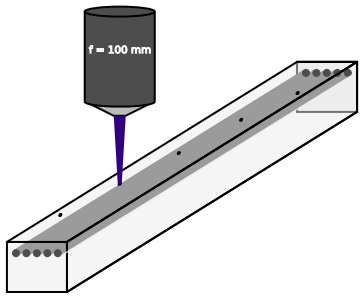

Figure 4.3: Illustration of the laser micromachining technique on the PC-Sn waveguide.

obtain the desired waveguide cross-section.

The rectangular cross-section of the drawn waveguide is incompatible with the sensor, which is made for detecting circular cross-sections. Thus, the reported diameter (Figure 4.2b) generally overestimates the actual length, which was read using a digital caliper or by examining the cross-section under an optical microscope for more accurate results.

Micromachining

The laser micromachining tool (LMT) is a microSTRUCT Vario from 3D-Micromac AG [79]. The purpose of this tool is to produce microstructures using high-power, ultrashort, focused laser pulses. The machine includes two different lasers: a 50 W picosecond laser (FUEGO) from Time Bandwidth Products and a 100 W nanosecond laser from IPG Photonics. While the latter was currently inactive in the machine, the former was the laser needed for the machining. FUEGO features three different operational wavelengths: 1064 nm, a second harmonic generation (SHG)-induced 532 nm mode and a third harmonic generation (THG)-induced 355 nm mode. The pulse duration is short of 12 ps, with a variable repetition rate from 200 kHz – 8 MHz. The pulse energy is up to 200 µJ, and the average output power is 30-37 W after the last laser module. The principle of micromachining is sketched in Figure 4.3, where the laser is focused on one of the channels to machine a hole.

To micromachine polymers such as PMMA and PC, THG mode was found to be the most suitable,

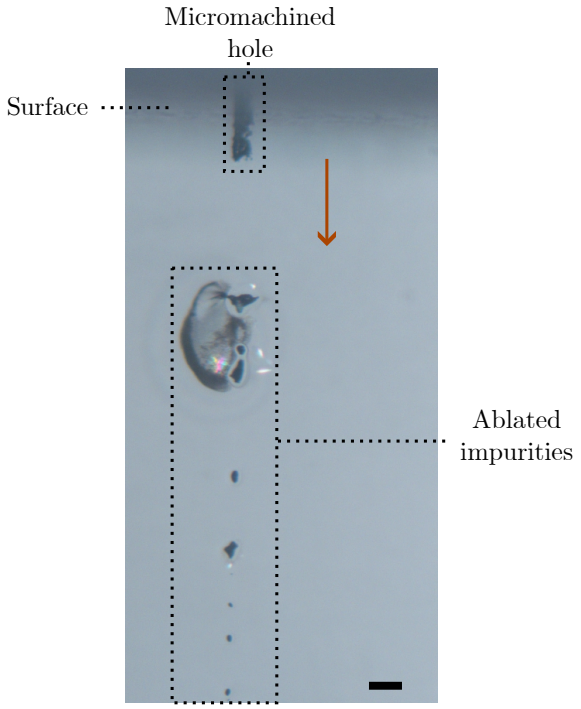

Figure 4.4: Machining of PMMA with the 1064 nm laser mode. The orange arrow indicates the beam direction. Scalebar = 100 µm.

as the absorption is the highest among the three wavelengths. As a matter of fact, when using the 1064 nm laser, the impurities in the polymer absorb most of the radiation, creating a series of irregular debris zones along the beam direction, as highlighted in Figure 4.4.

To run a job in the micromachining tool, three files must be prepared:

- A job file listing all the instructions for the job, such as the activation of the chuck vacuum beneath the blue tape frame, the xy alignment on the sample, the z focusing alignment, the activation of the suction, and the number of repetitions for the laser machining.
- A parameter file, loaded inside the job, contains the laser configuration parameters, such as the laser power, the laser on/off delay time, the laser wavelength, the objective, and the data input file. This file is most responsible for the quality of the machining.
- A data input file, in DXF or other formats, with the geometry to be machined onto the sample. This file was created in Clewin, a software typically used for the design of lithography masks, which can, however, also export into DXF and thus create a map of lines to be machined.

During the optimization of the machining, the main parameters that have been edited are briefly described as follows.

- **Laser power**. The laser power is clearly of primary importance in defining the etch rate. However, especially when using SHG or THG crystals, one should expect a highly nonlinear etch rate growth with power because of the increasing harmonic conversion efficiency associated with higher laser input power. The laser power is tuned by an acousto-optic modulator (AOM) and a thin-film polarizer (TFP). Usually, power is changed only by tuning the latter, which is

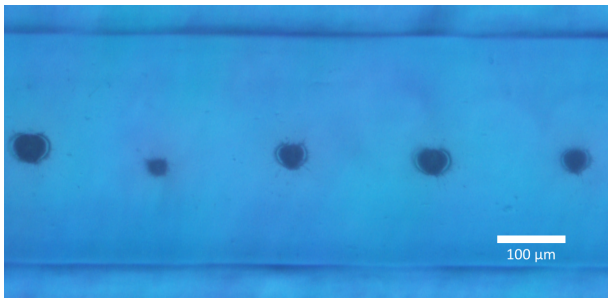

(a) Top view of the holes (laser-on times are 200, 300, 250, 225 and 265 µs, respectively.

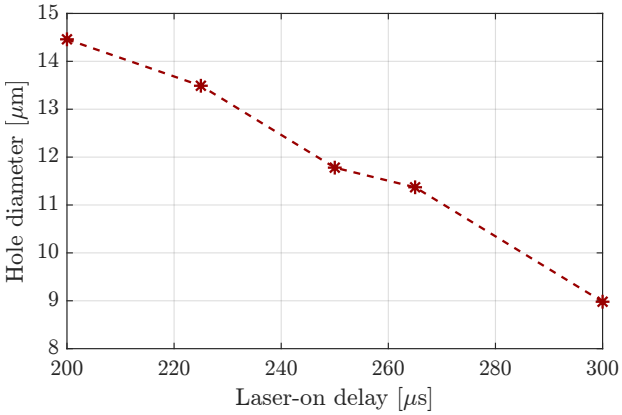

(b) Hole diameter against laser on delay time

Figure 4.5: Testing of the laser-on (and -off) delay in the LMT.

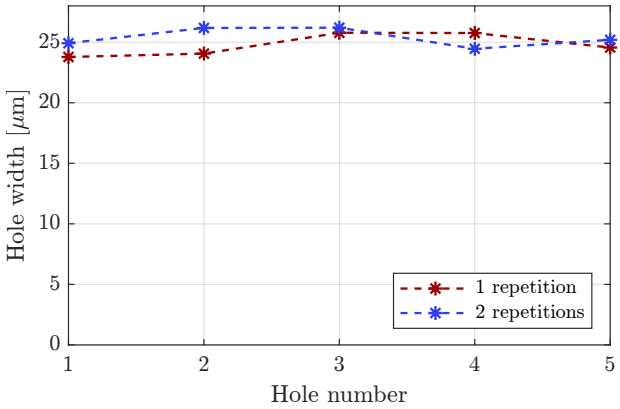

(a) Measurements of the hole diameters. The error is 3.8% and 3.1% for 1 and 2 repetitions, respectively.

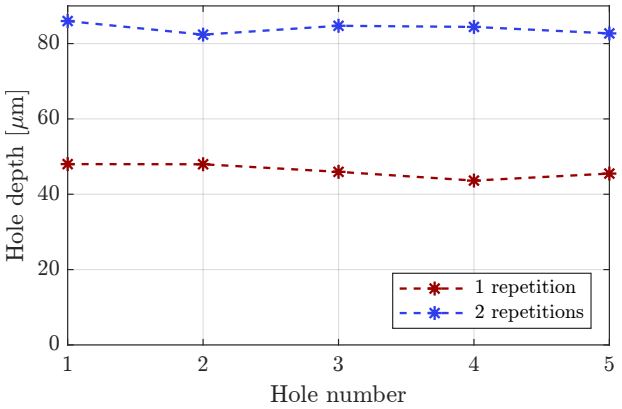

(b) Measurements of the hole depths. The error is 4.0% and 1.8% for 1 and 2 repetitions, respectively.

Figure 4.6: Results from the hole reproducibility test.

kept on a range between 10 and 80% of the maximum. Nevertheless, as explained in detail below, it is usually more convenient to change the number of repetitions rather than the laser power, which was kept at 50% for most of the tested processes.

- **Jump delay**. The laser jump delay regulates when the laser resumes writing after moving the mark vector. If it is too short, running-in oscillations will be visible. A long jump delay does not negatively impact the machining quality, but it increases the scanning time. Given the very small machined area, the jump delay was set to a relatively large value (3000 µs).

- **Laser-on/off delay**. The laser on and off delay values are particularly important for short patterns such as these holes. The laser on (off) delay regulates the delay between the start (end) of the laser machining after it has been moved in place at the starting point of a new symbol. If the laser on delay is too long, the pattern will be incomplete, as the start of the symbol will not be marked. On the other hand, if it is too short, burn-in effects at the start of the symbol will result. A test on PMMA of different laser delays is summarized in Figure 4.5. Since the quality of the holes did not seem to improve after 225 µs, the laser-on delay was kept

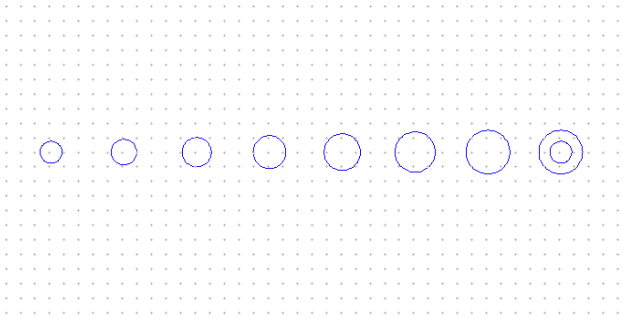

(a) Mask used for the repetition test. The grid measures 20 µm.

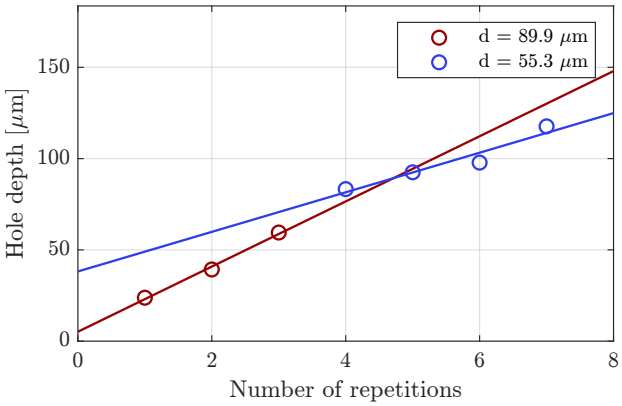

(b) Regression of the hole depths as a function of the number of repetitions.

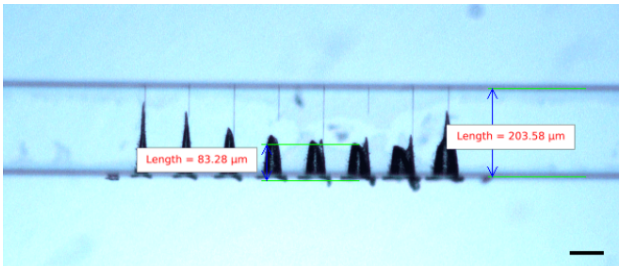

(c) Side view with $N = 4$. Scalebar = 100 µm.

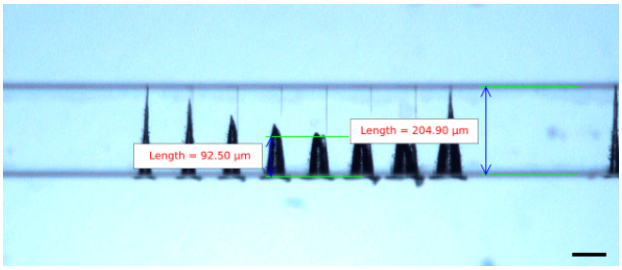

(d) Side view with $N = 5$. Scalebar = 100 µm.

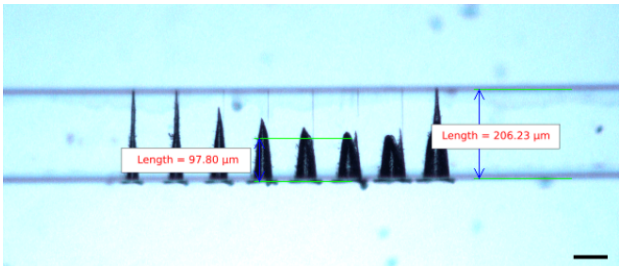

(e) Side view with $N = 6$. Scalebar = 100 µm.

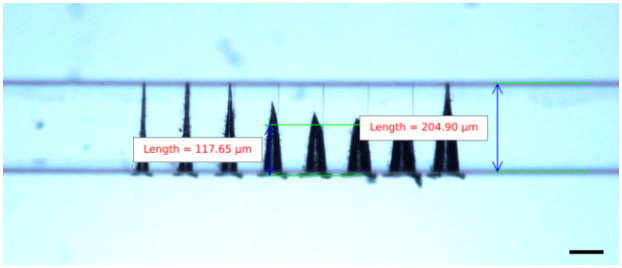

(f) Side view with $N = 7$. Scalebar = 100 µm.

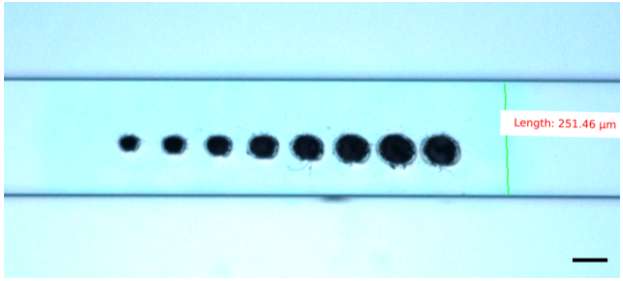

(g) Top view of the set of eight holes. Scalebar = 100 µm.

Figure 4.7: Summary of the results from testing the number of repetitions on PMMA with the LMT (mask diameter from 30 µm to 60 µm) on the PMMA fiber obtained with four repetitions at 80% TFP laser power.

at that value. Similarly, the laser-off delay was set to 275 µs.

- **Number of repetitions** N. This parameter adjusts the number of machining repetitions performed by the laser. The etching rate is not expected to be linear with the number of

repetitions because, assuming that the laser is focused on the surface of the sample, as the repetitions increase, the radiant flux at larger depths will decrease, thereby etching less material per repetition. Nevertheless, a test revealed that a linear fit could roughly approximate the etching rate. To find the most suitable hole width and depth, a series of eight holes of different sizes (from 30 to 60 µm, with steps of 5 µm) were machined with 1 to 8 repetitions (Figure 4.7a). While the number of repetitions does not change the width of the hole, it increases the depth. Incidentally, note that the final hole has an additional, smaller circle inside. Figure 4.7b summarizes the tests on two holes with different diameters and the linear fits on the data. It is worth underlining that the hole depth is also a function of the hole width, as a smaller diameter corresponds to a higher etch rate. This can also be easily seen in Figures 4.7c-4.7f, as the hole depth decreases with increasing hole size. Finally, the last hole (corresponding to the two concentric circles in the mask) shows a possible way to taper the hole profile and increase the depth in two steps. Incidentally, an increase in the number of repetitions has been shown to increase the consistency in the micromachined hole dimensions. Figure 4.6 shows the results from a reproducibility test, where two sets of five holes with identical process parameters were machined (TFP power at 80%). The first set was machined with $N = 1$, and the second with $N = 2$. As one can notice, both the hole diameter and depth are consistent across the holes. The normalized error for the hole diameter at $N = 1$ and $N = 2$ was 3.79% and 3.05%, respectively. For the hole depth, the improvement was more significant: the error with two repetitions went from 3.98% to 1.78%. This confirms the good reproducibility of the micromachine holes, which can be created to match the desired profile reliably.

- **Alignment process**. While a single hole has rotational symmetry and needs no alignment (one can shift the center to the desired position above the sample), arrays of holes or more complicated mask geometries usually require at least another degree of alignment. This can be easily done with a two-point alignment, where the first point defines the shift (i.e., the center of the mask on the sample), and the second point defines the rotation. When machining arrays of holes on an electrode, for example, it is sufficient to align the second point to the end of the electrode. More advanced alignment methods exist but were not needed in this project. Furthermore, there is a separate step for vertical alignment to focus the beam at the desired level; by focusing the camera lens on the surface of the waveguide, for example, a consistent beam focus can be achieved. Two cameras are available for aligning: a zoom and a wide camera. While the wide camera is beneficial for larger designs, it is critical to align the micromachined hole exactly above the desired position. Hence, the zoom camera, from which the features on the surface and inside the waveguide can clearly be distinguished, was used for both the single-point and vertical alignment.

Many other parameters can be adjusted in a parameter file, such as the jump and mark speeds, which also contribute to the overall accuracy and process time. However, they were found to be of minor importance and have not been altered further when creating additional configurations for new jobs.

Connectorization

The connectorization for the first PMMA waveguide was planned with tungsten (W) wires. The available wires had a diameter of 10 µm, 20 µm and 50 µm. The insertion of the wires inside the machined holes was attempted using an optical microscope by taping the ends of the piece of fiber and slowly bringing a piece of the wire closer to the hole with a pair of tweezers. While generally, a larger diameter increases the stiffness of the wire and makes the alignment with the waveguide easier, it also implies the need for micromachining larger holes. The holes with 40 µm were found to be too shallow to reliably slide the microwires in, while the thicker wire of 50 µm could be centered in the larger set of holes (diameter of about 75 µm).

Nevertheless, a reproducible method to reliably bend the tungsten wires to insert the tip in the hole and align the rest over the length of the waveguide could not be found. Attempts were made with flexure stages, but the curly wires could not be straightened properly and fixed to the stage to do so.

4.2 The PC-Sn waveguide

To counter the difficulties met when connectorizing with the tungsten wires, the electrodes were included in the preform preparation step. In general, this allows dramatically improved control over the fabrication process, which does not rely on manual alignment. A centimeter-scale preform is machined to have the desired geometrical proportions for the cross-section size and the holes, and metal wires are slid into the holes. The preform is then heated into the furnace of the draw tower above the glass transition temperature T_g and the melting temperature T_m of its constituent materials and drawn into the fiber [80]. The metal and the waveguide materials were chosen to have compatible melting and drawing temperatures, respectively. As a consequence, 1.5 mm-thin tin (Sb) wires (99.99+% purity) and PC were chosen. The main advantages of tin are the low melting point (231.93 C) and the flexibility at room temperature: tin is stiff enough to slide into the holes but flexible enough not to be brittle.

Preform design

As the previous PMMA preform, the preform consisted of a PC cylinder of 100 mm in length and 26 mm in diameter. Given the higher sensitivity of the heat drawing process due to the tin, the preform was further designed to be 15 mm × 12 mm in cross-section, with five holes of 1.6 mm, to ease the machining process and have some tolerance. The CAD design model for the preform is shown in Figure 4.8a.

Similarly to the first one, this preform was annealed at 50 °C for three days, and subsequently, the tin wires were slid into the five holes.

Waveguide drawing

The drawing of the PC-Sn was not successful. After one hour to stabilize the temperature at 150 °C, the temperature was increased gradually by 10 °C every 10 minutes until 200 °C, and subsequently

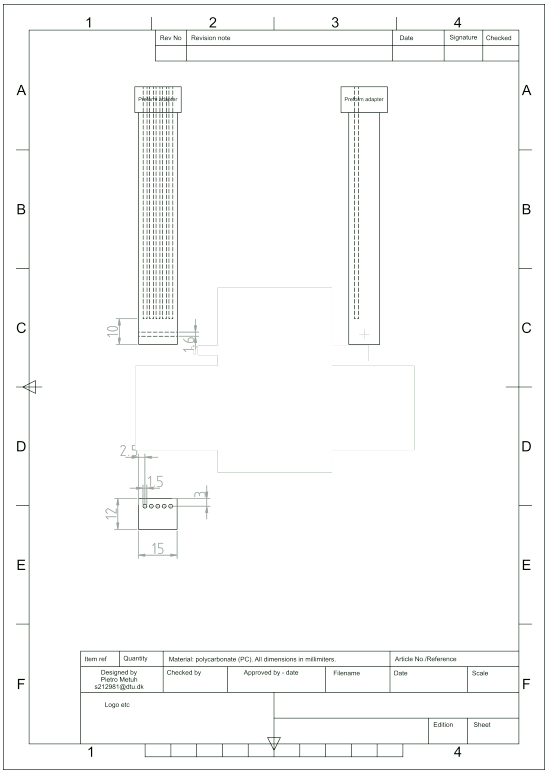

(a) CAD model for the preform, designed in QCAD.

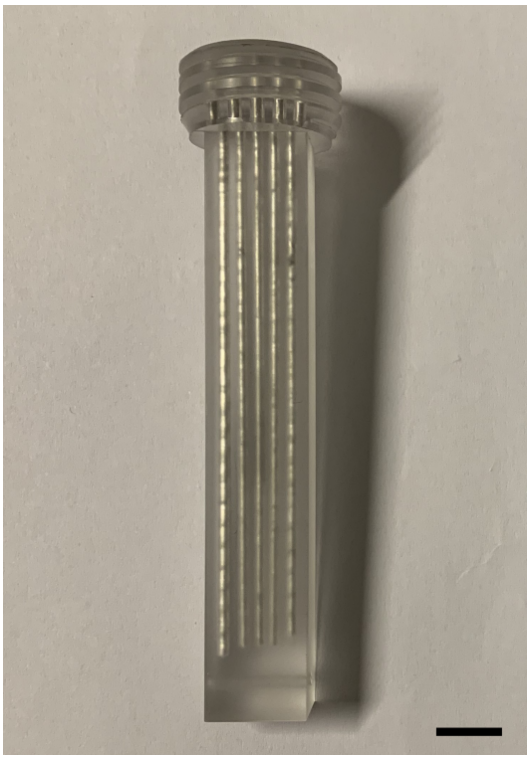

(b) Preform before the thermal drawing. Scalebar = 1 cm.

Figure 4.8: Preparation of the PC-Sn preform.

by 5 °C every 7 minutes. At 220 °C, the preform began to slide downwards, but the tin was still solid. Even though the melting temperature should be about 232 °C, the setpoint of the furnace was considered to be higher than the actual temperature inside the preform. The final temperature to try and compensate for this was 260 °C. However, at this temperature, the PC was arguably too hot and melted the preform much faster, intermittently closing down the machined holes and leaving only spare traces of tin along the waveguide. Due to the heat capacity of tin, the drawing could not be accomplished with these parameters, despite the attempts to compensate by adjusting the tension on the drawn waveguide. Figure 4.9 shows some pictures of the drawing attempt. While the fibers drawn in [78] used a tin-bismuth alloy, which is characterized by a lower melting temperature, pure tin wires were found to retain their shape for too long during the drawing.

4.3 The PC-In waveguide

Since it appeared that the cause of unsuccess for the PC-Sn preform was the high drawing temperature, a metal with a yet lower melting point was considered. Indium (In) has a melting point of 156.6 °C, and successful drawings of PC-In fibers have been demonstrated before [80]. On the other hand, indium is more prone to oxidation.

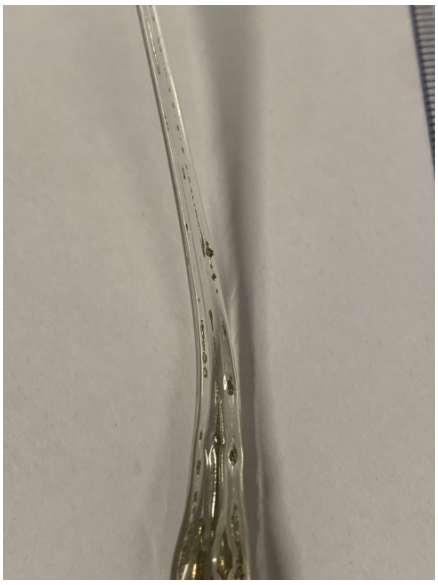

(a) Initial point of melting for the tin, when the temperature was increased. The holes are partially collapsed, and the tin has formed clumps.

(b) Residual of the preform after drawing. The distorted shape shows that the draw temperature was too high for the polycarbonate.

Figure 4.9: Details from the drawing of the PC-Sn waveguide.

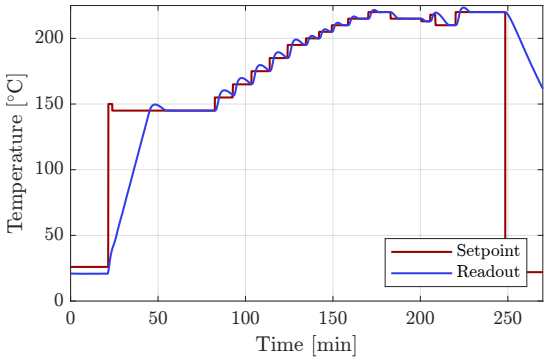

(a) Setpoint and real-time readout temperature in the tower furnace.

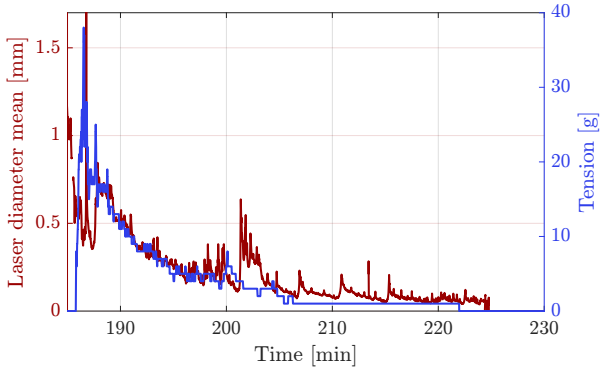

(b) Fiber diameter measured by the laser sensor and tension measured by the gauge. The diameter length is overestimated by about a factor of 1.2.

Figure 4.10: Data collected during the fiber drawing of the PC-In preform.

Preform design

The preform was machined identically to the PC-Sn waveguide; hence the design is the same as shown in Figure 4.8a. The preform was annealed for several days at 50 °C, and the wires were inserted. Due to the small difference between the indium wires and the 1.6 mm holes and the malleability of the indium, it was rather difficult to fit wires as a whole, and they had to be cut in smaller pieces and pushed down the hole with a screwdriver of similar diameter.

(a) Initial drop and remainder of the preform. Scalebar = 1 cm.

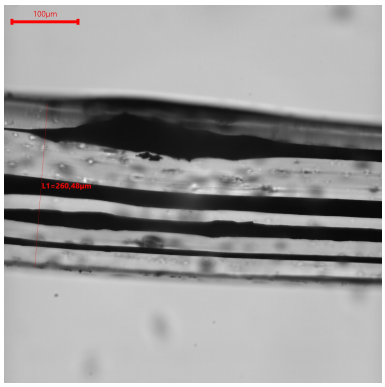

(b) Detail of an indium lump in one of the channels.

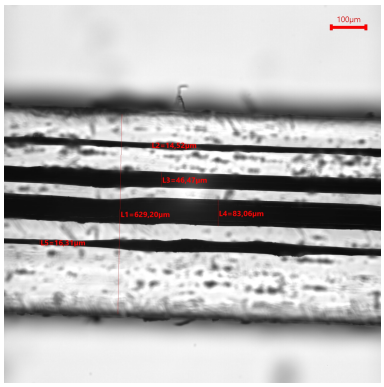

(c) Comparison of channel dimensions in a waveguide section.

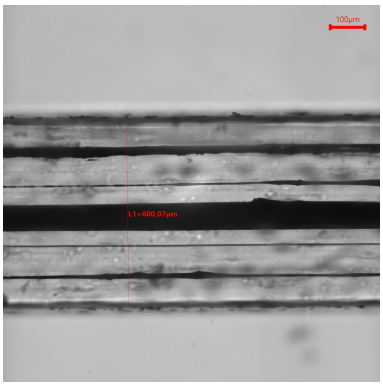

(d) A piece of waveguide with five electrodes.

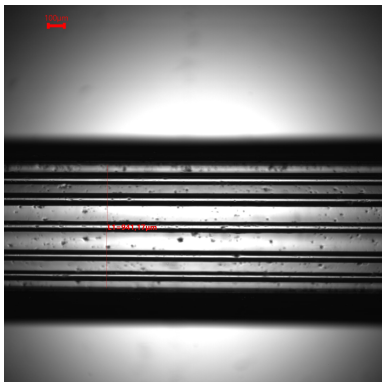

(e) A piece of fiber with empty channels.

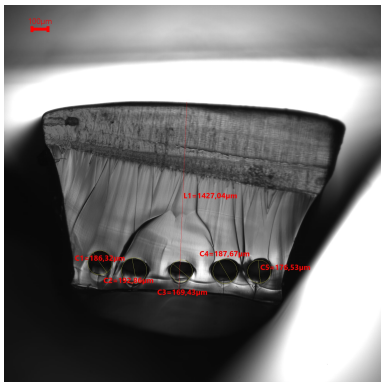

(f) Deformed cross-section of the preform by the necking region.

Figure 4.11: Drawing of the PC-In waveguide.

Waveguide drawing

The preform was heated up to 145 °C (about 10 °C less than the melting point of indium) and subsequently increased by 10 °C every 10 minutes until 200 °C, after which the temperature was increased by 5 °C every 7 minutes. Like the PC-Sn preform, the PC began dropping at 220 °C. However, the low melting point of indium deformed the beginning of the fiber, and due to the higher heat capacity of indium, some lumps deformed the bottom part of the preform, as shown in Figure 4.11a. This made the initial part of the drawing asymmetric, thus deforming the rectangular geometry of the cross-section and creating areas without any metal, as shown in Figure 4.11f, where the waveguide was cleaved with the cut-and-bend technique (a small cut is made with a razor blade on the opposite side of the holes, and the fiber is then bent until cleaved) to reduce the stress on the hole region. Here, one can also notice that the asymmetry made the cross section trapezoidal instead of rectangular.

During the drawing, the diameter of the waveguide quickly decreased to less than 100 µm, despite the attempts to stabilize the diameter by increasing the feeder speed, decreasing the pull speed, or changing the furnace temperature (Figure 4.10a) after 180 min. The tension also decreased until it

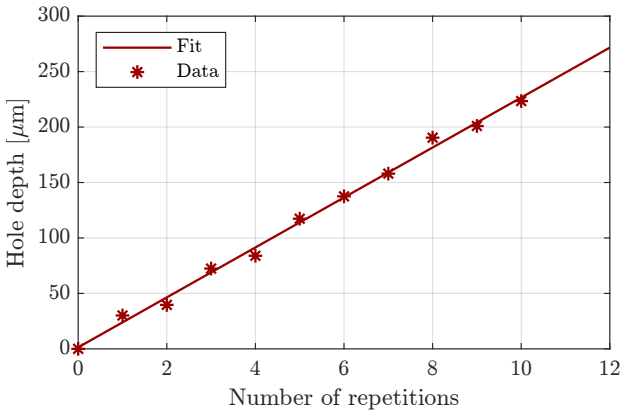

(a) Hole depth against the number of repetitions. The blue line shows a linear regression from the data.

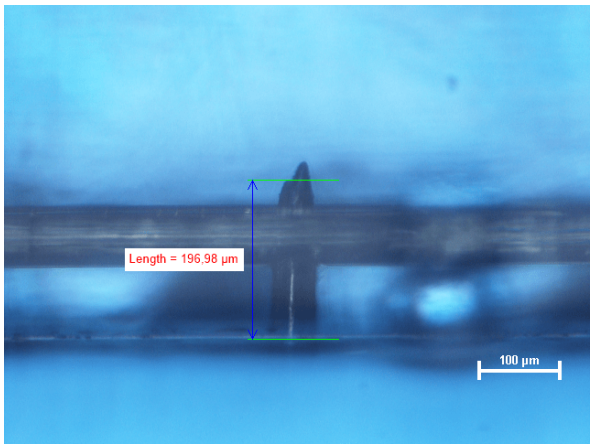

(b) A hole perforating an indium electrode, obtained with $N = 8$.

Figure 4.12: Testing the number of repetitions on PC with the LMT.

dropped to 0 g on the gauge, as shown in Figure 4.10b. Finally, the fiber section shrank so much that it caused a break, and the drawing had to be stopped. The remainder of the preform can be seen on the right in Figure 4.10.

The drawing did not stabilize enough to spool the fiber. However, parts of it could be saved and inspected. The distribution of indium across the fiber pieces was rather irregular, with some sections showing lumps of metal (Figure 4.11b), some with one or more collapsed channels (Figure 4.11c), and in general with a very large difference in diameter between channels (Fig. 4.11c, 4.11d). After the necking region, a section of the fiber even had empty channels, which, however, did not collapse (Figure 4.11e).

Micromachining

A new repetition test was performed to estimate the etch rate for PC. Figure 4.12a shows the interpolation of data obtained from reading the hole depth with a number of repetitions between 0 and 10. Even for PC, the depth is approximately linear with the number of repetitions. The attempts of machining through an indium electrode (Figure 4.12b) suggest that the hole length is unaffected by it, and it perforates through it, arguably due to its malleability.

4.4 The first PC-W waveguide

The polycarbonate-tungsten (PC-W) waveguide is fabricated by drawing a machined preform and introducing tungsten wires through the holes, whose size is naturally reduced due to the thermal drawing. The advantages of such an approach are the ease of connectorization (the tungsten wires can be connected directly to a printed circuit board (PCB)), higher drawing stability (no metal acting as a heat sink), and the use of a widespread metal in biological implants. On the other hand, while the fitting of the wires is easier than the initial approach through the holes with the PMMA waveguide, it is still prone to irregularities and requires a high hole tolerance.

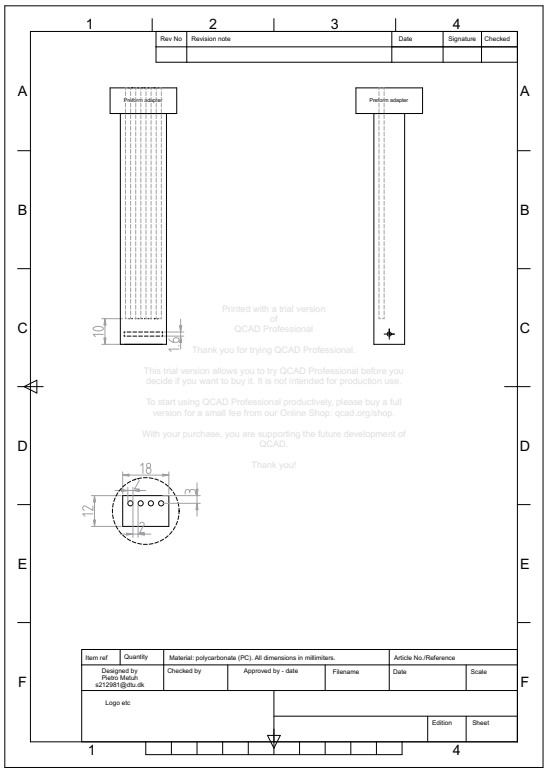

(a) CAD model for the preform, designed in QCAD.

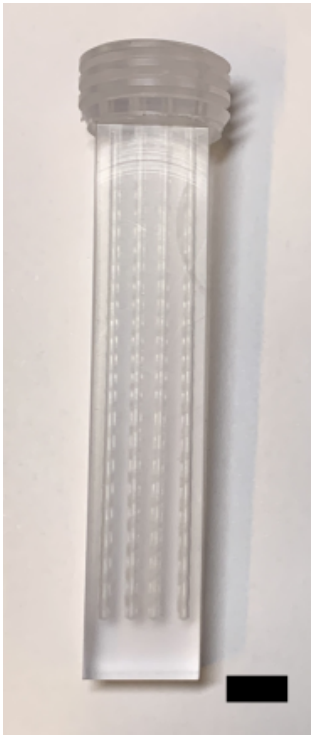

(b) Preform before the thermal drawing. The scale bar represents 1 cm.

Figure 4.13: PC-W preform.

Preform design

To increase the robustness of the waveguide during drawing, the number of holes was decreased to four, and the spacing between the holes was increased, as given in the CAD model design of Figure 4.13a. Figure 4.13b shows the preform before thermal drawing. Again, the annealing time was of 72 hours.

Preform drawing

The preferred tungsten wires have a diameter of 50 µm, hence the target hole size was of about 75-100 µm (shrinking of the preform by a factor 27 or 20, respectively) to have an adequate tolerance. While a smaller tolerance might be sufficient to fit the wires, the fiber cleaving causes a slight deformation of the holes, thus making them oval and decreasing their size.

The preform was drawn between 210 °C and 215 °C, as shown in Figure 4.14b. From examining the cross-section at the beginning of the drawing, the outermost electrode holes were found to be smaller than the innermost ones (Figure 4.14e), arguably due to additional stress forces when far from the center of the waveguide. To counter this, pressurized gas was activated from the top of the drawing tower and increased slowly. However, the pressure gas, which had not been previously tested in this draw tower, was found to be working improperly above 3.5 mbar, and by the end of the drawing, the size of the smaller holes was not found to change significantly. Figure 4.14f compares the ratio between side and central hole diameters in selected samples collected during the fiber drawing. Comparing the ratio with the pressure readout shown below, no correlation is found. Consequently,

(a) Initial drop and residual preform after the thermal drawing, with a ruler for scale.

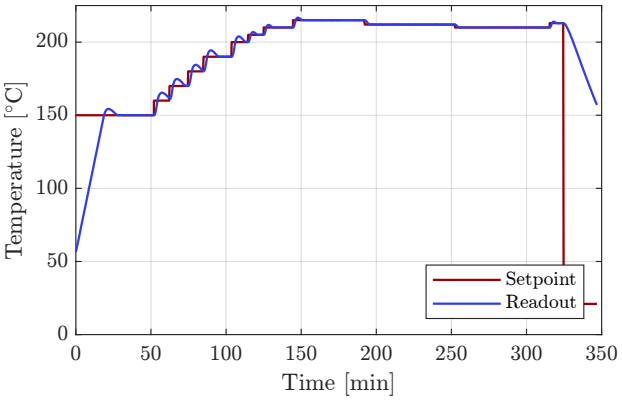

(b) Temperature setpoint and readout during the drawing.

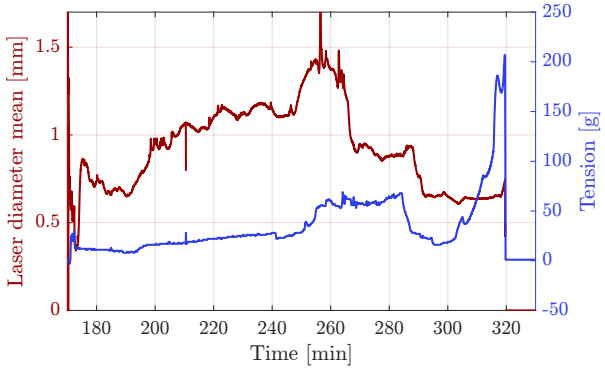

(c) Laser diameter (blue) and readout tension (orange).

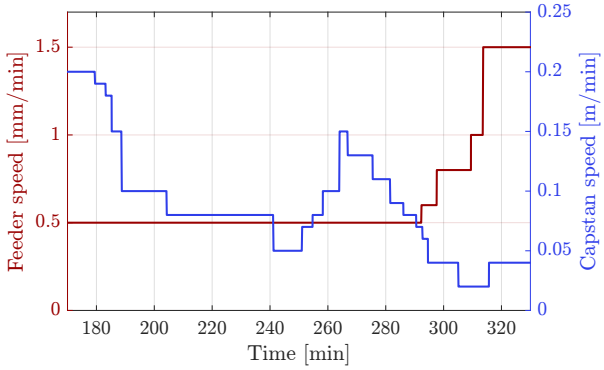

(d) Capstan and feeder speeds during the drawing.

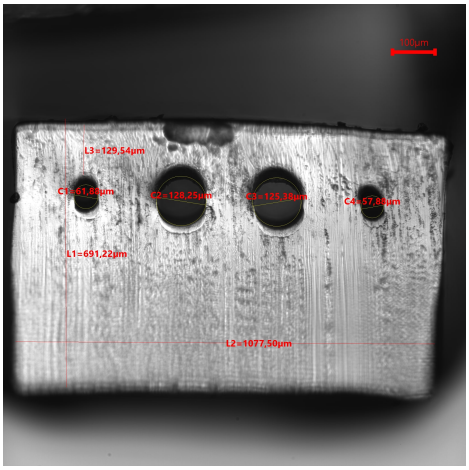

(e) Cross section of a piece of fiber of 1077 µm in width.

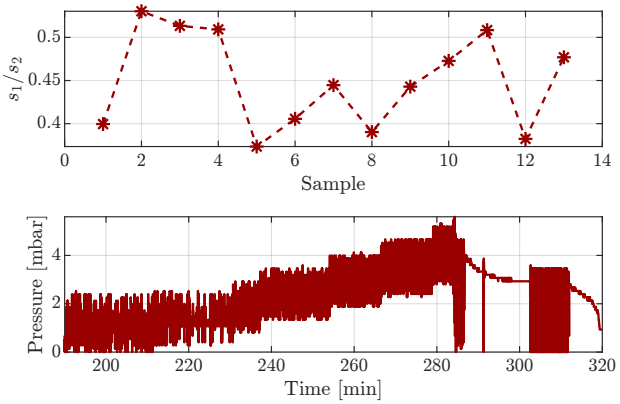

(f) Ratio between the outermost and innermost diameters d_2/d_1 (above) and gas pressure during the drawing (below).

Figure 4.14: Drawing of the first PC-W preform.

the fiber was drawn at a slower pull speed to increase the overall cross section (and thus the hole) size, as shown in Figure 4.14d. The temperature was also decreased to try and increase the tension, which usually helps maintain the features of a microstructured fiber.

The fiber could not be brought back to millimeter size, even when increasing the feed speed

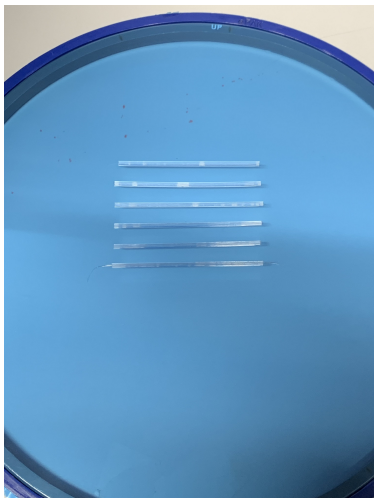

(a) 5 cm-long samples on the blue tape after the micromachining.

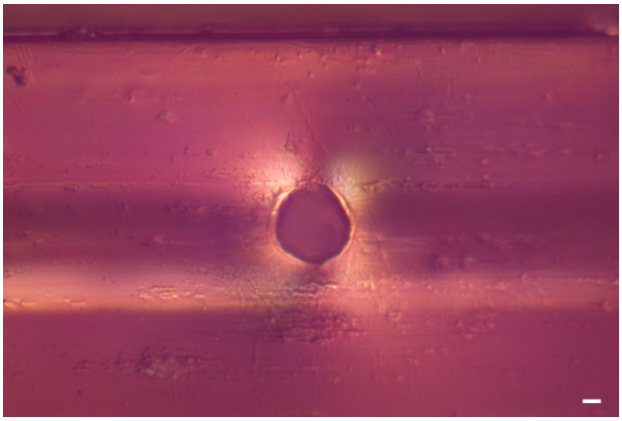

(b) Top view of a machined channel from an optical microscope with an analyzer. Scalebar = 10 µm.

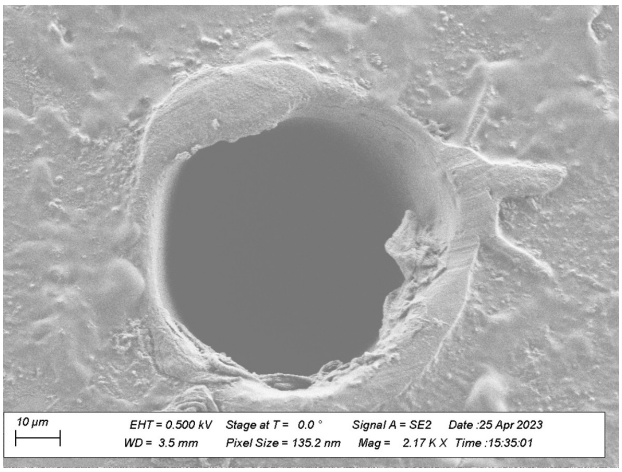

(c) Magnified view of a machined channel, from an SEM.

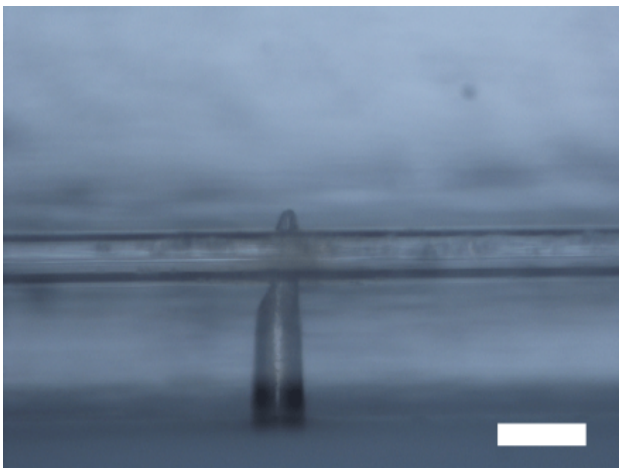

(d) Side view of a machined channel, from an optical microscope. Scalebar = 100 µm.

Figure 4.15: PC-W micromachining process.

or decreasing the pull speed (Figure 4.14c). Finally, towards the end of the preform drawing, the preform dropped. This was due to the preform adapter reaching the hot zone of the furnace and, since it is made of metal, starting behaving as a heat sink and increasing the temperature of the PC by the adapter, which made it melt and drop.

Micromachining

Six pieces of 5 cm of waveguide were cut and micromachined (Figure 4.15a). For each piece, the four electrodes were micromachined with a hole to expose the electrode. While from the repetition test of Figure 4.12a, six repetitions would have been enough to reach 130 µm for a hole of 55 µm in diameter, seven repetitions were used to increase the hole uniformity at a deeper distance from the surface (the expected hole depth was thus 158 µm). Each electrode is spaced 1 cm along the length of the fiber. Figure 4.15b shows one of the holes with a reflection optical microscope and a polarization analyzer, a device that filters light polarized along all but one direction. Analyzers can be used

to image scattering more easily because scattered light has rotated its polarization, thus providing better contrast. In this case, the bright spots close to the hole can be more easily seen. Figure 4.15c shows an image of the hole taken with an scanning electron microscope (SEM), which helps distinguish the surface features of the polycarbonate. While polymers such as PC are transparent in the visible spectral range, they are opaque to electron microscopy; hence the topography of the waveguide after machining can be better observed. Finally, Figure 4.15d reports the side view of the hole, which slightly extends after the channel.

Connectorization

Due to the partial collapse of the side holes during drawing, the fitting of the tungsten wires could be performed on only two of the six samples. Wires with diameters of 20 µm and 40 µm were found to be too thin to be inserted without bending, hence 50 µm wires were used for both the central and the side holes. The wires were cut to be a few centimeters longer than the 5 cm devices and manually inserted with a tweezer under an optical microscope. To connectorize the device, an adapter was 3D-printed. The adapter features two pieces; the bottom part with five slots for connectors (four dedicated to the tungsten wires inside the channels and one for electrical ground as a reference point to measure voltage), a circular hole for the optical ferrule, and a rectangular one for the end of the waveguide; the top part works as a lid to keep the wires and the 5-pin electrical connector in place. The adapter measures $11 \times 7 \times 6$ mm. After the manual insertion of each wire on the respective slot, the connector and the lid were placed, and the adapter was closed with a drop of superglue. The microwires were then trimmed on the other end, and the interface was stabilized by placing some superglue by the rectangular hole of the adapter.

Only two devices from the first PC-W preform could be connectorized because the side holes were too small for all the other samples. Nevertheless, the size of these samples was relatively large, making the implant stiffer than predicted. Therefore, some changes in the design were made to compensate for these issues.

4.5 The second PC-W waveguide

A second PC-W preform (Figure 4.16b) was made with increased size in the side holes (2.4 mm instead of 2 mm). All the other geometrical parameters were left intact and matched the CAD design of Figure 4.13a. The purpose of this design change was to try and compensate for the partial hole collapse experienced during the drawing of the first PC-W preform. By making the side holes larger, their shrinking is expected to be at least partially compensated. This helps both the connectorization with the tungsten microwires (which was possible only with very few pieces of the fiber drawn from the first preform) and the reduction of the cross-section size.

Preform drawing

During the first part of the drawing, the cross-section of the drawn fiber was inspected. Since the side holes still looked smaller than the central ones, the gas pressure was activated and ramped up, as shown in Figure 4.17b. However, the pressure was raised too much, and at 20 mbar, there was a

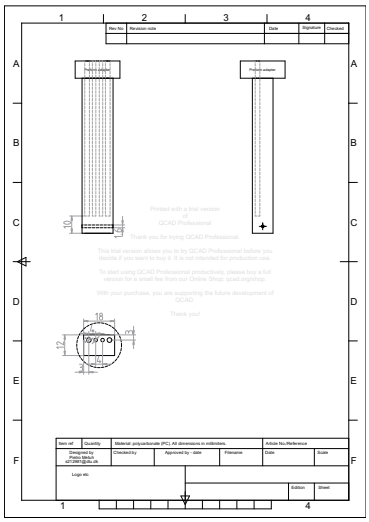

(a) CAD design of the second PC-W preform, with enlarged side holes.

(b) The second PC-W preform, with enlarged side holes. Scalebar = 1 cm.

(c) Initial drop and residual preform after the thermal drawing. Scalebar = 1 cm.

Figure 4.16: Design and photographs of the second PC-W preform.

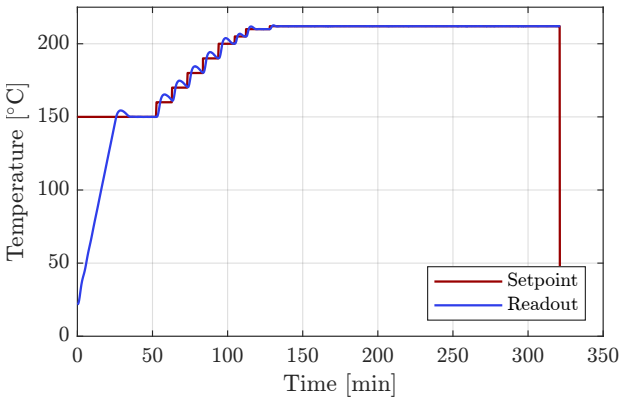

(a) Temperature setpoint and readout. The maximum temperature was 212 °C.

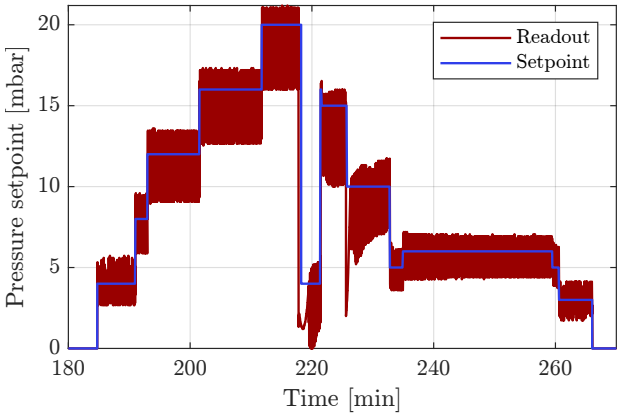

(b) Setpoint and readout pressure during the drawing. Drops of readout pressure correspond to rupture.

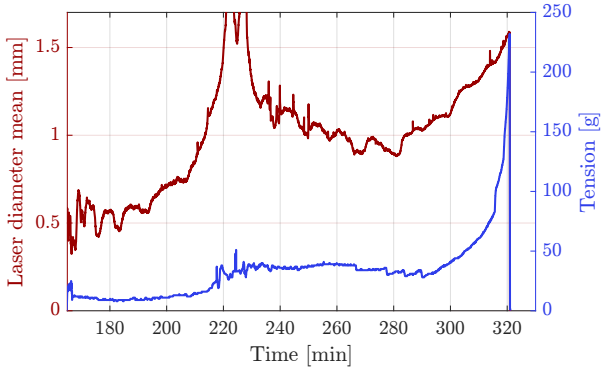

(c) Laser diameter (blue) and readout tension (orange).

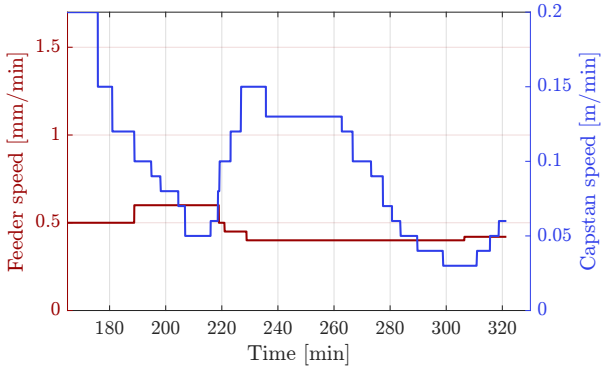

(d) Feeder and capstan speed.

Figure 4.17: Data from the drawing of the second PC-W preform.

rupture in the preform, as can be seen from the sudden drop in the readout temperature at about 218 min. The pressure setpoint was decreased at first and turned up again to 15 mbar. However,

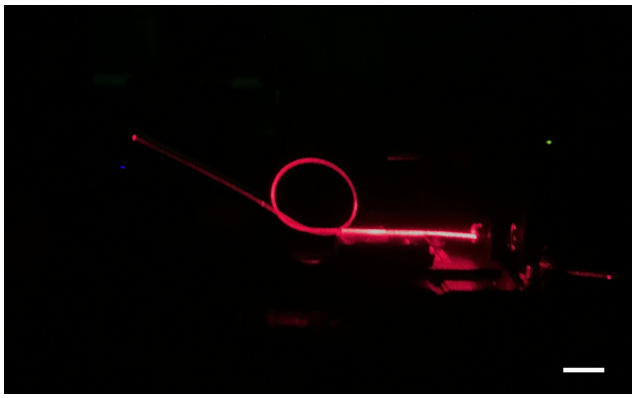

Figure 4.18: Knotted piece of the flexible PC waveguide, with red laser light coupled from one input. The bending diameter is 1.7 cm. Scalebar = 1 cm.

after a second rupture (see the drop at 225 min), the pressure was decreased even further, and the final part of the fiber was drawn with no pressure at all.

After the two ruptures, a long piece of damaged fiber was spooled. In this fiber, the central holes were overly enlarged and exploded towards the top of the waveguide, making the waveguide useless for any device. The final piece of the drawn waveguide, however, recovered the rectangular cross-section and featured enlarged side holes almost the same size as the central ones. This final piece of fiber was used to build the final devices.

Not only had the fiber from the second preform holes with similar sizes, but for a given hole size, the fiber was smaller, which meant that the devices could be scaled down in size while enabling easier connectorization with 50 µm microwires. The cross-section measured 941 µm in width and 563 µm in height, corresponding to a reduction factor of 19.1. The smaller cross-section of the waveguide, combined with the material properties of PC, enables a great degree of flexibility, which is qualitatively demonstrated in Figure 4.18, where the waveguide is purposefully knotted and coupled with red light to show both the flexible substrate and the capability of guiding light despite the bending losses.

Micromachining

After considerations regarding the ease of surgery on the spinal cord, the length of the device was decreased to 1 cm, with half a centimeter at one end to account for the fiber piece outside the animal and attached to the connector. A batch of three 1 cm devices was micromachined with one hole per channel, with the same laser power as the previous batch (AOM power at 100%, TFP power at 50%, design hole diameter of 55 µm), but with nine repetitions instead of eight, for an expected hole depth of about 175 µm. Each hole was spatially separated by 2 mm. Although the planned surgery was meant to use 1 cm, additional, longer devices were also micromachined, with lengths of 2, 3, and 4 cm (producing six devices in total).

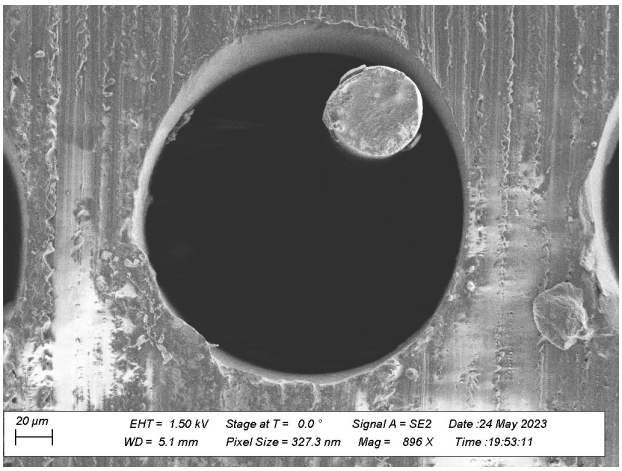

(a) Cross-section view of a single channel with a tungsten electrode.

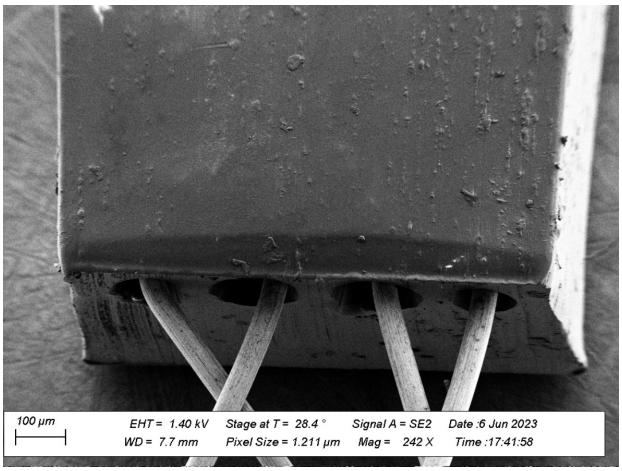

(b) Tilted view of one end of the interface, showing four protruding microwires.

Figure 4.19: End of a connectorized interface with the four tungsten wires coming out from the channels.

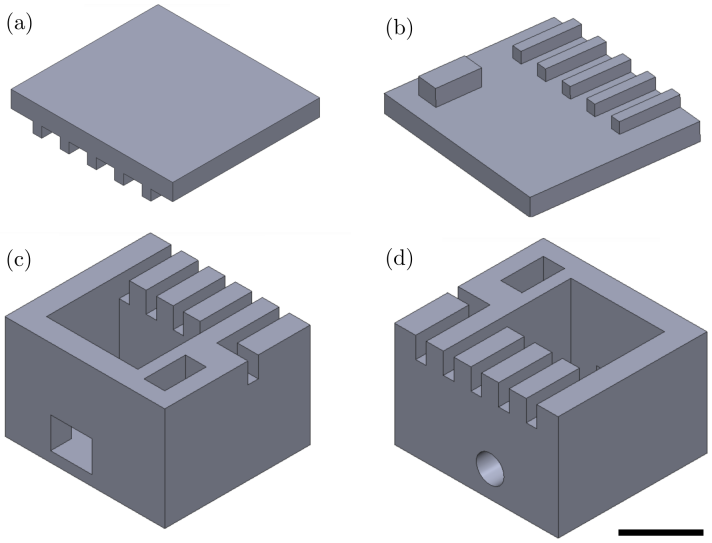

Figure 4.20: 3D-printed adapter design, showing (a) top of the lid; (b) bottom of the lid; (c) waveguide side of the main case; (d) ferrule and connector side of the main case. Scalebar = 5 mm.

Connectorization

Thanks to the larger holes, the connectorization was much easier and faster than the samples from the first PC-W preform. The 50 µm tungsten wires were fitted in the same way as before and could now be reliably inserted and removed even on the side holes of each device. Figure 4.19 reports some pictures of the I/O of the interface, with the four 50 µm tungsten wires coming out from the channels.

After the insertion of the tungsten wires (their length was variable but, in general, much greater than the device length), a new batch of polymer connectors was 3D-printed with a slightly larger hole for the optical ferrule; the CAD design of the adapter is shown in Figure 4.20. To improve the quality of the connectorization, the bottom part of the adapter was attached to a metal slab

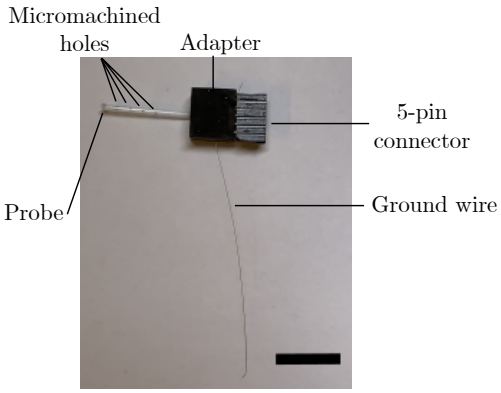

(a) Photograph of the fully-completed connectorized device, with a 3D-printed adapter, a 5-pin female connector, and a tungsten electrode for electrical ground. Scalebar represents 1 cm.

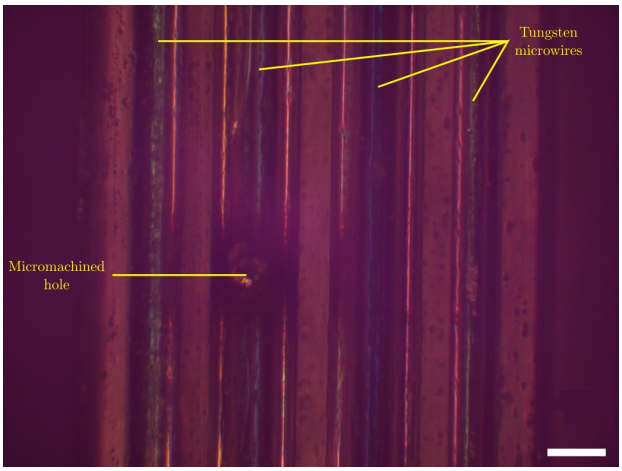

(b) Top view of a hole in one of the connectorized devices. The tungsten wires can be distinguished in each channel thanks to the analyzer filter and the bottom illumination of the optical microscope. Scalebar = 100 µm.

Figure 4.21: Final connectorized device.

with double-sided adhesive tape. The waveguide was inserted through the rectangular slit and also taped in place. Then, each wire was manually drawn through the respective guide with a tweezer and taped to the metal slab to avoid moving them while fitting the other microwires. This approach is much less prone to errors and allows taping every moving part of the device before placing the 5-pin connector and the lid of the adapter in place, finally closing with super glue. After fixing the adapter to the waveguide with more glue, the tape was removed, and the trimmed microwires at the end of the waveguide were insulated with another drop of glue. It is worth remarking that depending on the super glue, the capillary forces might be strong enough for the glue to penetrate inside the channels and clog the micromachined holes, preventing electrical contact with the environment and rendering them ineffective, so additional care must be put during the sealing step.

The coupling quality of the connectorized devices was optically tested by using a simple setup consisting of a red laser coupled to free space and then to a patch cable with an optical ferrule output (Thorlabs FG105LCA), which was plugged into the device. Figure 4.22a shows a macroscopic photograph of the connected device, from which the scattering points can already be noticed. Figures 4.22b and 4.22c further show the scattering properties of the connectorized device obtained through a digital optical microscope. Given the power of the red laser, the scattered light might seem rather weak; however, when using an light-emitting diode (LED) with comparable power to that used in optogenetics, as shown in the following chapter, the scattered power is high enough for neural stimulation.

4.6 Material comparison and protocol

This final section gives a brief overview of the preforms and the fabrication steps followed in the project. Table 4.1 illustrates the materials, thermal drawing parameters, micromachined features,

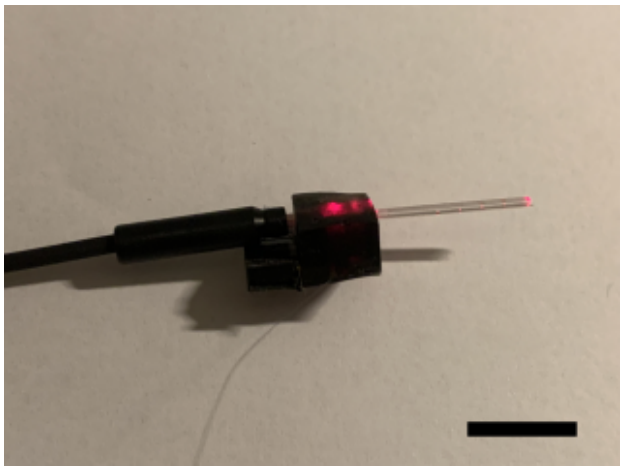

(a) The device, connected to an optical ferrule. Scalebar = 1 cm.

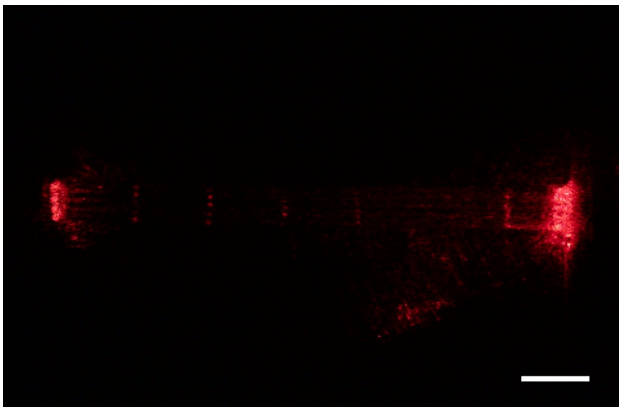

(b) Top view of a 1 cm connectorized device, showing the four scattering points and the light coupling at the end of the guide. Scalebar = 1 mm.

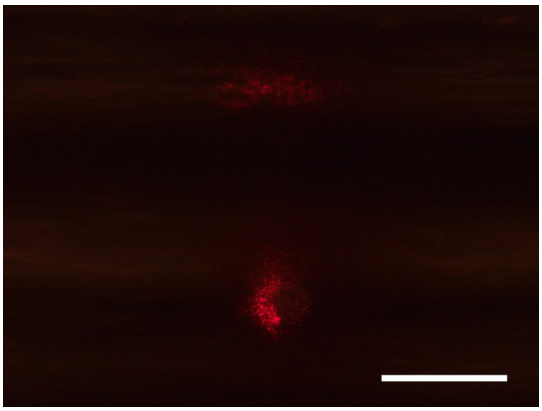

(c) Optical picture of a hole partially scattering red light propagating inside the waveguide, as seen from the top of the device. Scalebar = 100 µm.

Figure 4.22: 1 cm interface connected to an optical ferrule, showing scattering over the four micromachined holes.

and connectorization techniques. Some information, such as the hole profile for the PC-Sn and PC-In waveguides, was not reported, as the quality of the drawn waveguide was not high enough to continue with the fabrication process.

Given the successful fabrication of the full interface from the second tungsten preform, a protocol illustrating the entire fabrication procedure for a PC and tungsten-based optrode interface is detailed as follows:

1. Preform preparation
   (a) Obtain a PC cylindrical preform, at least 10 cm in length and 2.5 cm in diameter.
   (b) Machine the preform according to the CAD design of Figure 4.16a, shaping the preform adapter for the drawing tower, the rectangular cross-section of the preform. Machine the holes for the four channels with drills of 2 and 2.7 mm in diameter. Machine also a small hole at the bottom of the preform to fit through a thin wire to hold a weight for the thermal drawing.

Design	Preform	T_g [°C]	Pressure [mbar]	Feeder speed [mm/min]	Capstan speed [m/min]	Hole diameter [µm]	Hole depth [µm]	Connectorization
PMMA-W Surface channels	PMMA	205	0	0.2-0.6	0.24-2.3	25-80	80-120	–
PC-Sn	PC Sb wires	230-260	0	0.1-1	0.08-0.40	–	–	–
PC-In	PC In wires	210-220	0	0.04-1	0.05-0.50	–	–	No electrical connection
PC-W	PC	210-215	0-3.5	0.5-1.5	0.02-0.2	52	160	50 µm tungsten wires (2 channels)
PC-W Enlarged side holes	PC	212	0-20	0.4-0.6	0.03-0.20	52	175	50 µm tungsten wires (4 channels)

Table 4.1: Summary of the parameters and features of the fabricated waveguides.

(c) Anneal the preform for at least 72 hours in the temperature-controlled vacuum oven at 50 °C.

2. Thermal drawing

(a) Take the preform out of the vacuum oven.

(b) (Optional step) Fit a metal wire through the hole at the bottom of the preform and affix a light metal weight at the end to visualize the preform dropping rate.

(c) Start the thermal draw tower software and mount the preform on the metal adapter.

(d) Lower the preform inside the oven and cover the top with insulating foam.

(e) Turn on the furnace and set the temperature to 150 °C. Let the temperature stabilize for one hour.

(f) Increase the temperature in the furnace by 10 °C every 10 minutes, until 200 °C are reached. Increase then by 4 °C every 7 minutes, reaching 212 °C, and eventually by 2 °C every 5 minutes, until the bottom of the preform slowly begins to drop.

(g) Wait for the preform to drop about 1 m, then slice the fiber with a metal cutter. Turn on the waveguide diameter monitor.

(h) (Critical step) Activate the feeder and capstan drives and set them to 0.4 mm/min and 0.1 m/min. Take the new end of the dropping preform and very slowly pass it through the wheels and the tensiometer, and feed it to the capstan drive, ensuring that little stress is applied to the preform.

(i) Wait for the diameter of the waveguide to stabilize. If the diameter stabilizes below 600 µm, increase the capstan speed progressively until the desired diameter is obtained. If the diameter stabilizes above 900 µm, increase the feeder speed until the desired diameter is obtained. Moreover, check that a tension of at least 40 g is read at the tensiometer. If the tension is smaller, decrease the temperature of the furnace by 2 °C until the tension rises.

(j) Cut a waveguide sample and inspect the dimensions and the cross sections with an optical microscope. If the side channels are partially collapsed, activate the pressure on the

drawing tower and set it to 10 mbar. Cut and inspect another sample after 15 minutes, and adjust the pressure accordingly.

(k) When the samples have stabilized to the desired dimensions, start spooling the waveguide.

(l) Towards the end of the preform, the fiber diameter usually increases; hence, possibly increase the feeder speed to maintain a stable diameter size.

(m) When the furnace hot plane has reached the preform adapter, stop the feeder and the capstan drives, cut the remaining preform, and shut down the furnace. Raise the preform from the furnace, and wait for it to cool down before removing it.

(n) Inspect all the pieces of waveguide collected during the drawing, measure the dimensions with an optical microscope, and select a piece with stable features of at least 50 cm in length.

3. Micromachining

(a) Design a simple DXF file (in Clewin, QCAD, or similar software) with a single circle of 55 µm.

(b) Prepare the job and the parameter files, setting the wavelength to THG, the AOM power to 100%, the TFP power to 50%, the jump delay to 3000 µs, the laser-on delay to 225 µs, the laser-off delay to 275 µs, the number of repetitions to 9, a single-step xy alignment with the zoom camera and a vertical alignment with the zoom camera. Leave all the other parameters to their default values.

(c) With a freshly opened blade, cleave a series of 1.5 cm-long samples.

(d) Inspect the two ends of each sample and discard or cleave again any end with irregular dimensions in the channels.

(e) Turn the microSTRUCT Vario LMT system on, launch the software program and turn on the FUEGO picosecond laser. Wait 30 min for the laser power to stabilize.

(f) Place all the samples on a blue-tape sample holder, ensuring that the side closer to the four channels faces up. When in doubt, inspect the position of the channels under an optical microscope.

(g) Load the blue tape sample holder inside the LMT, placing a silicon wafer between the holder and the chuck to avoid damaging it with laser radiation.

(h) Test the quality of the hole by executing the job on a dummy sample and inspect both sides of the sample under the optical microscope to measure the size of the micromachined hole. Adjust the process parameters accordingly.

(i) For each channel, execute the job and manually align the laser onto the desired channel. Use the coordinate system of the aligner to calculate the position between holes and from the ends of the sample. Align vertically by focusing the camera on the upper surface of the fiber. Repeat this for each sample.

(j) Unload the samples, turn off the laser, and shut down the LMT as instructed by the user manual.

4. Connectorization

   (a) 3D-print the plastic connector adapters, following the CAD design shown in Figure 4.20.

   (b) Tape the sample on a vertical holder with adhesive tape, the cross-section facing up. Place the holder under a large enough optical microscope.

   (c) With a sharp pair of scissors, cut a series of 50 µm-diameter tungsten wires in pieces of about 4 cm.

   (d) With a very fine tweezer, take a microwire about 8 mm from one of the ends and insert it in a channel of the waveguide sample. Gently release the wire, and move it inside with the tweezer until it can be pulled from the other side of the waveguide. Repeat this for each of the four channels.

   (e) Remove the sample from the vertical holder and tape it onto a flat surface. Insert one waveguide end inside the connector until the position that the optical ferrule can reach when inserted, and tape the connector with double-sided adhesive tape.

   (f) (Critical step) Tape all the tungsten wires but one by the end opposite the adapter. With a tweezer, grasp the free wire and slide it through the respective guide on the adapter. Extend the microwire further and tape it in front of the adapter. Finally, tape the other end of the microwire back. Repeat for all the wires until all four wires are positioned along the right guides and taped on both sides. Ensure no wire is in contact with another wire inside the adapter to avoid short circuits.

   (g) Cut a 8 cm-long microwire, bend it at about 3 cm, and insert it on the fifth guide, reserved for the ground wire. Tape the ends of the microwire, too.

   (h) (Critical step) With a needle, put one drop of superglue on the adapter surface, avoiding contact with the wires. Quickly lay the five-pin male-to-female adapter inside the guide and close the adapter with the top lid. Keep pressure on the top lid until the superglue dries off, possibly adding some extra drops of glue around the lid.

   (i) Put a few drops of superglue by the waveguide slot to stabilize the waveguide position inside the adapter.

   (j) When the super glue has dried completely, remove the tape from all the microwires and cut the extra parts outside the waveguide and the adapter (except for the ground wire).

   (k) Add some drops of super glue at the end of the waveguide to encapsulate the end of the four microwires.

   (l) Repeat Steps (b-k) for each sample.

   (m) Clean the surface of the samples with some drops of de-ionized (DI) water on a single-use wipe, let dry and store in an appropriate container.

Chapter 5

Characterization

This chapter concludes the experimental work of this project, illustrating the methods and results from the main characterization activities carried out in the process. Section 5.1 deals with optical characterization and reports on the results from the transmission spectra and the space-resolved scattering measurements on the waveguide. Section 5.2 illustrates the electrochemical impedance spectroscopy technique applied to characterize the tungsten electrodes. Finally, Section 5.3 reports on the acute *in-vivo* study of the fully-connectorized implant, under collaboration with the University of Copenhagen.

5.1 Optical characterization

5.1.1 Transmission spectra

The characterization of the optical properties of the waveguide was done with the cutback method. The setup, represented in Figure 5.1a, consisted of a SuperK Extreme supercontinuum laser by NKT Photonics (400-2400 nm), coupled with an input silica fiber. The laser power during measurement was always set to 100% (corresponding to 2.2 W), and the repetition rate to 500 kHz. The fiber is manually aligned with one end of the polymer waveguide on a compact flexure stage (Thorlabs MBT616D/M). The second end of the fiber is also aligned and coupled with an output silica fiber, which sits on another three-axis flexure stage. For each measurement, the second end of the fiber was cut by the desired length (measured with a ruler), taped back to the flexure stage, and realigned. The output silica fiber was connected to an optical spectrum analyzer (OSA) (ANDO AQ-6315A), which was used to both tune the alignment at the output of the POF by maximizing the output power (in this case at 1064 nm, the peak wavelength of the laser source) and to read the output spectra, which were then saved on a floppy disk. The OSA was set up for 10 nm resolution and the sensitivity to 'High 1'. The data could then be read with a simple Matlab script.

To determine the waveguide losses, the cutback technique was used. The technique consists of performing the spectrum measurement on a relatively long waveguide sample, cleaving the fiber by a known length at the output end, repeating the measurement on the fiber, and subtracting the spectra to determine the properties of the short piece of fiber. Because of the inaccuracy of a single manual cleave, one needs to perform multiple cuts and average the results per unit of fiber length.

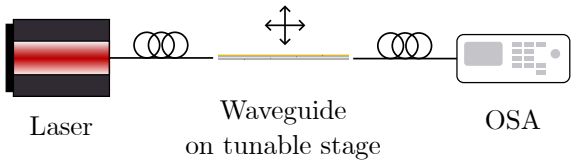

(a) Schematic representation of the setup for measuring the attenuation spectra. The SuperK laser is coupled into a silica fiber, which is free-space coupled into a 50 cm piece of fiber on a flexure stage. An output silica fiber is also placed on a flexure stage to adjust the relative position between the waveguide and both silica fibers. The output fiber is connected to an OSA for displaying and saving the spectra.

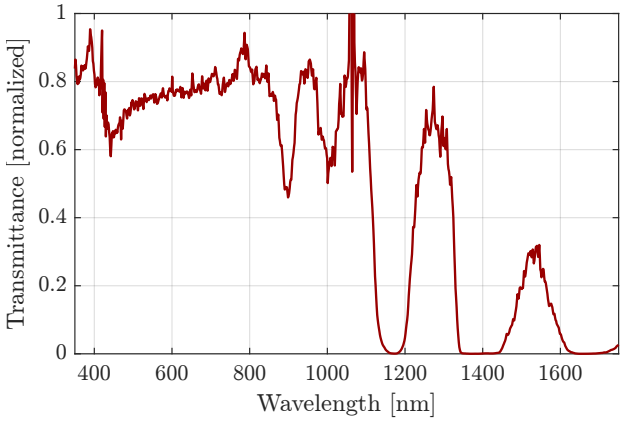

(b) Transmission spectrum of the waveguide, normalized to the peak at 1064 nm.

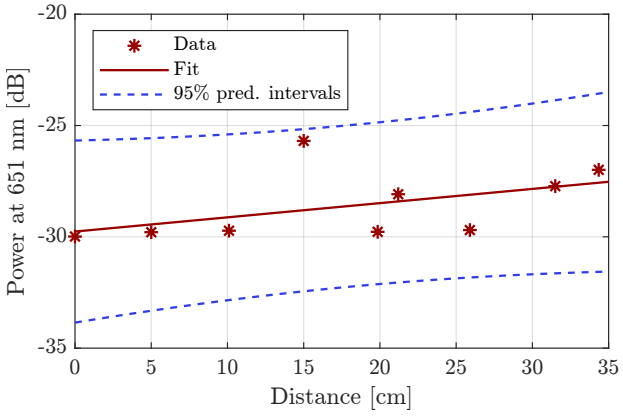

(c) Recorded power at 651 nm for the different cuts along the waveguide.

Figure 5.1: Attenuation measurements in the PMMA waveguide.

The technique to determine the hole scattering losses is similar. A waveguide with a series of holes is cleaved by one hole at a time, and after subtracting the waveguide losses (found in the previous step), the effect of the scattering can be isolated.

50 cm of fiber were divided as follows: 20 cm to determine the waveguide losses, 10 cm with nine equally-spaced holes, and 20 cm more for waveguide losses. First, a spectrum (Figure 5.1b) of the transmittance for the waveguide is calculated by dividing the trace by a reference measurement done with input and output fibers directly coupled. The typical features of PMMA transmittance can be observed, such as the dip around 420 nm due to electronic transitions and those at 1200 and 1400 nm, which are associated with molecular vibrations. The absorption in the NIR range appears to be particularly intense, which might suggest stronger molecular interactions for this combination of material and impurity composition. Moreover, the peak transmittance is found at 1060 nm (arguably due to a shift in the peak wavelength of the laser source), and the transmission is rather flat in the visible range. It is important to stress that the y-axis on the graph is normalized to the peak at 1060 nm, as a direct comparison with the power of the reference measurement is not significative. Due to the very low coupling efficiency, especially between the larger waveguide output and the silica fiber connected to the OSA, a large part of the light would be lost, giving a much lower transmittance than the real value.

After performing several cuts along the sample, the peaks at a specific wavelength (651 nm) were extracted for each trace and compared against the distance of the cut. The resulting linear fit, shown in Figure 5.1c, gives an average attenuation coefficient of 6.39 dB/m. As the 95% prediction intervals

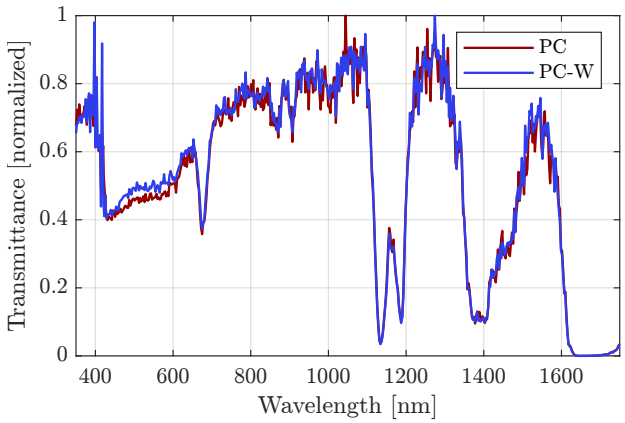

Figure 5.2: Normalized transmittance spectrum of the PC waveguide, before and after inserting the tungsten microwires.

show, the linear fit has a considerable amount of error, arguably introduced by the different cleavages.

As regards the portion of the waveguide containing the holes, whose peaks have been removed in Figure 5.1c, no statistically-significant results could be obtained for the scattering power caused by the hole, as the obtained peaks showed no trend. It is likely that the optical power scattered by the holes is too low to be recorded with this technique, as it is lower than the fluctuations introduced by the different cleavages for each hole. Consequently, the scattering measurements were obtained differently for the following samples, as reported in the following subsection.

As regards the final PC-W waveguide, a 50 cm-long piece of waveguide with uniform diameter was unavailable after the preparation of all the devices for the electrical and electrophysiological characterization. Therefore, only the transmittance was characterized. Figure 5.2 reports the transmittance spectrum for a 5 cm microstructured PC waveguide before and after the insertion of the tungsten microwires, obtained with the same setup as Figure 5.1a. As one might expect, the two traces closely overlap, as the effect of the scattering elements introduced by the microwires on wavelength, given their 50 µm diameter, is negligible. Overall, the PC waveguide presents a dip at 670 nm, which might originate from the absorption by some impurities embedded in the waveguide. It is worth stressing that the spectrum is still normalized to the peak transmittance (observed at 1044 nm and 1272 nm, respectively).

5.1.2 Hole-induced optical scattering

The upward optical scattering produced by the holes was quantified by optical power measurements. The NKT SuperK (output power set to 100%) was again coupled to a silica fiber, which was taped on a flexure stage. The sample was then manually aligned on another stage with the holes facing up, and the position was optimized using a spectral power meter (Thorlabs PM100USB) with a 50 µm-core patch cable and connected to a PC interface to record the spectral optical power in real-time (the wavelength was set to 632 nm). Figure 5.3a gives a schematic representation of the setup. The probing cable was mounted on a third stage and taped to stand vertically above the device to measure the vertically-scattered light. Figure 5.3b shows the illuminated device (the four scattering points are visible in the reflection of the metal slab) and the tip of the probe.

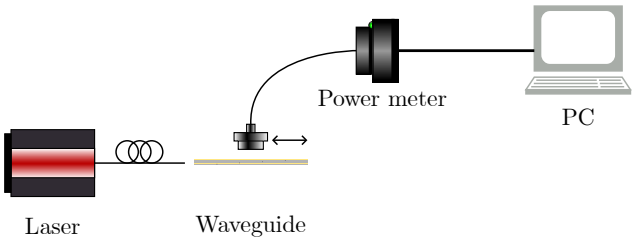

(a) Schematic representation of the setup for the scattering measurements. The SuperK laser is coupled onto a silica fiber, which is free-space coupled into the waveguide sample on a flexure stage. A patch cable is installed vertically on another flexure stage to scan horizontally along the waveguide length. The collected power is measured by a power meter and read in real-time on a computer interface.

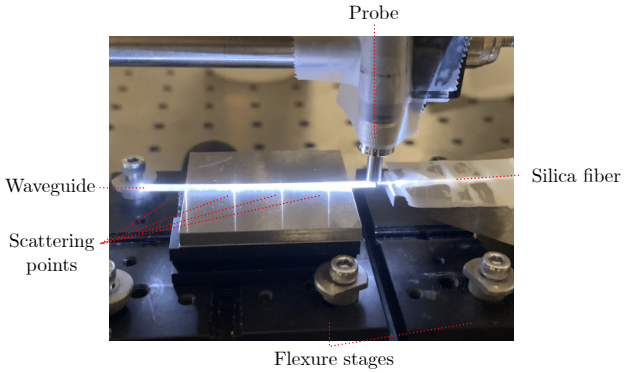

(b) Close-up of the experimental setup for the scattering measurement, showing the patch cable positioned at the beginning of the waveguide.

Figure 5.3: Experimental setup for the characterization of optical scattering.

Starting from the beginning of the device, the probe was scanned over the height and width to optimize the collected power. Then, the probing flexure stage was moved by 0.5 mm towards the end of the device, and another measurement was collected. This was repeated until the end of the fiber, thus obtaining about 100 optical power measurements. This technique enables a map of the light intensity above the waveguide, shown in Figure 5.4a for the device without electrodes. The initial and the end peaks correspond to the reflection and transmission of light at the ends of the fiber. The second peak (at about 6 mm) is caused by the reflection of the metal slab below the device and not by a scattering point in the device. The following four peaks, on the other hand, correspond to the machined holes. Above each peak of Figure 5.4a, there are four cropped pictures of the scattered light from each hole obtained from a DinoLite portable digital microscope, which was also mounted vertically to image each scattering point on the sample.

The output optical power was recorded by the same cable to estimate the scattering of the fiber. The highest output power value obtained was 4.51 mW at 632 nm; hence the scattering of each hole peak is estimated to be about 0.01-0.02% of the output power. This result is only indicative, as the scattering should be calculated by integrating the power over a much larger area than the aperture of the cable.

The same evaluation was performed on a device with four tungsten electrodes, and the obtained results (Figure 5.4b) are similar to those obtained for the device without electrodes, showing that

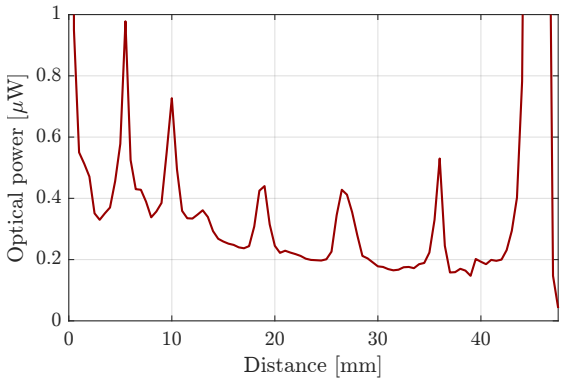

(a) Optical power against the position of the probe without electrodes.

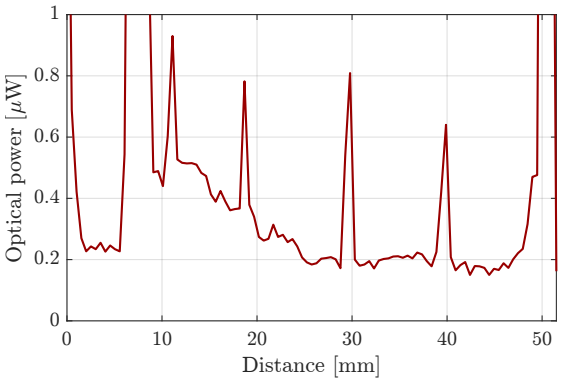

(b) Optical power against the position of the probe with electrodes.

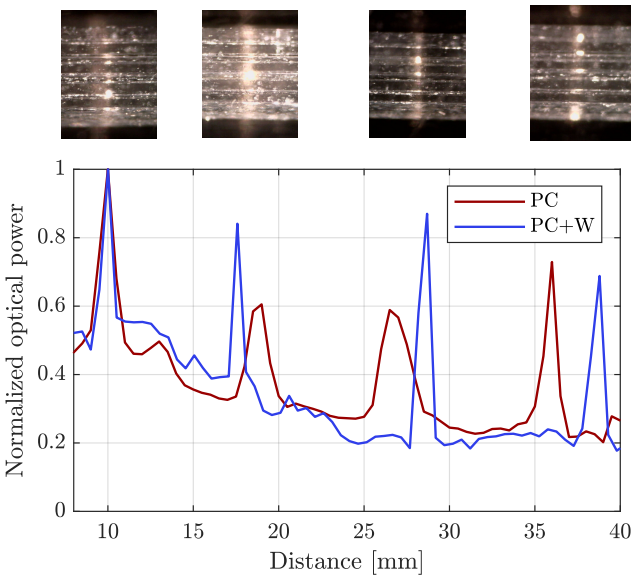

(c) Comparison of the scattered optical power normalized with the first scattering peak. The insets show a photograph of the waveguide at each scattering point.

Figure 5.4: Optical scattering measurements for a PC-W device.

the tungsten wires do not significantly impact the scattering results. Figure 5.4c compares the optical power from the previous plots, normalized by the scattered power at the first peak. When far from the holes, the scattered light has a decreasing trend in both cases, but the second and third peaks appear sharper in the fiber with electrodes. Given the size of the holes (about 70 µm) and the resolution of this measurement (500 µm), however, it is likely that the maximum scatter was not recorded at the exact maximum. In fact, the rounded peaks of the second and third holes in the fiber without electrodes seem to hint at a higher maximum between the two highest points.

5.2 Electrochemical impedance spectroscopy

The electrodes were characterized via a setup for EIS, a powerful tool for analyzing electrified interfaces such as electrochemical biosensors [81]. It measures the response (current or voltage) of a system to an applied small-amplitude voltage or current perturbation over a wide range of

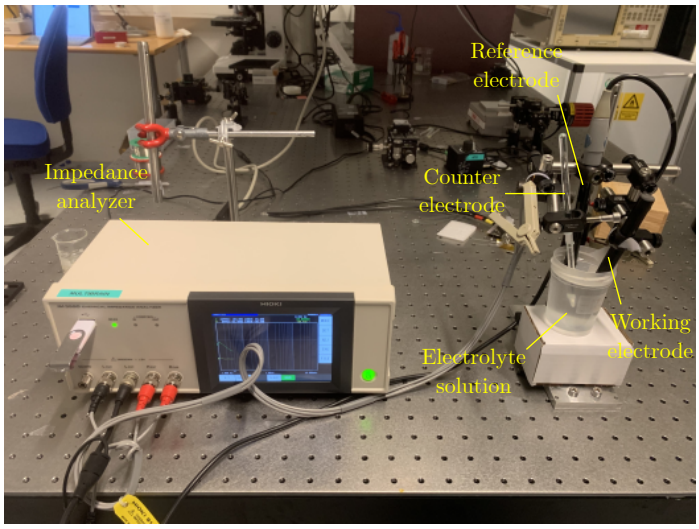

Figure 5.5: Experimental setup for electrochemical impedance spectroscopy.

frequencies so that a complex transfer function (namely the impedance) can be calculated. In EIS, the interactions include the concentration of electroactive species from the bulk solution where the electrode is inserted to the electrode surface [82].

The setup for EIS is shown in Figure 5.5. The chemical impedance analyzer (Hioki IM3590) runs in the 3-electrode mode. In this configuration, there is a working electrode (the tungsten microwire from the device), a counter-electrode (also made of a tungsten microwire, wrapped around a glass rod), and a reference electrode made of silver/silver chloride (Ag/AgCl) (Mettler-Toledo InLab Expert Pro pH electrode). The impedance analyzer features four terminals: low current, low voltage, high current, and high voltage. The low-current terminal is connected to the counter-electrode, and the low-potential to the reference electrode. The high-current and high-voltage terminals are connected to the clamp for the working electrode. Impedance is measured by applying a potential to the working electrode and recording the resulting current, and it is governed by three processes: the charging/discharging of the electric double layer at the electrode/electrolyte interface, the kinetics of the faradaic reaction (namely the electric current generated by the redox reaction at the electrode), and the diffusion of the redox species from the bulk to the electrode surface. Each process is characterized by a different time constant, the redox species diffusion generally having the longest stabilization time [83].

The probed sample consisted of a micromachined piece of waveguide (about 3 cm) with tungsten wires fit inside the channels. The microwires were cut on one end, and superglue was used to insulate the wires and fix them in place. On the other side of the waveguide, the microwires were kept long to ease the clamping. The waveguide was taped to a dielectric rod so that the holes could be placed inside the solution while the protruding microwires were facing up. For each measurement, a single electrode from the four microwires was individually connected to the metal clamp (adhesive tape was used to ensure the microwires did not short-circuit), thereby closing the circuit. All three electrodes were then placed inside a 0.01 M phosphate-buffered saline (PBS) solution, a water-based saline solution containing disodium phosphate and sodium chloride.

LCR mode, which provides an instant readout of the impedance at a given frequency (which

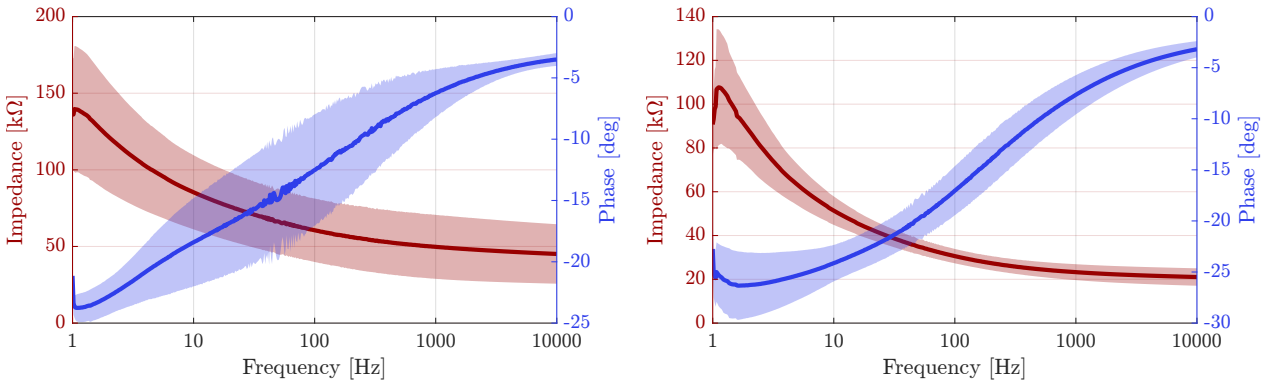

(a) Bode plot of the impedance, with the measurements obtained on the first day.

(b) Bode plot of the impedance, with the measurements obtained on the second day.

Figure 5.6: Results from the electrochemical impedance spectroscopy, separated in absolute value and phase, with the shaded area showing one standard deviation.

was set to 1 kHz in the experiment), was used for stabilization; when the measured impedance did not rapidly vary by more than 1 kΩ, spectra from 1 Hz to 10 kHz were measured, with a voltage setpoint of 1 V. The impedance magnitude and phase information was saved on a USB drive and later processed on a computer. One set of measurements was taken shortly after the insertion of the device in the PBS solution and included several recordings for each electrode. The second set of measurements was recorded after 24 hours of soaking time for the device to assess the difference in the results between the two cases. The results are reported in Bode plots (where magnitude and phase are reported) in Figure 5.6, where the standard deviation is shown as the shaded area around the mean value. The error for the impedance magnitude has, on average, decreased by 42% between the two measurements, while the phase error has decreased by 25%. The average error for the absolute value of the impedance was 35.3% for the measurements on the first day, but it decreased to 14.7% after 24 hours of soaking, suggesting a higher degree of stabilization of the electrolytes on the electrode surface.

The main ranges of interest for the impedance are those matching the neural signals, which are divided into action potentials (whose frequencies are typically around 1 kHz) and local field potentials (whose range lies between 0-150 Hz), as explained in Chapter 2. The average electrode impedance at 1 kHz was 23 ± 4 kΩ and below 100 Hz it varied between 30 and 133 kΩ, which is comparable to state-of-the-art recording probes featuring metallic electrodes with similar dimensions [64, 80]. Incidentally, the phase indicates that the reactance (namely the imaginary part of the impedance) decreases as the frequency increases, the negative sign indicating a capacitive reactance, which is coherent with the usual behavior of high-frequency electrical circuits.

5.3 *In vivo* electrophysiology

The fully-connectorized interface was finally tested under an *in vivo* study at the Panum Institute of the University of Copenhagen. The surgery took place in the Berg Lab of the Department of Neuroscience. While the lab is equipped for optogenetic studies, the preparation of such a study

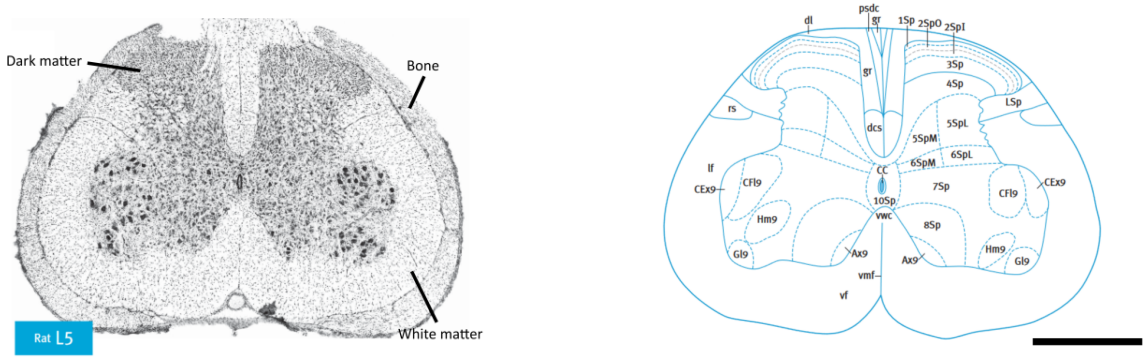

(a) Photograph of a Nissl stained transverse section from the spinal group L5.

(b) Detailed diagram of the spinal cord segment, delineating the significant neuronal groupings.

Figure 5.7: Cross section of the crural motoneuron group L5. The scale bar measures 1 mm. Adapted from [84].

requires considerably more time due to the additional required steps, such as the virus injection and manifestation, as well as a longer surgical operation, given the need of stitching the spinal cord and of recovery time. Therefore, the device was tested exclusively for its electrical features, that is with electrophysiology. On this matter, it is worth stressing that while the lab is equipped with a setup for electrophysiology, it is not shielded from external electromagnetic radiation; hence a considerable amount of noise from the surrounding might affect the electrophysiological measurements.

5.3.1 Surgical method

An adult (about 4 to 5 months old) female rat of 300-400 g was used for the experiment. Female rats generally have a thinner layer of fat and connective tissue; hence, the spinal cord is closer to the epilayer, thus easing the surgical procedure. The method for surgery is briefly described as follows:

1. All the metal tools and surfaces employed for the surgery are sterilized with an ethanol solution at 70%. Moreover, the tools are sterilized in a 250 °C heat sterilizer. Round and spear swab tips are also prepared.

2. The anesthetic (Attane Vet 1000 mg/g Isoflurane) is loaded into a metal tank and mixed with oxygen.

3. The rat is placed in a box for anesthesia for several minutes. Once the rat is sedated, it is moved outside, and a rectangle of fur is shaved with an electric shaver on its back, where the surgery will be performed (Figure 5.8a). The residual fur is removed with tape, and the skin is cleaned with chlorhexidine first and then ethanol.

4. A local anesthetic (Lidor Vet. 20 mg/mL) is injected into the spinal cord with a syringe. The rat is then moved to the surgical station on a heating mat at 37.1 °C to avoid rapid body heat loss while sedated (Figure 5.8b).

5. A window is cut on a surgical drape, roughly the size of the shaved area, and is put above the animal to prevent infection from contamination from the non-sterile areas. A sterile transparent

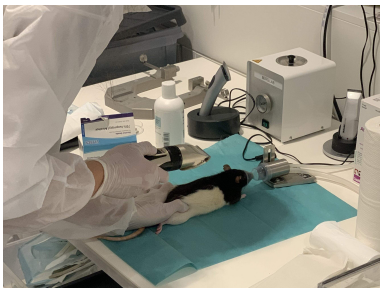

(a) Preparation of the sedated animal.

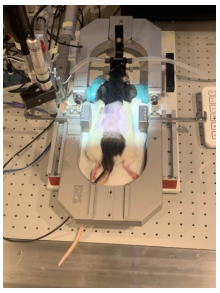

(b) Mounting of the animal on the surgical station.

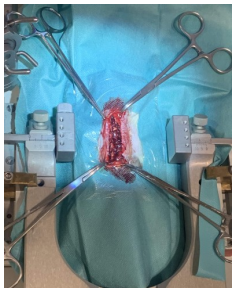

(c) Incision and clamping of the connective tissue with forceps.

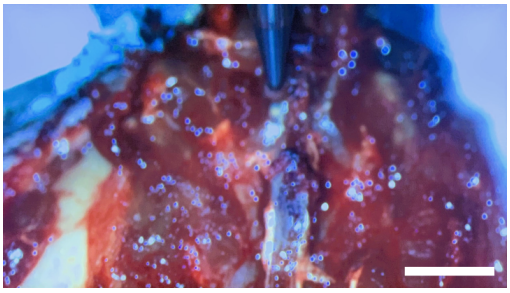

(d) Microscope picture of the drill tip performing a hole on a bone. Scalebar represents 1 cm.

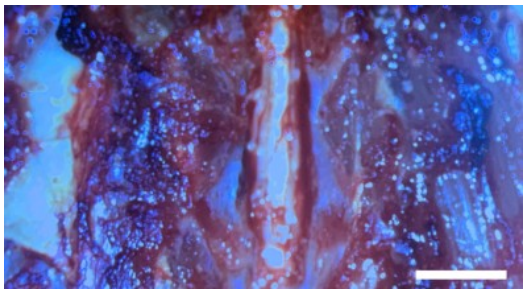

(e) Microscope picture of the spinal cord exposed after drilling. Scalebar represents 1 cm.

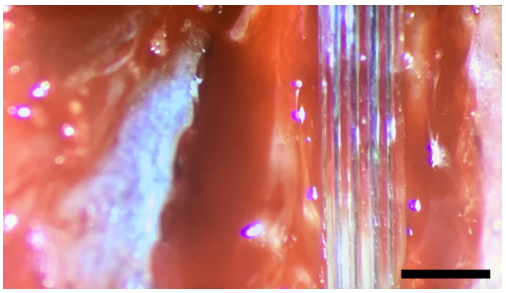

(f) Microscope picture of the implant in contact with the spinal cord. Scalebar represents 1 cm.

Figure 5.8: Photographs of the surgical procedure.

film is then placed on top of the cut window of the drape. The surgical setup is finally completed with a mount to clamp the spinal cord and keep it in place later.

6. An incision is performed along the spinal cord, opening up the epilayer, the connective tissue, the fat, and the muscle layers. The connective tissue is clamped with forceps, as vertebras are exposed (Figure 5.8c). Six vertebras are cleaned and exposed; while only four vertebras must be removed to accommodate the device, two extras are needed at the ends to clamp the spinal cord during the surgery.

7. The vertebras are clamped to hold them in place. With the aid of a surgical microscope (Leica Microsystems), the four vertebras are drilled to remove the bone layer protecting the spinal cord (Figure 5.8d). Figure 5.7 illustrates the cross-section of one of the groups (the crural motoneuron group L5), with a Nissl stain (Fig. 5.7a), namely an imaging technique that uses dyes to stain genetic material permanently, and a diagram highlighting the most significant neuronal groupings. The outer gray layer indicates the bone around the spinal cord, the darker gray corresponds to gray matter (containing the neurons), and the lighter gray to white matter

(void of neurons).

8. The final adjustments are made with the drill placed at an angle to slowly expose the spinal cord until it can clearly be distinguished with the surgical microscope (Figure 5.8e).

5.3.2 Electrophysiology

The setup for electrophysiology, shown in Figure 5.9a, consists of a computer with the Intan Technologies RHX Data Acquisition software, an RHD USB interface board, a preamplifier for extracellular recording (characterized by a high gain and a high input impedance) and a connector to plug in the device. An optical ferrule is also connected to the optical port of the interface to convey light from a red LED. As mentioned above, the study merely dealt with electrophysiology; however, optical light was used to demonstrate the visibility of the scattering points when the waveguide is coupled to a source for future studies including photosensitive opsins for optogenetics. The method used for the electrophysiology evaluation is explained below.

- A software-controlled motorized stereotaxic (Neurostar Stereodrive) is used to mount the connectorized device (length = 1.5 cm) at an angle so that the position on top or inside the spinal cord can be finely tuned with a micromanipulator. A picture of the probe with the coupled red LED turned on is given in Picture 5.9b, where the inset displays a magnified portion of the picture showing the four scattering points of the interface.

- The electrophysiology setup is turned on, and the computer interface (Intan Technologies RHX software) is loaded.

- The electrophysiology system supports up to 16 channels. The four channels connected to the electrodes are thus found by using a slightly conductive PBS solution and observing the oscillations of the recorded signals. Due to the amount of noise, this test did not give clear results. However, by applying a wide filter in the software, major movements (such as the respiration rate of the animal) can be observed and used to distinguish the active channels. A 50 Hz notch filter is applied.

- The probe is lowered, and the waveguide is slid in contact with the spinal cord (Figure 5.8f and Figure 5.9c). The ground wire is also bent to be in contact with the animal's blood so that most of the noise is removed from the channels.

- A first recording of 10 minutes is carried out. When applying a highpass filter, the recorded noise level was low, with about 20 µV peak-to-peak voltage noise in Channels 13-16. The expected spike amplitude is about 100 µV. However, it is worth underlining that the neurons are still relatively distant from the tungsten wires in the hole; hence, their signal might be very weak when reaching the electrodes.

- Since the neurons on the surface of the spinal cord are difficult to target, it is more likely to detect signs of LFP rather than single-unit recording. An incision on the spinal cord is performed to get closer contact with the neurons so the probe can slide inside and reach the

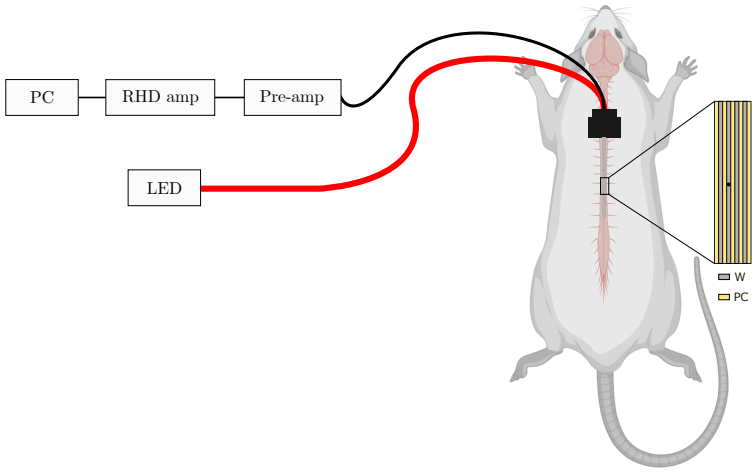

(a) Sketch of the setup used for electrophysiology. The recorded signal is pre-amplified, recorded by the interface board, and displayed on the computer with the graphics interface. The red LED source is used to show the micromachined holes. Drawing of the rat reproduced from BioRender.

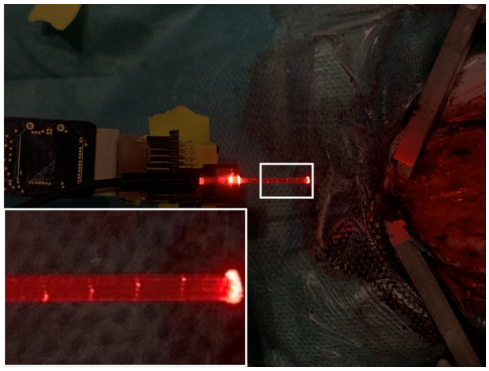

(b) Top view of the first implant, before the contact with the spinal cord. The four scattering points are magnified in the inset.

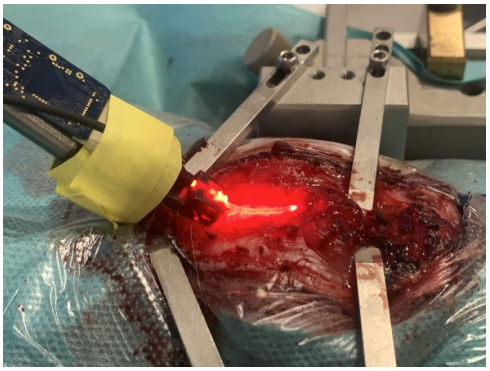

(c) Side view of the first implant in contact with the spinal cord. The flexible substrate accommodates the shape of the spinal cord.

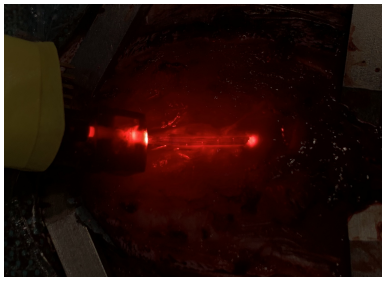

(d) Top view of the second implant of 2.5 cm in contact with the spinal cord, showing its four bright scattering points.

Figure 5.9: Neural interface implant on the spinal cord for electrophysiology.

gray matter region (see Figure 5.7). The probe is inserted into the spinal cord and moved deeper to reach the gray matter. Three sets of measurements are taken at different heights (about 1.4, 1.6, and 1.8 mm inside the spinal cord). As the photograph of the cross-section illustrates, the holes on the waveguide must be neither too up nor too down, as those regions contain white matter, where neural activity is very difficult to detect.

- Two other sets of three measurements are taken by changing the entry position for the waveguide.
- A second device (of length 2.5 cm) is tested with the same approach as the first one to compare the results between the two. All sixteen channels were recorded for this device, and two sets of measurements were collected. Figure 5.9d shows a picture of the second implant bent on the spinal cord and its four bright scattering points.

The software comes with some default filters: WIDE (the default one, also used to save the data), HIGH (a highpass filter, useful to detect single-neuron activity), and LOW (a lowpass filter, useful to detect collective actions from the local field potential. However, the traces are recorded without any filtering but the 50 Hz notch filter. The following subsection further elaborates on the post-processing filters used to reveal the signals and includes some comments on the findings.

5.3.3 Post processing (device 1)

The collected data for the first device, which came with a .rhd extension, were converted with a Matlab file reader script (Version 3.0) downloadable at the company website [85]. Each trace contains information about the number of amplifier channels (8 for the first device and 16 for the second one), the frequency parameters (a data structure containing, among others, the amplifier sample rate and the notch filter frequency), the timestamps of each recording and the amplifier data. This subsection is further divided into two: the first part deals with the time-domain investigation of high-frequency action potentials in the traces, while the second part reports on the frequency-domain findings related to local field potentials.

Action potentials

Figure 5.10 summarizes the post-processing steps for finding the action potentials. The raw data are displayed as 180 s traces (Figure 5.10i). From this, the power spectral density (PSD) can be estimated via the periodogram plot, shown below the time-domain trace. Signal windowing is used to contrast the finiteness of the signal, which in real-life recordings has a limited length [59]. While a longer signal is preferred over a short one (as it reduces the sidebands of the signal when performing a Fourier transform), the signal is always bound to end, and windowing is done to partially compensate for the problem. The signal is reduced in amplitude close to the bounds by multiplying it with a function (the so-called window) that approaches zero at the boundaries. This window function be a simple rectangular function or a function that reduces the signal amplitude more slowly (such as a Hanning or a Gaussian function). Different window functions can considerably impact the frequency domain when the signal is arbitrarily truncated and does not terminate at the end of its period (which is almost always the case when sampling real-world signals). In that case, a smoother window function helps reduce broadening effects in the frequency domain.

The first step for post-processing is rectifying the signal, namely removing the lower-frequency portion of the signal. A simple window-based HP filter was designed to rectify the signal. A Kaiser window with $\beta = 2$ was observed to have a steep enough magnitude response to filter out the lower frequencies. A comparison of a portion of the unfiltered signal and three different HP filters (at 100,

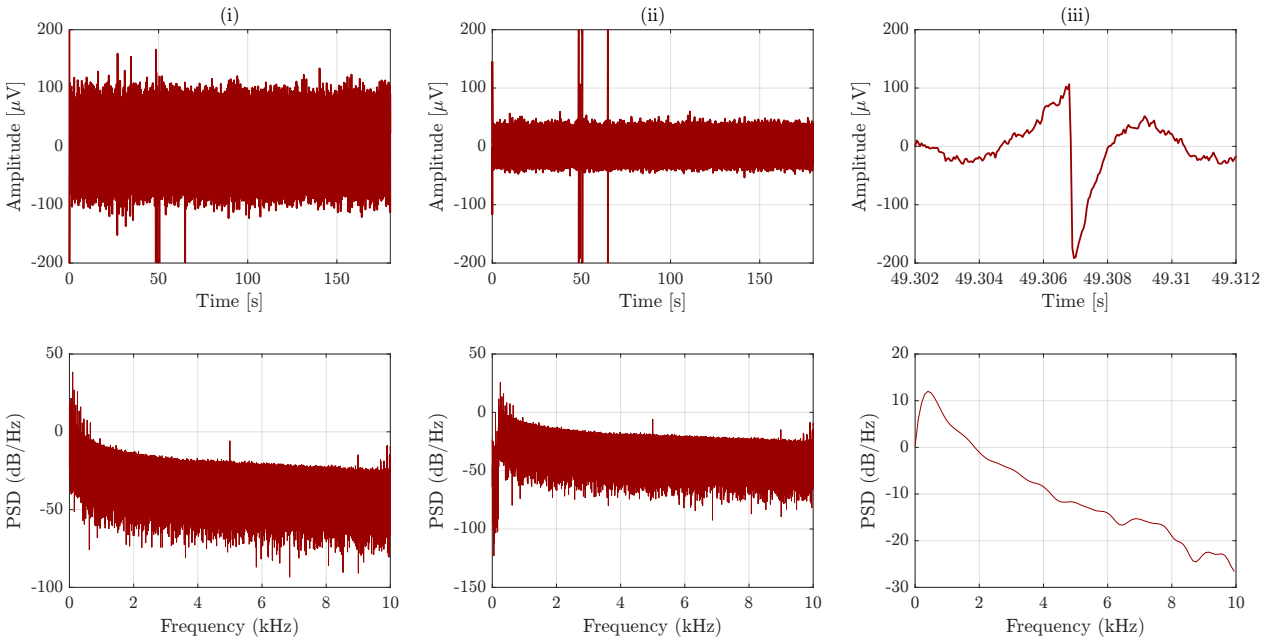

Figure 5.10: Processing steps for the traces, showing (i) the raw signal, (ii) the rectified signal after removal of lower frequencies, (iii) a spike found by setting an appropriate threshold and finding local minima. At the bottom, the corresponding PSD for all the signals.

200, and 300 Hz) is shown in Figure 5.11a. With a filter at 100 Hz, one can notice the decrease of slow oscillations in the signal. As the cut-off frequency increases, faster oscillations also begin to disappear, and the signal amplitude further weakens. A good compromise between low-frequency filtering and the ability to find spikes on the channel was found to be 200 Hz. Figure 5.11b reports the magnitude response of the three Kaiser filters.

The rectification of the signal is reflected in Figure 5.10ii, from both the reduced amplitude and the damped lower-frequency portion of the spectrum on the calculated PSD, when compared to the trace in Figure 5.10i. The spikes were then found by building a script finding all the local minima within a specified threshold (where the upper bound was below the noise level, and the lower part was usually above -200 or $-300\,\mu V$, to filter out any measurement artifacts), a typical feature of an action potential, as previously seen in Figure 2.4. Adjacent local minima were then compared within a threshold of 10 ms, and only the lowest dip was maintained to avoid recording the same spike multiple times. Figure 5.10iii shows an example of an action potential. Given the short time window of this portion of the signal, the PSD is not as accurate as the full trace; nevertheless, it suggests that the main spectral density band is concentrated around 1 kHz in the frequency range.

As mentioned above, eight channels were recorded during electrophysiology for the first tested device. Due to channel crosstalk, the other channels available in the RHX interface, which had no wiring to any electrode, acted as antennas, propagating the recorded signal in the other channels, as well [86].Given the noise level and the arrival times for the spikes, it was possible to distinguish the resonant channels from the recording ones. The measurements from such channels were thus isolated, leaving four channels to analyze, each corresponding to one electrode. Figure 5.12a displays an overlap of all the detected action potentials per channel (in gray) and the average lineshape from

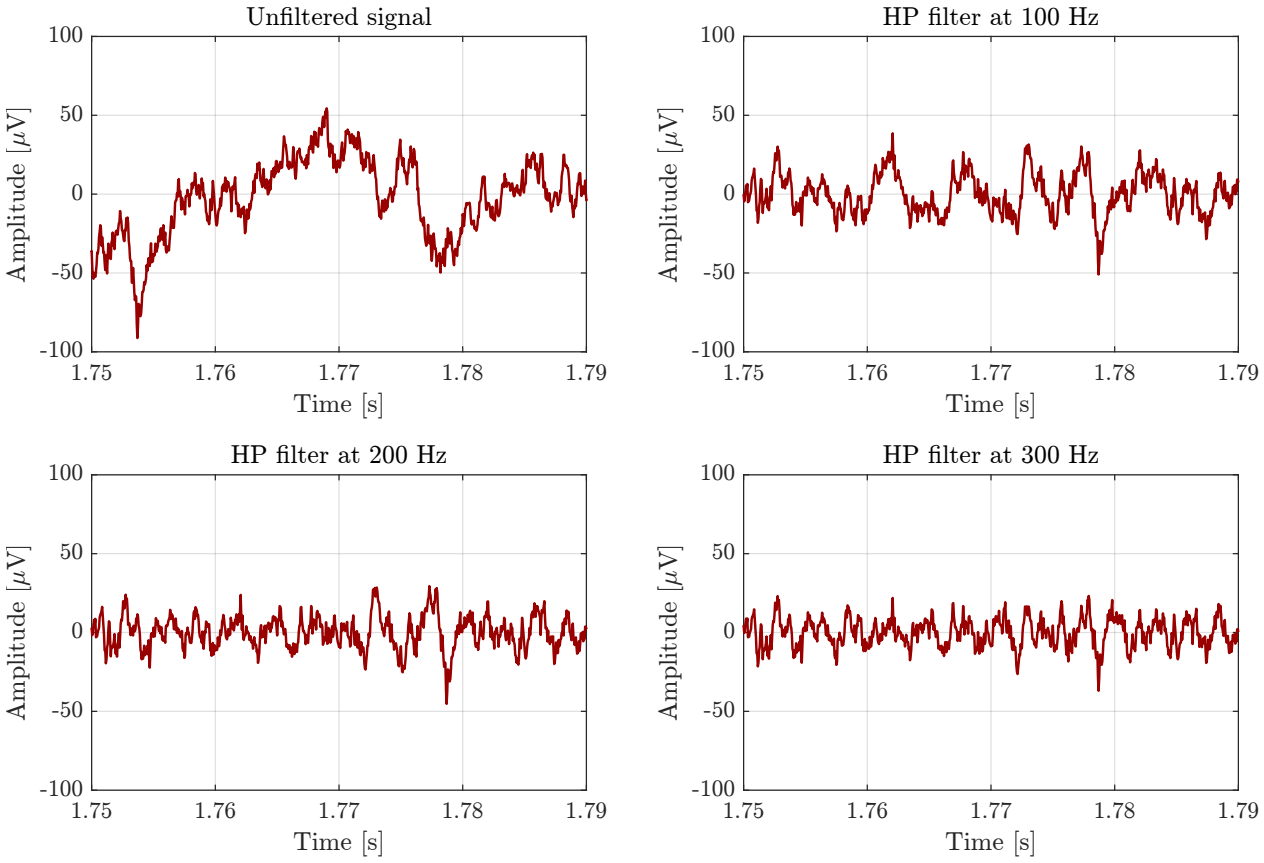

(a) Comparison of a section of an unfiltered signal and three highpass filters at 100, 200, and 300 Hz. The signal is progressively rectified, improving the chances of detecting a high-frequency action potential spike, but some information is lost, and the signal amplitude is considerably decreased.

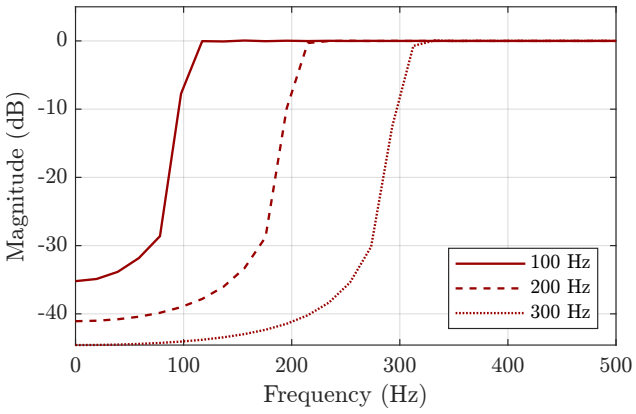

(b) Magnitude response of the designed high-pass (HP) filters used above.

Figure 5.11: Highpass filters tested on the signal traces.

the spikes (in black). The overlap shows a clear trend of the spikes found by the script. In Channel 2, one can notice a false-positive spike, whose slope is first decreasing and then increasing, which does not correspond to the depolarization-repolarization cycle of a biological action potential. Except for this spike, all the others show the increasing potential with depolarization, and the subsequent dip during the repolarization phase, which suggests that the collected spikes indeed came from recorded neurons. Comparing the average lineshape with the one reported in Figure 2.4, as well as in other

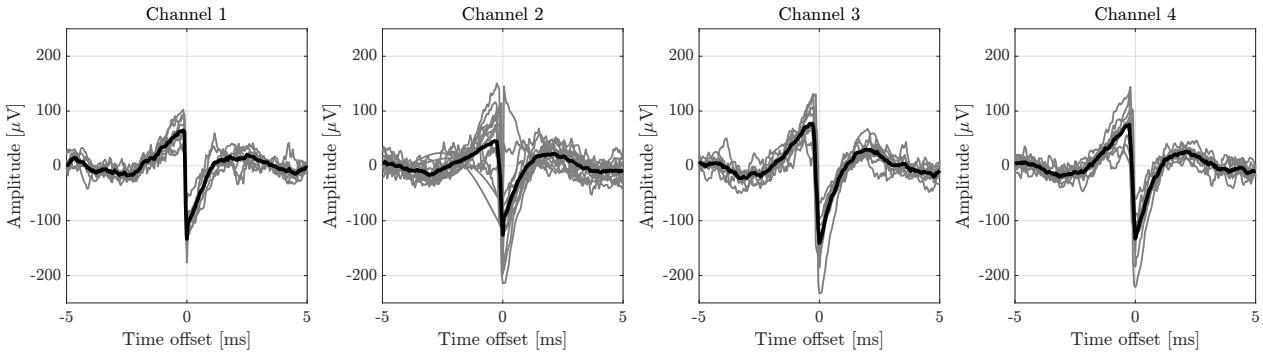

(a) The action potentials detected for all the recorded channels (gray) and the average of all the signals (black).

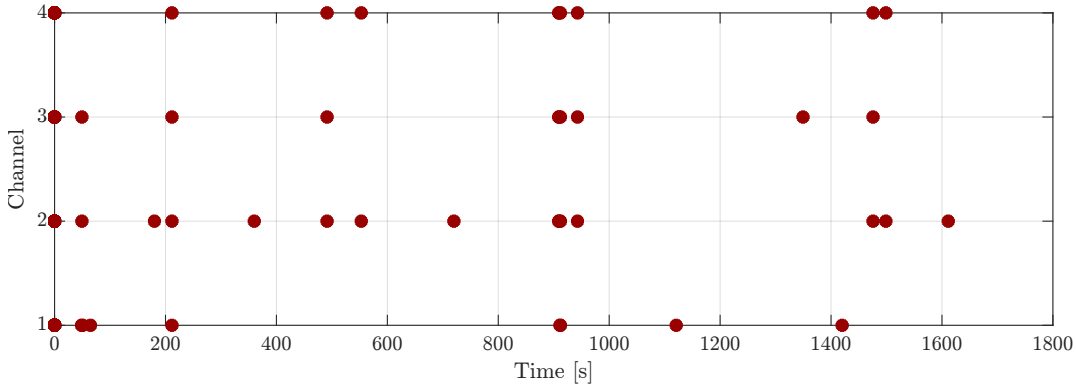

(b) Detected action potentials over time, separated into channels. Each dot marks an action potential event. Most recordings occur in multiple channels, indicating a strong cross-correlation between channels.

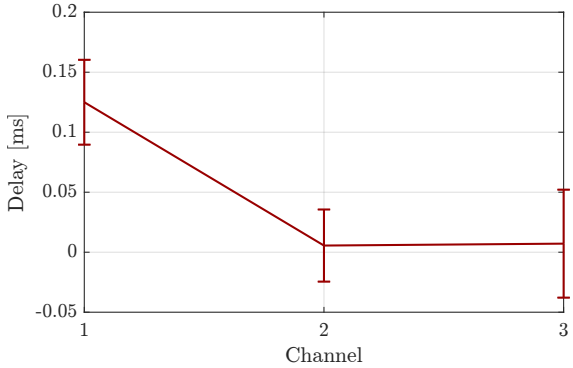

(c) Delay of action potential spikes from Channel 4 to Channels 1, 2, and 3, shown with one-sigma error bars.

Figure 5.12: Action potential activity recorded with the first device.

works (e.g., the action potential along the spinal cord in dogs of [87]), it appears that the matching is close enough to conclude that the recording was effective. Moreover, the PSD of the spike traces of Figure 5.10(iii), which peaks around 1 kHz, matches the expected value from the literature [86].

Figure 5.12b reports the recorded spikes as a function of time for the entire recording period. While some action potentials appear in single channels, most spikes appear in two or more channels (corresponding to two or more dots vertically aligned), suggesting that the neural signals might have been recorded as they travel up or down the spinal cord. To test the hypothesis, the delay between coinciding spikes was calculated. Figure 5.12c reports the delay calculated from Channel 4, which corresponds to the furthest hole from the rat brain. Channel 4 shows, on average, a positive delay with respect to all three other channels. While the error is high and the sample size should be

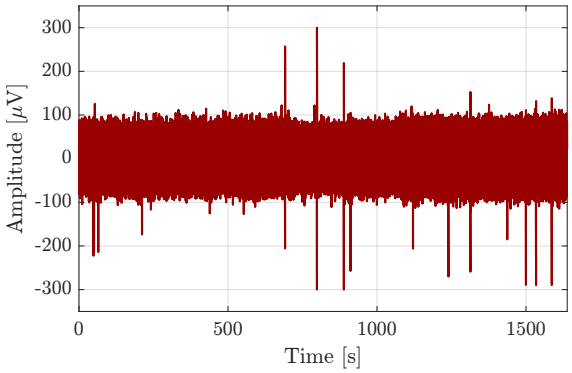

(a) Signal obtained from merging all the traces of the first channel, in the time domain.

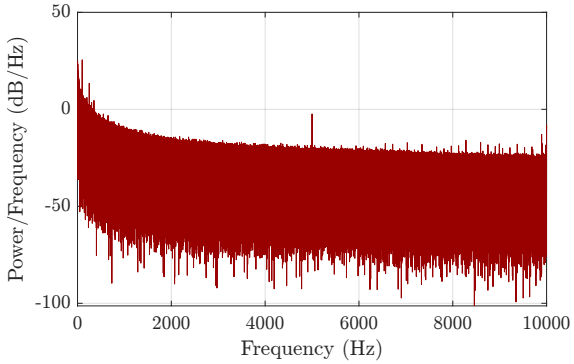

(b) Signal obtained from merging all the traces of the first channel, in the frequency domain.

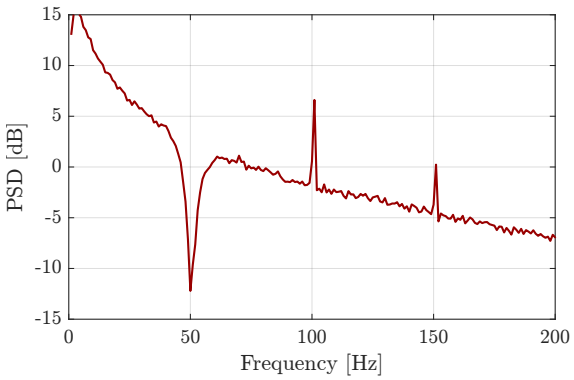

(c) Discretized power spectral density at low frequencies for the first channel.

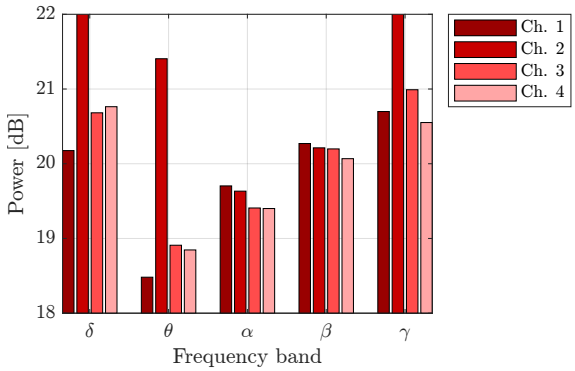

(d) Bar graph showing the power of the trace, divided into the frequency bands of neural oscillations.

Figure 5.13: Analysis of the neural oscillations along the whole recorded trace.

increased for the graph to be conclusive, the decreasing delay with the channel number hints at a tendency for the action potentials to propagate from the brain down towards the lower end of the central nervous system. Moreover, it is worth noting that many spikes occur within one or two time samples from the others, meaning that a sampling rate higher than 20 kHz might benefit the accuracy of the measurement. Alternatively, a longer device with further-distributed holes would increase the signal travel time between holes, which should correspond to less error in the plot. The estimated average speed for signal propagation (also referred to as conduction velocity) was 53.56 ± 36.62 m/s. As mentioned above, the high error makes this result inconclusive. However, such conduction velocity is compatible with values found in faster-propagating neural signals, such as those fired by myelinated nerve fibers [67].

Local field potentials

Finally, a power spectral analysis was carried on with the collected traces. While action potentials are characterized by high-frequency spikes, local field potentials occur at low frequency (less than 300 Hz), as described in Section 2.5.2. This analysis was done by merging all the traces, obtaining a signal of about 27 min, which is shown in Figure 5.13a for the first channel. The corresponding PSD is given in Figure 5.13b, and similarly to previously shown PSDs, shows the highest spectral density

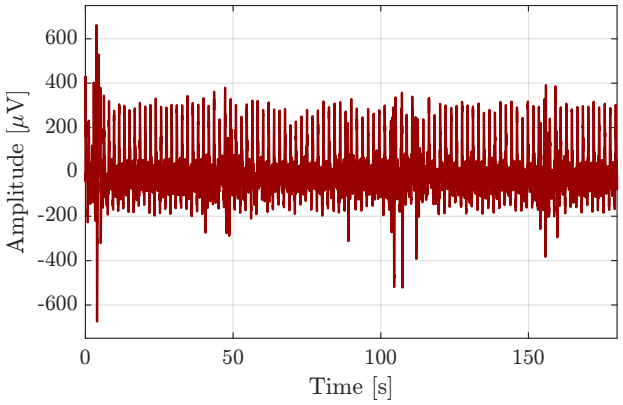

(a) Suspected artifacts from an unconnected channel of the amplifier.

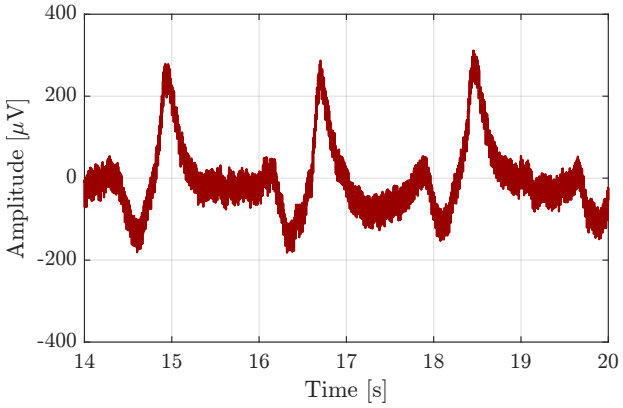

(b) Magnified view of three low-frequency spikes from the unconnected channel.

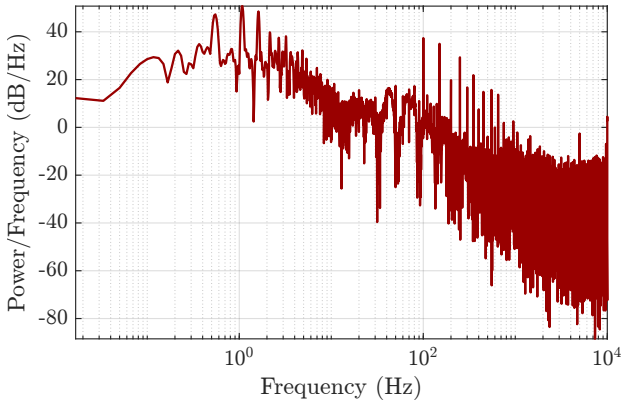

(c) Power spectral density in semilogarithmic scale, to highlight the peaks at low frequency.

Figure 5.14: Artifacts recorded during electrophysiology with the second device.

at lower frequencies.

To search for neural oscillations arising from the local field potential, the PSD was first discretized and sampled every single Hz to reduce the visible noise on the periodogram. The resulting PSD magnified between 0 and 200 Hz is shown in Figure 5.13c, where the dip caused by the applied notch filter around 50 Hz, as well as a peak at 100 Hz (possibly an overtone from 50 Hz) can be observed. By integrating the power over the range of each type of brainwave, the plot in Figure 5.13d hints at a lower activity in the theta rhythm for all the channels but the noisier one (Channel 2 was the only one picking up artifacts from the action potential analysis). This appears plausible, as these waves are usually associated with sleep stages or emotional stress in adult species. On the other hand, the gamma (γ) waves contain the highest power. Another reasonable result is read from the high delta (δ) waves (peaking at 15 dB) being also relatively strong compared to θ- and α-waves. Strong delta brainwaves have been associated with the loss of consciousness induced by anesthetics. In contrast, theta, alpha, and beta waves have been shown to decrease under this cognitive state [88].

5.3.4 Post processing (device 2)

For the second implanted device, a shorter set of data (six traces of three minutes each) was collected. However, the data appeared to be somewhat different from the first device. First and foremost, no tangible action potentials could be observed or extracted along the traces, even when modifying the signal filters. On the other hand, most of the traces, especially from the unconnected channels, picked up very regular artifacts, as shown in Figure 5.14. While the artifacts might appear to be caused by the respiration or the pulse rate, the period of this movement is about 1.8 s, corresponding to a frequency of 33 repetitions per minute, which is considerably lower than the threshold for the breathing rate (70-120 breaths per minute) or for the pulse rate (260-500 beats per minute) in anesthetized rats [89].

The PSD shown in Figure 5.14c, with the frequency axis in logarithmic scale, shows three peaks at 0.53, 1.06, and 1.61 Hz, the last two being overtones of the 0.53 Hz peak. All the sharper peaks at higher frequencies also occur at integer multiples, such as at multiples of 50 Hz, indicating a strong presence of higher overtones. While some of these overtones were noticeable in the spectra of the first tested device, they were weaker and less regular. The artifact overtones observed in Figure 5.14c might be caused by electronic artifacts from the applied notch filter at 50 Hz. Considering that the time-domain peaks are stronger for the unconnected channels, it is likely that the device was not correctly connected to the board, which might have amplified background noise instead.

Chapter 6

Conclusion and future work

In this final chapter, a reflection on the project is given, commenting on the achieved milestones in terms of the modeling outcome, fabrication results, and characterization methods. The possible risks predicted during the writing of the project plan are also commented on. Finally, some indications for possible future work to improve the neural interface are given.

Discussion

The starting point of the project dealt with numerical modeling, whose purpose was to demonstrate a possible set of geometrical parameters that meet the requirement of the device. However, it soon became clear that the interface as a whole could not be simulated with the wave optics package due to the large set of finite elements in the mesh. Consequently, the focus of the numerical modeling shifted towards analyzing the scattering properties as a function of the fundamental parameters (polarization, excited mode, geometrical size) for models reduced in size. The simulations showed that at the largest-possible simulation geometries, scattering mostly depended on the excited mode, but no significative polarization effects were observed.

The initial design plan, combining the laser micromachining tool and physical vapor deposition techniques, was soon replaced by an alternative. The main reason was the limitation in the deposition thickness of metals with physical vapor deposition (less than 500 nm for most available metals), which would require a smaller polymer substrate and possibly lithographical methods to obtain replicable results. However, no compatible substrate complying with the material restrictions at DTU Nanolab was found. Consequently, the integration of electrodes was first investigated with a rectangular PMMA waveguide and tungsten wires partially buried inside the scattered hole. However, not only was it challenging to connectorize the device by aligning the wires on the surface of the device, but this method would have required the encapsulation of the device to insulate the wires and a second round of laser micromachining to expose the electrodes in the desired regions.

Therefore, the subsequent designs tried to integrate the electrodes with the thermal drawing of the preform. Indium and tin were tested with PC to do so. The unsuccessful drawings were mostly attributed to the heat capacity of the metals and the difference between the glass transition temperature of the polymers and the melting point of the metals. This and the asymmetrical preform design (which was inevitable, given the need for a rectangular waveguide and for the electrodes to be

exposed on the same side) led to instability during the thermal drawing. Except for some sparse pieces, the drawn waveguides did not have acceptable quality for continuing with the connectorization step.

An alternative method was found by going back to tungsten microwires. Instead of laying the electrodes on the surface of the waveguide, they were fit inside it by drawing microstructured waveguides with four air channels inside. After adjusting for the partial collapsing of the side holes in the first drawing by tuning the preform design and the pressure during drawing, the second preform successfully provided a long waveguide to produce numerous devices, which were first micromachined and then connectorized. Due to the aforementioned complications, the prototype was completed in the 17^{th} week of the project rather than the 12^{th} week first predicted when writing the project plan.

As regards the optical characterization, the first measurements were done with the PMMA waveguide, from which the observed scattering intensity was relatively weak. Consequently, the subsequent holes were designed to be wider and deeper, enhancing the scattered light further. The optical and electrical characterization on the final PC-W waveguide showed positive results, mainly summarized in the recorded scattering peaks along the surface of the waveguide and the magnitude of the recorded impedance in the frequency bands of interest, respectively. Both the local scattering intensity and the impedance are compatible with an optoelectric interface for optical neural stimulation and electrical recording.

The remaining time in the project allowed for an *in vivo* electrophysiology trial of the interface, described in detail in the previous chapter. The data analysis showed positive preliminary results for the traces collected by one device, from which signs of action potential and local field potential activity were identified. However, an additional chronic study is needed to confirm the capability of the device for space-resolved electrophysiology and to test the potential for optogenetic stimulation.

Overall, the produced flexible polymer interface showed positive results in the characterization phase of the project. The developed models for numerical simulations were not as indicative of the performance of the actual device as expected, primarily due to a combination of the author's inexpertise with advanced modeling and the main focus of the project being the fabrication of the interface. Nevertheless, the obtained results dealing with the spatial distribution of the scattering intensity matched the experimental observation.

The limited timeframe of the project and the temporary interruptions during the project (due to the LMT being temporarily unavailable or to the wait for materials or preform preparation) influenced the final design, whose footprint was not as small as first planned. Nevertheless, having become acquainted with the materials, design, and methods used in the fabrication, scaling down the dimensions of the waveguide while keeping the same structure is believed to be possible. This mainly can be achieved by combining enlarged microstructured channels (thanks to the pressure during thermal drawing and larger machined holes in the preform), a higher capstan speed to reduce the dimensions of the waveguide, and a cutter for thinner tungsten microwires (of 20 µm or 25 µm in diameter). This may be sufficient to scale down the waveguide back to a cross-section of about 250×200 µm or lower. Not only would a smaller and more flexible cross-section decrease the risks of inflammation in a chronic study, but it would also decrease the gap between the exposed electrode and the neurons, which is expected to increase the sensitivity for electrophysiology, especially for

single-unit recordings.

Future work

Combining the findings for the project, as well as some ideas from other works in the literature, some possible topics for future work related to this project are collected in the following list.

- As mentioned above, a new interface might be realized by drawing the waveguide to smaller cross-section features and using thinner tungsten microwires to improve the biocompatibility and the electrical sensitivity for neural recordings. Thinner microwires might also allow for more channels for enhanced space-resolved recording. However, a very high density of channels would be challenging primarily for correct thermal drawing and connectorization. Given the observed minimum hole size in PMMA and PC, the minimum feature size is about 20 µm; hence the size would not be limited by micromachining.

- An alloy of tin with a lower glass transition temperature (such as a bismuth-tin alloy) has been shown to be compatible with thermal drawing for PC [78]. While some issues with the heat conductivity and the asymmetry of the design might still be challenging, it is worth investigating the possibility of iterative thermal drawing with integrated electrodes further, as that might also allow for reduced device cross-section.

- A size reduction might also be obtained via convergence thermal drawing, namely by feeding metal microwires with high melting point (such as tungsten) during the drawing of the fiber, through a previously machined preform [80]. The advantage of this approach is that the machined holes can be much smaller and will adapt to the size of the microwires after drawing. On the other hand, convergence drawing requires a separate feeding system for each microwire and a clamping system that supports them.

- The 3D-printed adapter could be reduced in size by designing the rectangular waveguide aperture on the upper part instead of the lower part to decrease the stress introduced by the bending when implanting the interface.

- The interface should be tested in a chronic study to verify the feasibility of combined optogenetics and electrophysiology. The photosensitive opsins must be expressed with gene therapy viral vectors to restrict the delivery to defined areas and it must be followed by a patient observation period of several days [23].

- To improve the resolution of the illumination region, it is likely that a core/cladding structure in the waveguide (which could be drawn with PMMA and PC, for instance) would decrease the illumination volume, thereby increasing the spatial resolution and easing the distinction between the activated neurons and the rest of the population. Moreover, other hole designs might be investigated to increase the directionality of the scattered light toward the top and decrease the side scattering, as the response of the stimulated neurons cannot be recorded there.

- A more extensive rework might consider polymers compatible with monolithic fabrication. Due to cross-contamination and incompatible techniques, polymeric materials are typically excluded from microfabrication [90]. However, advances in chemically stable and biocompatible polymers have challenged this, presenting polymers, such as plasma-polymerized fluorocarbon (PPFC) and parylenes, which are compatible with microfabrication techniques such as UV lithography, plasma etching, and thin-film deposition [91]. This would allow a dramatic decrease in the size of the implant and better control of the fabrication process compared to the thermal drawing and connectorization methods used in the project.

Bibliography

1. Guertin, P. A. Central pattern generator for locomotion: anatomical, physiological, and pathophysiological considerations. *Frontiers in neurology* **3,** 183 (2013).
2. Welkenhuysen, M. *et al.* An integrated multi-electrode-optrode array for in vitro optogenetics. *Scientific reports* **6,** 20353 (2016).
3. Deisseroth, K. Optogenetics. *Nature methods* **8,** 26–29 (2011).
4. Steinbeck, J. A. *et al.* Optogenetics enables functional analysis of human embryonic stem cell–derived grafts in a Parkinson's disease model. *Nature biotechnology* **33,** 204–209 (2015).
5. Etter, G. *et al.* Optogenetic gamma stimulation rescues memory impairments in an Alzheimer's disease mouse model. *Nature communications* **10,** 5322 (2019).
6. Sawan, M. *Handbook of Biochips: Integrated Circuits and Systems for Biology and Medicine* (Springer, 2015).
7. Zhang, Y. *et al.* Battery-free, lightweight, injectable microsystem for in vivo wireless pharmacology and optogenetics. *Proceedings of the National Academy of Sciences* **116,** 21427–21437 (2019).
8. Zhang, H. *et al.* Emerging Optoelectronic Devices Based on Microscale LEDs and Their Use as Implantable Biomedical Applications. *Micromachines* **13,** 1069 (2022).
9. Kim, K. *et al.* Artifact-free and high-temporal-resolution in vivo opto-electrophysiology with microLED optoelectrodes. *Nature communications* **11,** 1–12 (2020).
10. Jeong, J.-W. *et al.* Wireless optofluidic systems for programmable in vivo pharmacology and optogenetics. *Cell* **162,** 662–674 (2015).
11. Dufour, S. & De Koninck, Y. Optrodes for combined optogenetics and electrophysiology in live animals. *Neurophotonics* **2,** 031205–031205 (2015).
12. Aravanis, A. M. *et al.* An optical neural interface: in vivo control of rodent motor cortex with integrated fiberoptic and optogenetic technology. *Journal of neural engineering* **4,** S143 (2007).
13. Adamantidis, A. R., Zhang, F., Aravanis, A. M., Deisseroth, K. & De Lecea, L. Neural substrates of awakening probed with optogenetic control of hypocretin neurons. *Nature* **450,** 420–424 (2007).
14. Gradinaru, V. *et al.* Targeting and readout strategies for fast optical neural control in vitro and in vivo. *Journal of Neuroscience* **27,** 14231–14238 (2007).

15. Iseri, E. & Kuzum, D. Implantable optoelectronic probes for in vivo optogenetics. *Journal of neural engineering* **14,** 031001 (2017).

16. Wu, F. *et al.* An implantable neural probe with monolithically integrated dielectric waveguide and recording electrodes for optogenetics applications. *Journal of neural engineering* **10,** 056012 (2013).

17. Kim, T.-i. *et al.* Injectable, cellular-scale optoelectronics with applications for wireless optogenetics. *Science* **340,** 211–216 (2013).

18. Kathe, C. *et al.* Wireless closed-loop optogenetics across the entire dorsoventral spinal cord in mice. *Nature biotechnology* **40,** 198–208 (2022).

19. Fu, R. *et al.* Implantable and biodegradable poly (l-lactic acid) fibers for optical neural interfaces. *Advanced Optical Materials* **6,** 1700941 (2018).

20. Spagnolo, B. *et al.* Tapered fibertrodes for optoelectrical neural interfacing in small brain volumes with reduced artefacts. *Nature Materials* **21,** 826–835 (2022).

21. Shan, D. *et al.* Flexible biodegradable citrate-based polymeric step-index optical fiber. *Biomaterials* **143,** 142–148 (2017).

22. Cho, I.-J., Baac, H. W. & Yoon, E. *A 16-site neural probe integrated with a waveguide for optical stimulation* in *2010 IEEE 23rd International Conference on Micro Electro Mechanical Systems (MEMS)* (2010), 995–998.

23. Tian, H., Xu, K., Zou, L. & Fang, Y. Multimodal neural probes for combined optogenetics and electrophysiology. *Iscience* **25,** 103612 (2022).

24. Zou, L. *et al.* Self-assembled multifunctional neural probes for precise integration of optogenetics and electrophysiology. *Nature Communications* **12,** 5871 (2021).

25. Anikeeva, P. *et al.* Optetrode: a multichannel readout for optogenetic control in freely moving mice. *Nature neuroscience* **15,** 163–170 (2012).

26. Montgomery, K. L., Iyer, S. M., Christensen, A. J., Deisseroth, K. & Delp, S. L. Beyond the brain: Optogenetic control in the spinal cord and peripheral nervous system. *Science translational medicine* **8,** 337rv5–337rv5 (2016).

27. Karimi, A., Shojaei, A. & Tehrani, P. Mechanical properties of the human spinal cord under the compressive loading. *Journal of chemical neuroanatomy* **86,** 15–18 (2017).

28. McAlinden, N. *et al.* Multisite microLED optrode array for neural interfacing. *Neurophotonics* **6,** 035010–035010 (2019).

29. Saleh, B. E. & Teich, M. C. *Fundamentals of photonics* (john Wiley & sons, 2019).

30. Nikitin, P. V., Stancil, D. D. & Erosheva, E. A. *Estimating the number of modes in multimode waveguide propagation environment* in *2011 IEEE International Symposium on Antennas and Propagation (APSURSI)* (2011), 1662–1665.

31. Tamaki, K., Takase, H., Eriyama, Y. & Ukachi, T. Recent progress on polymer waveguide materials. *Journal of Photopolymer Science and Technology* **16,** 639–648 (2003).

32. Tao, G. *et al.* Infrared fibers. *Advances in Optics and Photonics* **7,** 379–458 (2015).

33. Borzycki, K., Kobelke, J., Schuster, K. & Wójcik, J. *Arc fusion splicing of photonic crystal fibers to standard single mode fibers* in *Photonic Crystal Fibers IV* **7714** (2010), 273–284.

34. Schift, H. Nanoimprint lithography: An old story in modern times? A review. *Journal of Vacuum Science & Technology B: Microelectronics and Nanometer Structures Processing, Measurement, and Phenomena* **26,** 458–480 (2008).

35. Franke, J. *et al. Optical Polymer Waveguides: From the Design to the Final 3D-Opto Mechatronic Integrated Device* (Springer Nature, 2022).

36. Beckers, M., Schlüter, T., Vad, T., Gries, T. & Bunge, C.-A. An overview on fabrication methods for polymer optical fibers. *Polymer International* **64,** 25–36 (2015).

37. Bunge, C.-A., Beckers, M. & Gries, T. *Polymer Optical Fibres: Fibre Types, Materials, Fabrication, Characterisation and Applications* (Woodhead Publishing, 2016).

38. Argyros, A. Microstructured polymer optical fibers. *Journal of Lightwave Technology* **27,** 1571–1579 (2009).

39. Barton, G., van Eijkelenborg, M. A., Henry, G., Large, M. C. & Zagari, J. Fabrication of microstructured polymer optical fibres. *Optical Fiber Technology* **10,** 325–335 (2004).

40. Zhang, Y. *et al.* Casting preforms for microstructured polymer optical fibre fabrication. *Optics express* **14,** 5541–5547 (2006).

41. Gao, Y. *et al.* Consecutive solvent evaporation and co-rolling techniques for polymer multilayer hollow fiber preform fabrication. *Journal of materials research* **21,** 2246–2254 (2006).

42. Cordeiro, C., Ng, A. K. & Ebendorff-Heidepriem, H. Ultra-simplified single-step fabrication of microstructured optical fiber. *Scientific Reports* **10,** 1–12 (2020).

43. Ahmed, R. Optical study on poly (methyl methacrylate)/poly (vinyl acetate) blends. *International Journal of photoenergy* **2009** (2009).

44. Woyessa, G. *Lecture notes for the course in Novel Optical Fibres in Life Sciences, Lecture 5*

45. Vo-Dinh, T. *Biomedical photonics handbook: biomedical diagnostics* (CRC press, 2014).

46. Pisanello, F. *et al.* Dynamic illumination of spatially restricted or large brain volumes via a single tapered optical fiber. *Nature neuroscience* **20,** 1180–1188 (2017).

47. Snyder, A. W., Love, J. D., *et al. Optical waveguide theory* (Chapman and hall London, 1983).

48. Pisanello, M. *et al.* Tailoring light delivery for optogenetics by modal demultiplexing in tapered optical fibers. *Scientific reports* **8,** 1–11 (2018).

49. Gradinaru, V., Mogri, M., Thompson, K. R., Henderson, J. M. & Deisseroth, K. Optical deconstruction of parkinsonian neural circuitry. *science* **324,** 354–359 (2009).

50. Cardin, J. A. *et al.* Targeted optogenetic stimulation and recording of neurons in vivo using cell-type-specific expression of Channelrhodopsin-2. *Nature protocols* **5,** 247–254 (2010).

51. Nagel, G. *et al.* Channelrhodopsin-1: a light-gated proton channel in green algae. *Science* **296,** 2395–2398 (2002).

52. Nagel, G. *et al.* Channelrhodopsin-2, a directly light-gated cation-selective membrane channel. *Proceedings of the National Academy of Sciences* **100,** 13940–13945 (2003).

53. Kleinlogel, S. *et al.* Ultra light-sensitive and fast neuronal activation with the Ca2+-permeable channelrhodopsin CatCh. *Nature neuroscience* **14,** 513–518 (2011).

54. Bamann, C., Gueta, R., Kleinlogel, S., Nagel, G. & Bamberg, E. Structural guidance of the photocycle of channelrhodopsin-2 by an interhelical hydrogen bond. *Biochemistry* **49,** 267–278 (2010).

55. Lin, J. Y., Lin, M. Z., Steinbach, P. & Tsien, R. Y. Characterization of engineered channelrhodopsin variants with improved properties and kinetics. *Biophysical journal* **96,** 1803–1814 (2009).

56. Mutoh, H., Perron, A., Akemann, W., Iwamoto, Y. & Knöpfel, T. Optogenetic monitoring of membrane potentials. *Experimental physiology* **96,** 13–18 (2011).

57. Zhao, Y. *et al.* An expanded palette of genetically encoded Ca2+ indicators. *Science* **333,** 1888–1891 (2011).

58. Zhang, F. *et al.* Optogenetic interrogation of neural circuits: technology for probing mammalian brain structures. *Nature protocols* **5,** 439–456 (2010).

59. Bretschneider, F. & De Weille, J. R. *Introduction to electrophysiological methods and instrumentation* (Academic Press, 2018).

60. Frank, J. A., Antonini, M.-J. & Anikeeva, P. Next-generation interfaces for studying neural function. *Nature biotechnology* **37,** 1013–1023 (2019).

61. Barnett, M. W. & Larkman, P. M. The action potential. *Practical neurology* **7,** 192–197 (2007).

62. Braini, C. *Biophysical approach of neuronal shapes* PhD thesis (Université Grenoble Alpes, 2016).

63. Im, C. & Seo, J.-M. A review of electrodes for the electrical brain signal recording. *Biomedical Engineering Letters* **6,** 104–112 (2016).

64. Hong, G. & Lieber, C. M. Novel electrode technologies for neural recordings. *Nature Reviews Neuroscience* **20,** 330–345 (2019).

65. Herreras, O. Local field potentials: myths and misunderstandings. *Frontiers in neural circuits* **10,** 101 (2016).

66. Nelson, M. J. & Pouget, P. *Do electrode properties create a problem in interpreting local field potential recordings?* 2010.

67. He, B. *Neural engineering* (Springer, 2005).

68. Guo, L. *et al.* A PDMS-based integrated stretchable microelectrode array (isMEA) for neural and muscular surface interfacing. *IEEE transactions on biomedical circuits and systems* **7,** 1–10 (2012).

69. Adrega, T. & Lacour, S. Stretchable gold conductors embedded in PDMS and patterned by photolithography: fabrication and electromechanical characterization. *Journal of Micromechanics and Microengineering* **20,** 055025 (2010).

70. Dymond, A. M., Kaechele, L. E., Jurist, J. M. & Crandall, P. H. Brain tissue reaction to some chronically implanted metals. *Journal of neurosurgery* **33,** 574–580 (1970).

71. Marg, E. & Adams, J. E. Indwelling multiple micro-electrodes in the brain. *Electroencephalography and clinical neurophysiology* **23,** 277–280 (1967).

72. Canales, A. *et al.* Multifunctional fibers for simultaneous optical, electrical and chemical interrogation of neural circuits in vivo. *Nature biotechnology* **33,** 277–284 (2015).

73. Obaid, A. *et al.* Massively parallel microwire arrays integrated with CMOS chips for neural recording. *Science Advances* **6,** eaay2789 (2020).

74. *The Finite Element Method (FEM)* https://www.comsol.com/multiphysics/finite-element-method (2023).

75. Polyanskiy, M. *RefractiveIndex.INFO* https://refractiveindex.info (2023).

76. Baker, T. J. Mesh generation: Art or science? *Progress in Aerospace Sciences* **41,** 29–63 (2005).

77. Landau, L. EM Lifshitz The classical theory of fields. *Course of theoretical physics* **2** (1975).

78. Jiang, S. *et al.* Spatially expandable fiber-based probes as a multifunctional deep brain interface. *Nature communications* **11,** 6115 (2020).

79. AG, 3.-M. *microSTRUCT vario catalog*

80. Antonini, M.-J. *et al.* Customizing MRI-Compatible Multifunctional Neural Interfaces through Fiber Drawing. *Advanced Functional Materials* **31,** 2104857 (2021).

81. Wang, S. *et al.* Electrochemical impedance spectroscopy. *Nature Reviews Methods Primers* **1,** 41 (2021).

82. Magar, H. S., Hassan, R. Y. & Mulchandani, A. Electrochemical impedance spectroscopy (EIS): Principles, construction, and biosensing applications. *Sensors* **21,** 6578 (2021).

83. Lazanas, A. C. & Prodromidis, M. I. Electrochemical Impedance Spectroscopy - A Tutorial. *ACS Measurement Science Au* (2023).

84. Watson, C., Paxinos, G., Kayalioglu, G. & Heise, C. in *The spinal cord* 238–306 (Elsevier, 2009).

85. Technologies, I. *Intan Technologies Downloads Page* https://intantech.com/downloads.html?tabSelect=Software (2023).

86. Prasad, A. & Sahin, M. Characterization of neural activity recorded from the descending tracts of the rat spinal cord. *Frontiers in neuroscience,* 21 (2010).

87. DiMarco, A. F., Kowalski, K. E., Supinski, G. & Romaniuk, J. R. Mechanism of expiratory muscle activation during lower thoracic spinal cord stimulation. *Journal of Applied Physiology* **92,** 2341–2346 (2002).

88. Bhattacharya, S. *et al.* Propofol anesthesia alters cortical traveling waves. *Journal of Cognitive Neuroscience* **34,** 1274–1286 (2022).

89. For Laboratory Animal Medicine, U. *Guidelines on Anesthesia and Analgesia in Rats* https://az.research.umich.edu/animalcare/guidelines/guidelines-anesthesia-and-analgesia-rats (2023).

90. Chang, B., Liu, X., Bertram, N. & Han, A. Flexible BioMEMS devices enabled by micromachining of plasma-polymerized fluorocarbon. *Micro and Nano Engineering* **19,** 100177 (2023).

91. Yamagiwa, S., Ishida, M. & Kawano, T. *Flexible optrode array: Parylene-film waveguide arrays with microelectrodes for optogenetics* in *2015 Transducers-2015 18th International Conference on Solid-State Sensors, Actuators and Microsystems (TRANSDUCERS)* (2015), 277–280.